

**Identification of Potential Reservoir sands within the Torok Formation
in a northern portion of the National Petroleum Reserve – Alaska**

By:
Javier Herbas
Department of Earth and Planetary Science
McGill University
Montreal, Quebec, Canada

Submitted:
October 02, 2009

A thesis submitted to McGill University in partial fulfillment of the
requirements of the degree of Master of Science

@ J. Herbas 2009

ABSTRACT

This thesis examines the seismic responses of potential hydrocarbon charged sandstone reservoirs within the Torok xxxFormation in a northern portion of the National Petroleum Reserve – Alaska (NPRA). By integrating wireline logs, 3D seismic data, seismic attributes and modeling, I show that the most prospective sandstones are those characterized by a decrease in their p-wave, an increase in their s-wave, a suggested increase in porosity (by the density wireline log), and a decrease in Poisson's ratio which causes AVO anomalies Class II and III.

Similar to other sandstones deposited in turbidite channels in the NPRA, some of these potentially porous Lower Torok sandstones show an increase in their absolute amplitude values with an increasing offset (negative gradient) and a negative or positive intercept. This work suggests that those amplitude anomalous responses could be due to the presence of fluid saturated sandstones, which cause the decrease and corresponding increase in p and s-waves that result in a low Poisson's ratio and in the definition of the Class II and III AVO anomalies.

RESUME

Cette thèse étudie la réponse sismique de réservoirs potentiels chargés d'hydrocarbure, formés de grès appartenant à la formation Torok et situés dans la partie nord de la réserve nationale d'hydrocarbure de l'Alaska (NPRA). En intégrant les diagraphies, les données sismiques 3D, les attributs sismiques et la modélisation, je démontrons que les grès les plus prospectifs sont caractérisés par une diminution de leur amplitude d'onde de compression, une augmentation de leur amplitude d'onde transversale, une augmentation suggérée de la porosité (diagraphie de densité) et une diminution du coefficient de Poisson qui cause des anomalies AVO (variation de l'amplitude avec le déport) de classe II et III.

Comme pour d'autres grès déposés dans des chenaux de turbidite dans la région du NPRA, certains de ces grès potentiellement poreux de la formation Lower Torok démontrent une augmentation de leur valeur absolue d'amplitude avec un déport augmentant (gradient négatif) et une valeur positive ou négative pour un déport de zéro. Ce travail suggère que ces réponses d'amplitudes anormales pourraient être causées par la présence de grès saturés en fluide, ce qui cause une diminution de l'amplitude des ondes de compression et une augmentation correspondante de l'amplitude des ondes transversales, ce qui résulte en un coefficient de Poisson moins élevé et en une définition des anomalies AVO de classe II et III.

THESIS FORMAT

This thesis was done based on a paper format and it consists of three chapters: Chapter I introduces the geological background of the area, data available, methodology applied and objectives of this case study; chapter II, which is the paper itself; and chapter III that refers to the study conclusions. Additionally, this report has 6 appendices that go through all the mathematical and geophysical background to support the methodology and workflows applied. All pages within this thesis were formatted to meet the guidelines from the thesis preparation document prepared by the faculty of Graduate Studies and Research from McGill University.

CONTRIBUTION OF AUTHORS

I hereby declare that all practical and analytical aspects of the research described herein has been performed and carried out by myself, Javier Herbas. Guidance and supervision was given by Wayne Park, Dr. Andrew Willis and Dr. Bruce Hart to ensure a rigorous scientific method was upheld and adhered to throughout the work.

ACKNOWLEDGEMENTS

I will like to give special thanks to my family, Julio Herbas (father), Nelida de Herbas (mother), Andreina Herbas (sister) and Aaron Mendez (brother in law) for all the support and strength they gave me throughout the course of my Master Program, and to my girlfriend Michaela Bjorseth for helping me by being supportive and being very patient while I was writing this thesis. Without all you guys I could not have finished my MSc.

I wish to thank Petro-Canada, who cordially sponsored the thesis project over its duration and contributed with great technical and intellectual discussions via my mentors, namely Wayne Park and Andrew Willis; WesternGeco for providing the 3-D seismic survey and allowing me to publish the result of this study. Special thanks to Jeff Bever (Alaska Team Leader) and Derek Evoy (Alaska Regional Manager) for giving me the opportunity to work in their team while doing my MSc thesis; to Todor Todorov for his assistance with the AVO Modeling, Anne Halladay for all the attribute analysis discussions; to my very good friend Cindy Koo for going over my thesis several times and for the great times in the mountains; to Tim McCullagh for allowing me to use his thesis as a guide, to Charles Boyer and Jonathan Menivier for helping me with the abstract translation from English to French, and to Dr. Bruce Hart for all his guidance, suggestions and thesis corrections.

TABLE OF CONTENTS

Abstract.....	2
Resume.....	3
Thesis format.....	4
Contribution of authors.....	4
Acknowledgements.....	5
List of Figures.....	8
List of Tables.....	19
List of appendices.....	19
 Chapter one – Introduction to study.....	20
Introduction.....	20
NPRA history.....	22
Previous work.....	23
Objectives.....	24
Database and Methods.....	25
 Chapter two – Identification of potential reservoir sands within the Torok Formation in a northern portion of the National Petroleum Reserves – Alaska.....	27
Abstract.....	27
Introduction.....	27
Geological Setting.....	29
Stratigraphic and structure of the Brookian turbidite play.....	30
Source rocks.....	31
Study area, database and methods.....	33
Results.....	35

1. Seismic calibration and mapping.....	35
2. AVO modeling.....	38
3. Seismic attributes.....	41
Discussion.....	45
1. Depositional geomorphology.....	45
2. Amplitude anomalies.....	46
3. Seismic attribute analysis.....	49
Conclusions.....	50
Acknowledgments.....	52
Chapter three – Conclusions of study.....	98
References.....	101
Appendices.....	109

LIST OF FIGURES

Figure 1: Base map displaying major geologic provinces within the NPRA (boundary indicated by cyan line), namely, the Barrow arch, the Colville foreland basin, the foothills fold belt, and the Brooks Range overthrust. These provinces overlap to varying degrees, but can be divided on the basis of geological history affecting known and possible petroleum occurrence (Montgomery, 1998). Some of the known oil and gas accumulations are displayed on the map on green and red, respectively. The seismic survey used is within the northern part of the NPRA. Its exact location cannot be revealed due to confidentiality agreements. Additionally, the map includes the location of the Tarn and Meltwater fields, which are two of the most recent discoveries made on bottom-sets on the North Slope of Alaska, plus the Kuparuk River Field, which is the second largest in North America following Prudeau Bay.....53

Figure 2. Seismic expression of Brookian depositional style in the eastern part of the NPRA showing topset, clinoform, and bottomset strata geometries and relation to the LCU and Beaufortian sequence. Location of this 2D seismic section is displayed with a red line on base map (left). A secondary green transect is displayed on the base map which represents the west-to-east orientation of the seismic section from Figure 4.....54

Figure 3. Chronostratigraphic column for the Colville foreland basin, northern Alaska, showing revised stratigraphic nomenclature and ages of units (Mull et al, 2003).....55

Figure 4 .West-to-east transect built out of 2D lines extracted from the USGS (Unite States Geological Survey) data base. Two strong reflectors were interpreted; the LCU (upper in red), and the Shublik (lower in green), plus the major faults towards the east. Above the LCU lies the HRZ (one of the well known source rocks in the NPRA), which has on top prograding

clinoforms towards the east that represent the basin filling pattern. Location of this transect is displayed on top of a base map on Figure 2 with green..56

Figure 5. Seismic section with a west-to-east orientation with 4 different seismic files: a) full stack time-migrated seismic data processed with a non AVO friendly sequence, b) full stack time-migrated seismic data processed with an AVO friendly sequence, c) near angle stack seismic data generated by stacking shot gathers from 10 to 20 degrees, and d) far angle stack seismic data generated by stacking shot gathers from 30 to 40 degrees. All the sections have well A overlain, which has a GR log (purple) displayed on its left, a sonic log on its right (green), and a synthetic seismogram in the middle (green). Amplitude increases between the near (c) and the far (d) angle stacks are very prominent and easy to visualize, in particular on some of the troughs closer to the left of the section. The full stack time-migrated seismic file (a) was used for horizon picking since the events are more continuous, although for seismic attribute extraction purposes, the AVO friendly was the one used because the compliant processing sequence applied preserves the amplitudes.58

Figure 6. Well A displaying zero-offset synthetic seismograms generated with three different types of wavelets (Butterworth, Ormsby and Ricker). Best result was achieved with the 10, 18, 50, 72 Hz Butterworth with no phase rotation. Two strong markers (HRZ and LCU) used for calibration are displayed at the bottom. GR logs are displayed on the left (purple curves) and DT logs to the right (green curves). High slope channels (shallower) and the basin floor fans (deeper – above the HRZ marker) are displayed on the GR log. Synthetics seismograms have not been stretched nor compressed in order to try and preserve velocities as much as possible. Yellow rectangles show the correlation window used, with the best values achieved at the bottom below the HRZ and LCU markers, whereas above these, the ties were rather poor, possibly due to the event thicknesses (below seismic resolution), lateral lithology variations, and/or the type of

migration (time migration) and algorithm used. See Figure 6 for exploded synthetic and further analysis.....60

Figure 7. Exploded synthetic seismogram for well A generated by reducing the resolution of both, the DT(red in far left) and the RHOB (blue in far left) logs, by forcing them to have a maximum of 100 blocks. From left to right, the exploded synthetic is located in the middle with red and blue colours to differentiate from one trace to the next; the synthetic seismogram, product of adding the individual traces displayed by the exploded synthetic, is in black to its right; and lastly the full stack seismic file is located to the far right. Fifteen Torok Sand markers are activated with a red horizontal line across the entire display for analyses purposes. The exploded synthetic shows on top of each of these Torok Sand markers how the amplitudes cancel or add up resulting in stronger/weaker peaks and/or troughs in the synthetic seismogram, therefore smearing some of the reflections and resulting in a poor synthetic tie as it can be concluded by correlating the synthetic with the Full stack seismic data.....62

Figure 8. Synthetic shot-gathers for Well B generated with a full-elastic wave equation. Seismic markers present at this well location are displayed with small blue letters on the left. The word math on the well logs means that they have been filtered to reduce the noise content. Red and green arrows with respective letters above them, suggest what is interpreted as potential AVO anomalies Class III and II, respectively. As described on the exploded synthetic (Figure 6), the seismic reflections are interfering with each others, causing the different onsets (peaks or troughs) to either partially or totally cancel themselves, or increase their magnitudes, therefore, erroneous AVO signatures are produced within the synthetic shot gathers (far right). This effect is the result of having events thinner than the minimum resolvable distance by the seismic data. Markers A, F, H and I, appear to be Class II AVO anomalies, where a peak or a subtle trough becomes a strong trough in the far offset, whereas markers B, C, D and E

come out as Class III AVO anomalies, defined as a trough increasing its magnitude in the far angles. From the markers with a Class II AVO anomalies response, A shows no P-wave velocity variation, has almost no sand, if any, and has a high Poisson's ratio, consequently it can be interpreted as a false AVO signature. From the markers with a Class III AVO anomaly response, B and D have no sand and have high Poisson's ratio values, therefore these can be consider false AVO signatures as well. The rest of the markers (C, G, F, H and I) are all characterized by a decrease in P-wave velocity, an increase in S-wave velocity, a decrease in density (suggesting an increase in porosity), a decrease in Poisson's ratio (typical response of fluid-filled reservoirs) and a Class II or III AVO signature (shot gathers).....64

Figure 9 Seismic section with Well A displayed on top of the fully stacked time-migrated seismic data (not AVO friendly). The well has displayed a GR log (left), a DT log (right), and a synthetic seismogram (center). These logs together show the seismic character of 17 of the main interpreted markers. The lower portion of the GR (above the HRZ up to Torok E) shows interbedded sands with shales that represent the lower fan system, whereas above this interval, the present sands correspond to high slope channels. As the GR shows, the thickness of some of these sands at this well location are considerably below the seismic resolution, making it impossible to map as individual packages, so they were mapped as groups between the two same most proximal onset types (e.g. from trough to trough). As explained with the exploded synthetic (Figure 6), the well-to-seismic ties above the HRZ are poor due to unresolvable events by the seismic data, time-migration and algorithm applied, AVO anomalies present, and lateral lithology variations due to the deposition environment (turbidites/basin floor fans).....66

Figure 10. Correlation from a time window starting at 0.6942 to 1.1065 ms from a synthetic seismogram generated with a 10, 18, 50, 72 Hz

Butterworth wavelet from Well A. The polarity used was normal and the maximum correlation coefficient achieved was 0.673. The correlation coefficients suggested that a bulk time shift of 208 ms was needed plus a relative phase rotation of 6 degree, which was not corrected due to its numerical size. This synthetic was generated from the southernmost well, where the clinoforms tend to thin down. The low correlation could be due in part to the thickness of the high slope channels and the interbedded sands with shales being below tuning (below seismic resolution), lateral lithology variations caused by the presence of many channels, low signal to noise ratio, and/or the presence of the AVO anomalies above the HRZ marker..68

Figure 11. Time structural maps of markers HRZ, E, I, J, K, and L. Hot colours (towards yellow) indicate shallow values whereas colder (towards blue) are indicating deeper intervals. These time structural maps suggest that the highs are located to the west with a northeastern to southwestern orientation that dips towards the east, which follows the basin filling pattern of the North Slope of Alaska (Figure 13). The HRZ map suggests the presence of a subtle high or anticline (black arrow in map a) that thins as it passes down the slope to the south east, whereas as it gets shallower, markers I, J, and K suggest an additional pattern towards the south, where there is a pronounced low (black arrow on maps c, d and e) that appears to get partially filled up as marker L is reached (map f).....70

Figure 12. Composite of isochrons where the base of each map corresponds to the HRZ, the top or shallower markers are surfaces that get younger in age starting with marker G (a) all the way to marker L (f). Color bars used are the same for the six maps, with red to yellow displaying shallow values, and dark blue representing deeper contours. This set of maps clearly show the west-to-east depositional filling pattern reflected by contours with an approximate south-to-north trend and an east dip that indicates the filling pattern over the slope towards the basin as the seismic transect from Figure 4 also suggests. Isochrons for intervals H, I, J, K, and

L suggest the presence of a low (black arrow in each map), easily recognized with the white trend line between the yellow and light blue colors. This low could potentially be a good location for sediment deposits that were carried by currents down the slope.....72

Figure 13. Composite isochrons for individual intervals with constant color bar, where hot colors (towards red) represent thicker intervals and cold colors (towards dark blue) thin intervals. These isochrons together suggest that the depocenter of the bodies (red-to-yellow) deposited on top of the slope migrated with a north-eastern-to-south-western trend, giving this way an idea of how the sediments got deposited by always looking for the lower part on the relief of the slope that corresponded to the previous lobes. This is the expected behavior as currents always look for the deeper or lower paths to go through and thus deposit part of their sediment loads on their paths. a) interval D-E with two dashed arrows that show the trends of the thickest parts of the isochron where it was assume that the biggest sediment load was deposited; b) interval E-Ea with one dashed arrow that follows the thickest part of this body which appear to be accommodated approximately between the two previous depocenters from D-E; c) interval Ea-F, again with two dashed arrows, one that migrated to the south, whereas the other (northern one) seems to have filled in the thinner part (blue) from interval E-Ea; d) interval F-G showing scattered bodies that are the response of probably thin sands or interbedded sands with shales below the seismic resolution; e) interval J-K with two dashed arrows to the south on top of what could be one or two depocenters; and f) interval K-L with two dashed arrow following two potential depocenters that partially filled what seemed to be thinner intervals from J-K.....79

Figure 14. Wireline logs corresponding to Well A with seismic markers J (green), I (red) and HRZ (blue) displayed. Two cut-off values were applied; a first one of 120 to indicate sandstones (yellow) on the GR, and a second of 10 ohm.m on the resistivity logs (red vertical line) to indicate potential

hydrocarbon presence or fresh water sandstones. Marker J corresponds to the top of a relatively thin sandstone package (low GR reading) which is characterized by a increase in P-wave (DT), a decrease on the S-wave (DT_SH), a decrease in density (RHOB), and an increase in resistivity, normally interpreted as a hydrocarbon indicator, since hydrocarbons, as the rock's matrix, are not-conductive, therefore, as the hydrocarbon saturation of the pores increases, the rock's resistivity also is expected to increase. Marker I represents potentially the base of a thin sandstone, but in this case this pick is characterized by basically no changes on P nor S-waves, a relatively small decrease on density but no increase on resistivity, suggesting no hydrocarbon saturation.....76

Figure 15. Composite image of seismic marker J (horizon J on Figure 8 close to AVO signature marker C); a) West-to-east section from the fully stack time-migrated seismic file is displayed with Well A overlain. Additionally, a GR (left), a synthetic seismogram (middle), and a sonic log (right) are displayed for further interpretation. The GR log defines marker J as the closest seismic marker to the top of a sandstone characterized by a decrease in the P-wave velocity; b) time structural map (upper middle) with hot colours (towards yellow) representing shallower values, and cold colours (towards blue) representing deeper values. Map is showing the orientation of the slope with a set of arrows pointing at lows that could be interpreted as feeders with some high slope channels developing down the slope towards the basin; c) corresponds to the maximum trough amplitude extracted from the fully stacked seismic file (AVO friendly). Color bar shows low amplitudes in black and high amplitudes in red. The high amplitude values define potential high slope channels that appear to form fans/lobes like features down the slope towards the basins (right); d) and e), correspond to the maximum trough amplitudes extracted from the near (NAS) and the far angle stacks (FAS), respectively, both with color bars that define low maximum trough values in black and high maximum trough values in red. Furthermore, the difference between FAS and NAS was

calculated (f). This variation corresponds to the absolute increase in amplitude that was interpreted from the AVO signatures from the synthetic shot gathers (Figure 8), which we will call, for the purpose of the analysis, “sweet spots”. The color bar for this map (f) shows in light brown and dark blue, the lowest amplitude differences, which in this case can be interpreted to be the calculated attribute from bad manual picking or noise that was incorporated inside of the attribute analysis time window, therefore only the highest amplitude (lighter blue), are considered as potential sweet spots.....78

Figure 16. Composite image of seismic marker J (horizon J close to AVO signature marker C) showing two complex trace attribute analyses (see Appendix A for complex trace attribute analysis theory), average reflection strength (a, b and c maps), also known as envelope amplitude, and the total energy (d, e, and f maps). Both attributes were extracted from the NAS and FAS, and additionally, the difference between the FAS and the NAS was calculated (c and f) as for the maximum trough amplitude on Figure 14. The color bars for the NAS and FAS define low amplitudes as colours towards black and high amplitude as colours towards red. The NAS maps (a and d) roughly define what can be interpreted as a high slope channel system, with most of these channel like features suggesting a steep slope due to their almost straight trend. The FAS (b and e) sharpen the amplitudes that define some of these events. This was an expected response from the modeling results (Figure 8), maximum trough amplitude analysis (Figure 15), and also an anticipated response from the Alaskan sandstones with Class II to III AVO anomalies. Maps c) and f) show the calculated difference between the FAS and the NAS (potential sweet spots), and as indicated by the color bars, the light brown colours correspond to the lowest amplitude differences, which as for the maximum trough amplitude case, are considered the results of bad manual picking or noise that comes in from the time window used to extract these attributes,

therefore only the highest differences (blue features following the high slope channel features trend) are considered sweet spots.....80

Figure 17. Composite of post-stack trace attributes with seismic files displayed on top of seismic marker J on a 3D visualization software. All trace attribute were calculated from the full stack time-migrated seismic file (AVO friendly) (Appendix A). a) Time structural map with red colours indicating shallower depths and blue colours deeper values; b) full stack time-migrated seismic file with troughs in yellow and peaks in darker blues. The highest negative amplitude values correspond to the same locations as the features interpreted as high slope channels from Figures 15 and 16; c) semblance cube with black colours corresponding to 0 correlation (indicating discontinuities) and brighter blue colours corresponding to total correlation (correlation equal to 1). Three distinctive trends can be identified; a first to the north-east, a second to the south of the first, and a third located to the south with a west-to-east trend. The two southernmost correspond to the same locations as two of the probable fan/lobes deposited by the feeder channel coming down the slope, whereas the northernmost was capture by the horizon based attributes from Figures 15 and 16 but it is not sharp enough to make a conclusion on what it could be; d) sweetness ($I_{amp}/(I_{freq})^{1/2}$), as the semblance results, this attribute shows the same three distinctive features (red and yellow colours), but with better boundaries delineated, most probably due to the scale of the attribute itself, which is not constrain from 0 to 1 as semblance is; e) gradient (generated from shot gathers), used in many cases as a lithology differentiator. In this case, two distinctive trends are differentiated, a first yellow-to-orange that follow the trends of the high slope channels and are suggested to be at least partially filled with sands by the GR log from Figure 14, and a second in blue that represents what was interpreted to be unconfined fans/lobes that could be filled in by either shales or interbedded sands with shales; and f) instantaneous phase, an attribute known to emphasize spatial continuity, shows in grey the continuity of the troughs

(compare to map b), whereas in red parts of the peaks and not-continuous events.....82

Figure 18. Composite image of a thin sandstone interval enclosed between seismic markers I and J. a) West-to-east seismic section of the full stack seismic file with Well A displayed. Three logs describe the interval starting from left to right with a GR (purple), a zero-offset synthetic seismogram and a DT (green). a) Isochron of interval I-J with blue colors showing the thickest parts, whereas grays described the thinnest parts of the interval. The isochron suggests that the sediment at that corresponding geological time was deposited preferentially in lows.....84

Figure 19. Composite image of marker I. a) Seismic section corresponding to a west-to-east line from the time-migrated seismic file with Well A displayed on top. Additionally, a GR (left), a synthetic seismogram (middle), and a sonic log (right) are displayed. The seismic character of this horizon is a strong trough that appears very close to the base of a thin sandstone (GR log). b) Time structural map showing multiple possible feeders (arrows) with high slope channels developing down the slope toward the beginning of the basin. c) Average reflection strength or amplitude envelope calculated from the full stack time-migrated seismic file. The lower three maps correspond to maximum trough amplitudes extracted from the near (d) and the far (e) angle stacks, plus the difference between them that defines potential sweet spots (f). The synthetic shot gathers generated by modeling (Figure 14) indicate that this marker is characterized by an amplitude response with increasing offset that corresponds to a false AVO signature.....86

Figure 20. Composite of two similar amplitude statistic seismic attribute maps, RMS amplitude and total energy. The upper maps correspond to RMS calculated from near (a) and far (b) angle stacks, plus the difference between them (c), whereas the lower correspond to total energy calculated from the same angle stacks. The far minus the near angle stacks (offset)

define the difference in amplitude with increasing offset, which according to the synthetic shot gathers correspond to amplitude responses that correspond to seismic background. Color bars for the total energy (d, e, and f) outputs were adjusted in order to sharpen the false AVO signatures described in the far angles.....88

Figure 21. Summary of RMS amplitudes of randomly selected markers within the Torok Formation calculated from far angle stacks (FAS) to isolate the amplitude responses with increasing offset. By isolating these responses from the FAS, amplitude responses with increasing offset that define possible deep water geomorphologies can be better analyzed due to their increased sharpness. Some of these responses are what characterize AVO anomalies Class II and III, although before classifying them it is necessary to analyze the synthetic shot gathers acquired from the AVO modeling (Figure 8).....90

Figure 22. Summary of the differences between maximum trough amplitude calculated from the far and near angle stack seismic files from randomly selected markers within the Torok Formation. Normally, when in the presence of Class II or III AVO anomalies, the difference between attributes calculated from far and near angle stacks will define the sweet spots or bodies with anomalous amplitude, but as it can be seen from either Figure 14 or Table 2, there is always the possibility of obtaining an AVO response from the seismic background, which can be due to factors such as a shale with a decrease in P-wave and an increase in S-wave velocity, small porosity variations, wrong seismic processing sequence applied, and the presence of volcanic ash, among others.....92

Figure 23. Schematic block diagram illustrating submarine fan deposition based on the slope channel system defined by integrating the time structural maps with the seismic attributes extracted mainly from the far angle stacks. The slope dip angle was interpreted to range between 3 to 5 degrees, based on the path defined by the feeder channels that cut through

the slope and later form potential submarine fans, although, due to the surveys boundaries, the fan development cannot be validated. The composition (lithology) of the high slope channel system and submarine fans is unknown due to a lack of wells penetrating them.....94

LIST OF TABLES

Table 1. Well data base showing the wireline log availability for each well used for both the seismic calibration (DT, GR, and RHOB) and the AVO modeling (DT, DT_SH, GR, and RHOB).....95

Table 2. Classification of the different amplitude responses to increasing offset based on the elastic modeling results obtained for the three different wells with S-wave sonics. The classification is done for individual markers and intervals in cases where sandstone bodies or interbedded sandstones with shales are present between two horizons. Amplitude responses are described based on the intercept (starting onset type) and gradient (slope). In some cases the AVO anomalies observed on both the synthetic shot gathers and the angle stack files correspond to false anomalies, which could be due to reflector dip and depth, receiver array attenuation, inelastic attenuation, thin bed effects, anisotropy and/or an erroneous seismic processing sequence.....96

LIST OF APPENDICES

Appendix A: Theoretical background.....109

Appendix B: Derivation of trace envelope.....127

Appendix C: Hilbert Transform.....129

Appendix D: Zoeppritz equations.....131

Appendix E: Velocity and Elastic Moduli.....134

Appendix F: Map database.....136

CHAPTER 1: INTRODUCTION TO STUDY

INTRODUCTION

In recent years, hydrocarbon exploration in the North Slope of Alaska has been increasing its focus on stratigraphic objectives, particularly in bottomset and clinoform plays of the Lower Cretaceous Torok Formation. Many shows and tests from these Brookian plays (Houseknecht and Schenk, 2001) have been reported, although it has been only 15 years since they became exploration targets thanks to the geological and technological advances that reduced the sizes of the economically viable hydrocarbon accumulations (Montgomery, 1998).

Exploration success in the Brookian plays in the National Petroleum Reserve – Alaska (NPRA), including the discoveries made on the Tarn and Meltwater fields to the east of this area (Figure 1) have stimulated interest in their hydrocarbon potential. Despite all these positive indications, however, a large number of wells have penetrated them without any success, suggesting that a better understanding of reservoir quality, distribution and hydrocarbon charge is needed (Houseknecht and Schenk, 2001).

The Cretaceous and Tertiary Brookian sequence, as summarized by Bird and Molenaar (1992), is a succession of marine and nonmarine deposits shed northward from the Brook Range orogenic belt. The sequence includes thick (>8 km) Colville foreland-basin deposits developed ahead of northward-advancing thrust sheets, relatively thin (<1-4 km) deposits over the subsiding Barrow arch rift shoulder, and thick (>8 km) Canada Basin passive-margin deposits. Brookian deposits are deformed on the south and east by compressional folding and faulting, on the west by wrench faulting, and along the passive margin on the north by growth faulting. The hallmark seismic signature of the Brookian sequence is that of topset-clinoform-bottomset geometry (Figure 2).

The Torok Formation, of Aptian-Cenomanian age (Figure 3), represents a total petroleum system that consists primarily of shale, mudstone, and clay shale with interbedded siltstone and fine-to-medium-grained sandstones that were deposited in slope and basin-floor setting as parts of submarine fans (Morrow, 1985). These fans commonly have multiple lobes that are not easily resolvable with three-dimensional seismic data, but when parts of them are charged with hydrocarbon they sometimes show anomalous amplitude responses with increasing offset. These anomalies can be described by a decrease in Poisson's ratio due to both, a decrease in P-wave (V_p) and an increase in S-wave velocity (V_s), and a positive or negative intercept and gradient illustrated on the amplitude-versus-offset binary graph (Appendix A) that suggests that they represent a Class II (positive intercept) to III (negative intercept) AVO anomaly typical of the Alaska sandstones.

This thesis integrates well logs, 3D seismic data, complex trace-attribute analysis and amplitude variation with offset (AVO) modeling to examine potential reservoir sands within the Torok Formation of the Brookian sequence in a northern portion of the Colville Foreland Basin (Figure 1). The results illustrate the importance of predicting reservoir characteristics in defining potential "sweet spots" (favorable location to drill a well based on an amplitude anomaly).

The Colville Foreland Basin developed at the beginning of the Late Jurassic as a result of tectonic and sedimentary loadings that were associated with the northward advance of the Brooks Range fold and thrust belt. The basin was floored by up to several thousand meters of preorogenic Mississippian-Jurassic strata deposited when the basin area was part of a southward facing passive margin (Montgomery, 1998).

The formation of the Colville foreland basin started with the uplift and unroofing of major portions of the Brooks Range thrust complex. Its major episode of basin filling took place in the Albian-Maastrichtian with prodelta

shales and turbidites that now represent the Torok Formation, and some major pulses of deltaic sedimentation that correspond to the Nanushuk and Colville Groups (Figure 3). These deposits eventually prograded northward and eastward across the Barrow Arch where they established both the continental shelf and the slope clastic environments in the Canada basin. Much of the Cretaceous basin fill subsequently became involved in late-stage thin skinned deformation associated with the foothills terrain (Montgomery, 1998).

NPRA HISTORY

Formerly known as the Naval Petroleum Reserve No. 4, the vast 93,240 km² area of Alaska has a history of nearly 100 years of petroleum exploration and represents today the largest remaining frontier area for hydrocarbon exploration in North America. This area includes major portions of Northern Alaska west and southwest of the Prudhoe Bay-Kuparuk River producing complex, extending from the northern margins of the Brooks Range to the northern coastline (Figure 1) (Montgomery et al. 1998).

In 1923 President Harding set aside this region as an emergency oil supply for the U.S. Navy. In 1976, in accordance with the Naval Petroleum Reserve Production Act, the administration of the reserve was transferred to the Department of the Interior, more specifically the Bureau of Land Management, and was renamed to what is now known as the National Petroleum Reserve-Alaska (NPRA).

The NPRA is composed of 4 major structural-stratigraphic provinces: Barrow Arch, Colville foreland basin, foothills belt, and northern Brooks Range overthrust (Figure 1) (Montgomery et al., 1998). Stratigraphically it is divided into three sequences: Ellesmerian (Mississippian – Early Jurassic),

Beaufortian (Middle Jurassic – Early Cretaceous), and Brookian (early Cretaceous to Tertiary) (Figure 3).

PREVIOUS WORK

The Torok Formation is a thick (18,500 to 3,100 ft) shale unit of Lower Cretaceous (Aptian to Cenomanian) located in the Colville Foreland Basin of the North Slope of Alaska (Mull et al., 2003). This unit was first named by Gryc and others (1951), although the same rocks had previously been referred to as the Topogoruk Fm. Gryc (1951) did core analysis and originally defined the Torok Fm. as a dominantly shale facies. Patton (1956) revised the Torok Fm. for a thick sequence of dominantly nonresistant, fine-grained sedimentary rock. Molenaar (1981, 1985, and 1988) used core descriptions, outcrop sections and 2D seismic data from a USGS public domain database to demonstrate that the Torok Fm. displays the overall seismic geometry of bottomset-clinoforms-topset strata, which suggests an eastward to northeastward migration of a depositional system that included deep marine through non-marine depositional environments. Weimer (1987) performed a seismic stratigraphic analysis of three areas of lower slope failure within the Torok Fm. where he identified and described in detail different facies that changed gradually from organized slides at the upslope edge to disorganized slides and sediment gravity flows basinward. McMillen (1991) did core analysis suggesting, based on sedimentary structures, that the sandstones of the Torok Fm. were deposited as turbidites. Knowles et al. (1997) used the Torok Fm. as part of a group of formations in describing the petroleum potential of the east NPRA. Montgomery (1998) defined the Torok Fm. as prodelta shales and turbidites, based on 2D seismic lines, well log correlations and outcrop mapping that were deposited during the main episode of basin filling, which took place in the Albian-Masstrichtian. Houseknecht and Schenk (1999) identified four distinct phases of shelf margin sedimentation (regression,

transgression, aggradation and progradation) within bottomset and clinoform strata of the Torok Fm. Decker (2007) used lithologic descriptions from mud logs and outcrop measured sections to carry out an interpretative analysis of the west-central North Slope where he named the Nanushuk-Torok as one of the three major genetic cycles recognized in the Brookian sequence in the northern part of the Colville Basin.

Recently, numerous studies of the Torok Fm. within the NPRA have been done in which complex trace attributes and different AVO techniques were combined, but due to the current commercial sensitivity of the area these have been kept confidential.

OBJECTIVES

Previous work on the Torok Formation within the NPRA has focused mainly on defining stratigraphy and seismic facies. This thesis tries to identify the seismic response of potentially hydrocarbon charged sandstone reservoirs within the Torok Formation in the near and far offsets by combining complex trace seismic attributes with AVO modeling. The benefits of doing this research will be a better understanding of the AVO anomalies present in a portion of the 3D survey used located in the north of the NPRA (Figure 1). The following analyses were carried out:

- a. Calibration of seismic and well data
- b. Mapping of relevant seismic markers, including time-structure and Isochron map generation
- c. AVO modeling and generation of near, mid and far angle stacks plus gradient cubes
- d. Complex trace attribute analyses from near and far angle stacks
- e. Reservoir property prediction between wells by integrating AVO modeling, seismic attributes, and wireline logs

DATABASE AND METHODS

The database consists of a southern portion of the 3D survey that covers an area of approximately 914 km² and was acquired by WesternGeco in 2003. Two different seismic files were used; an initial full stack time migrated volume with a 2 ms sampling rate and an approximate dominant frequency of 38 Hz between 500 and 1700 ms, and a secondary AVO friendly (processed with the objective of performing an AVO analysis on it) seismic volume with a sampling rate of 2 ms and a dominant frequency of approximately 30 Hz within the same time interval. Shot gathers from this survey were also available.

A well database with 7 wells was used (Table 1). Unfortunately the names and locations of these wells cannot be disclosed due to confidentiality agreements. The wireline logs available for each well usually included bulk density (DRHOB and/or RHOB), gamma ray (GR), resistivity (ILM, ILD, ATM90, and others), P-wave sonic (DT), S-wave sonic (DT_SH), Poisson's ratio (calculated from P-wave and S-wave velocity) and spontaneous potential (SP).

Zero-offset synthetic seismograms were generated in order to calibrate the wells to the seismic data. AVO modeling was performed on 4 wells with the objective of defining lithologies and the type of amplitude responses to increasing offset. Afterwards, near, mid and far angle stacks and gradient seismic files were created from the original shot gathers. See Appendix A for further explanation of the AVO theory that supports this analysis.

A total of 24 horizons were mapped, 17 troughs and 4 peaks on the time-migrated seismic file and 3 troughs from the far angle stack file. All the horizons were interpolated and used to acquire complex trace attributes from the full stack seismic file, the near and the far angle stacks in order to better understand the nature of the amplitude anomalies present in the

Torok Formation from the Brookian sequence within the NPRA. See Appendix A for theory and explanations on seismic attributes analysis.

CHAPTER 2: Identification of Potential Reservoir Sands within the Torok Formation in a northern portion of the National Petroleum Reserve – Alaska.

ABSTRACT

In this paper we examine potential reservoir sands within foreset and bottomset deposits from the Lower Torok Formation in a northern portion of the National Petroleum Reserve – Alaska (NPRA). By integrating wireline logs, 3D seismic data, seismic attributes and AVO modeling, we show that the most prospective sandstones correspond to “stratigraphic sweet spots” which are characterized by a decrease in their P-wave velocity, an increase in their S-wave velocity, a suggested increase in porosity (by the density wireline log), an increase in resistivity, and a decrease in Poisson’s ratio.

Similar to other sandstones deposited in turbidite channels in the NPRA, some of these potentially porous Lower Torok sandstones show an increase in their absolute amplitude values with an increasing offset (negative gradient) and a negative or positive intercept. This work suggests that those amplitude responses (amplitude anomalies) could be due to the presence of fluid saturated sandstones, which causes the decrease and corresponding increase in P and S-waves sonic logs that result in a low Poisson’s ratio, therefore, in the definition of the Class II and III AVO anomalies.

INTRODUCTION

Covering 93240 km² the National Petroleum Reserve – Alaska (NPRA) represents the largest remaining frontier area for hydrocarbon exploration in North America. This enormous onshore domain has been the setting for close to 60 exploratory wells, of which 19 were drilled by the U.S. Navy

between 1951 and 1975, with an additional 16 wells drilled by the U.S. Geological Survey between 1978 and 1981 (Montgomery, 1998).

In recent years, hydrocarbon exploration in the North Slope of Alaska has been increasing its focus on stratigraphic objectives, particularly in bottomset and clinoform plays of the Lower Cretaceous Torok Formation. Many shows and tests from these Brookian plays have been reported, although it has been only 15 years since they became exploration targets thanks to the geological and technological advances that reduced the sizes of the economically viable hydrocarbon accumulations (Montgomery, 1998).

The Cretaceous and Tertiary Brookian sequence, as summarized by Bird and Molenaar (1992), is a succession of marine and nonmarine deposits shed northward from the Brook Range orogenic belt. The sequence includes thick (>8 km) Colville foreland-basin deposits developed ahead of northward-advancing thrust sheets, relatively thin (<1-4 km) deposits over the subsiding Barrow arch rift shoulder, and thick (>8 km) Canada Basin passive-margin deposits. Brookian deposits are deformed on the south and east by compressional folding and faulting, on the west by wrench faulting, and along the passive margin on the north by growth faulting. The hallmark seismic signature of the Brookian sequence is that of topset-clinoform-bottomset geometry (Figure 2) (Bird, 2001).

The Torok Formation, mostly of Albian age, includes bottomset and clinoform strata that consist of marine and turbidite facies. This formation thickens markedly into the foredeep of the Colville foreland basin, where much of it forms a foredeep clinoform wedge whose geometry indicates eastward migration of a sand rich slope, with the most favorable stratigraphic traps occurring where amalgamated sandstones deposited in turbidite channels incised on the mid to lower slope and on proximal part of submarine fans (Houseknecht et al., 2001).

Exploration success in the Brookian plays in the NPRA, including the discoveries made on the Tarn and Meltwater fields to the east of this area (Figure 1) have stimulated interest in their hydrocarbon potential. Despite all these positive indications, however, a large number of wells have penetrated them without any success, suggesting that a better understanding of reservoir quality, distribution and hydrocarbon charge is needed (Houseknecht and Schenk, 2001).

This research project integrates well logs, 3D seismic data, complex trace attribute analysis and AVO modeling to examine potential reservoir sands within the Torok Formation of the Brookian sequence in a northern portion of the Colville Foreland Basin. The results illustrate the importance of predicting reservoir characteristics in defining potential sweet spots.

GEOLOGICAL SETTING

Based on its hydrocarbon potential, the NPRA can be divided into four geological provinces, which include, from north to south, the Barrow arch, the Colville foreland basin, the Foothills fold belt, and the Brooks Range overthrust (Figure 1). These provinces overlap to varying degrees, but can be divided based on their geologic history affecting known and possible petroleum occurrences (Montgomery, 1998).

The area of study is located in the Colville foreland basin, so only the evolution of this geological province will be explained with detail. This foreland basin started developing in the Late Jurassic as a consequence of the crustal and sedimentary loadings that were associated with the northward advancing movement of the Brooks Range fold and thrust belt. This basin was flooded by thousands feet of preorogenic Mississippian-Jurassic strata that was deposited when the basin area formed part of a south-facing passive margin (Montgomery, 1998; Weimer, 1987).

The formation of this foreland basin started with the uplift and unroofing of major portions of the Brooks Range thrust complex, with a main episode of basin filling that took place during the Albian – Maastrichtian. This episode was characterized by prodelta shales and turbidites from the Torok Formation that happened at the same time as some major pulses of deltaic sedimentation that today represent the Nanushuk and the Colville Group. Finally, all these deposits prograded northward and eastward, where they established the continental shelf and the slope clastic environment of the Canadian Basin (Weimer, 1987).

Results of the hydrocarbon potential evaluation suggest that this province has good to excellent reservoirs within turbidites and deltaic sandstones (Kirschner and Rycerski, 1988). Good quality source beds are found in underlying Triassic-Jurassic deep-marine shales and the Lower Cretaceous Pebble Shale. Entrapment in this portion of the North Slope would be mainly stratigraphic (Montgomery et al. 1998).

STRATIGRAPHY AND STRUCTURE OF THE BROOKIAN TURBIDITE PLAY

The Brookian sequence of northern Alaska includes Early Cretaceous through Tertiary sediments derived from the ancestral Brooks Range and deposited in the Colville foreland basin (Figure 3). The filling of this basin generally progressed from west to east through time as reflected by the eastward strata across the North Slope of Alaska (Figure 4).

The oldest Brookian strata within the NPRA are limited to the highly deformed outcrop belt of the southern Foothills (e.g., Moore and others, 1994), although lower parts of the Torok Formation are likely equivalent to the Fortress Mountain Formation (e.g., Molenaar, 1988). The youngest Brookian strata consist of the uppermost part of the Nanushuk Formation and the lower parts of the overlying Seabee Formation (Houseknecht and

Schenk, 2001). This project was focused exclusively on the Torok Formation of Aptian-Albian age.

The west-to-east regional geometry of the Brookian strata in the NPRA is displayed on Figure 4. Evidence suggests that there is very modest deformation beneath the coastal plain, although the thermal maturity patterns indicate that this area was subject to extensive regional uplift and erosion throughout the Tertiary (O'Sullivan et al. 1997).

Today, around fifteen oil and gas accumulations have been discovered in this sequence in structural and/or stratigraphic traps with the help of 3-D seismic data, seismic attributes and AVO studies. Many believe that this sequence has a very promising potential for future discoveries, and that the most favorable stratigraphic trapping geometries occur where amalgamated sandstones deposited in turbidite channels incised on the mid to lower slope and on the proximal parts of submarine fans during regression are capped by relatively condensed mudstone facies deposited during transgression (Houseknecht and Schenk, 2001).

SOURCE ROCKS

Approximately 15 oil and six gas accumulations have been discovered in the Brookian sequence in structural and stratigraphic traps. Demonstrated source rocks feeding the reservoirs from this sequence include Cretaceous (High Radioactive Zone also known as the HRZ and the pebble shale), Jurassic (Kingak), Triassic (Shublik), and Carboniferous (Lisburne) (Figure 3). Four petroleum systems have been currently identified and described in the North Slope including the Ellesmerian, the Hue-Thompson, the Torok-Nanushuk, and the Canning-Sagavanirtoq (Magoon and Dow, 1994).

The Ellesmerian petroleum system contains a mixture of oil types. Its oil is derived mostly from the Shublik Formation, with varying admixtures from

the Hue Shale (HRZ) and the Kingak Shale (Seifert et al., 1980; Wicks et al., 1991; Masterson et al., 1997; Masterson et al., 2000). Oils in this hybrid system are found along the Barrow arch in reservoir rocks that range in age from Mississippian to Tertiary. Mixing of oils is apparently the result of common migration pathways along rift-related normal faults and along the Lower Cretaceous unconformity (LCU). Some mixing also may have occurred during spilling and remigration of early-accumulated oil in Prudhoe Bay field as a result of regional eastward tilting (Jones and Speers, 1976; Erickson and Sneider, 1997; Masterson et al., 2000).

For the Hue-Thompson system, a definitive match between oils and the Hue Shale (HRZ) source rock has been established (Montgomery, 1998). The Torok-Nanusuk system is postulated to have source rocks in the Brookian and/or Beaufortian sequences, and the Canning-Sagavanirktok system is postulated to have a Brookian source similar to that proposed for some oils in the nearby Mackenzie Delta region of Canada. Oils in these three systems have similar characteristics and are distinguished mainly on the basis of carbon isotopes and biomarkers. Common characteristics of these oils include low sulfurs (less than 1%), 30-40° API, moderate gas-oil ratio (42.5-198 m³/bbl), moderate to high saturate-aromatic hydrocarbon ratio (1.7-3.5), and very low nickel and vanadium content or nickel content greater than vanadium (Magoon, 1994; Lillis et al., 1999; Magoon et al., 1999).

Analyses made by Molennar (1982) and Bird (1994) indicated that the Ellesmerian petroleum system is responsible for over 3 quarters of the total hydrocarbon generated in the region. On the basis of average total organic content (TOC) data and interpreted hydrogen indices, this total is estimated to be in the order of 8 trillion bbl of oil (Bird and Molenaar, 1992). In addition, burial history and TOC information also indicated that the Torok-Nanushuk system generated significant amounts of hydrocarbons within the

margins of the NPRA, mainly in slope and basinal marine shales of the Torok Formation (Montgomery, 1998).

STUDY AREA, DATABASE AND METHODS

The study area corresponds to the southern portion of the 3D survey that covers approximately 914 km² (entire 3D cover over 1600 km²). This survey is located in the central northern part of the National Petroleum Reserve – Alaska, along the Colville Foreland Basin (Figure 1).

The database consists of a fully stacked time migrated seismic volume with a 2 ms sampling rate, an approximate dominant frequency of 38 Hz between 500 and 1700 ms, and a 25 m distance between lines and traces. Additionally, a secondary AVO friendly seismic volume (processed for AVO analysis) with a sampling rate of 2 ms and a dominant frequency of approximately 30 Hz within the same time window was available (Figure 5). Shot gathers from this survey were also on hand.

A well database with 7 wells was used (Table 1). The wireline logs available for each well typically included bulk density (DRHO and/or RHOB), gamma ray (GR), resistivity (ILM, ILD, ATM90, and others), P-wave sonic (DT), S-wave sonic (DT_SH), Poisson's ratio (calculated from P-wave and S-wave sonic logs), and spontaneous potential (SP). Unfortunately, due to confidentiality agreements, it is not possible to reveal the exact location or the names of these wells, therefore for further analysis the wells will be named with letters A to G.

Zero off-set synthetic seismograms were generated to calibrate the wells to the seismic data. Three different types of wavelets were tested; Ricker, Ormsby and Butterworth (Figure 6), with the best result achieved with a 10, 18, 50, 72 Hz Butterworth with zero degree phase rotation. As previously mentioned, there were only 7 wells with the necessary wireline logs to

generate synthetic seismograms; nevertheless a good calibration was achieved that ensured that the appropriate horizons were mapped on the 3D survey. Additionally, exploded synthetic seismograms were generated for 5 wells in order to analyze the reflections within the full stack time-migrated seismic file and to try to better understand the poor tie (low correlation) above the HRZ and LCU markers (Figure 6 and 7). The inputs for these types of synthetics were obtained by blocking the density and P-wave sonic logs.

Prestack synthetic shot gathers were generated by using AVO modeling techniques with a full elastic wave equation for 3 wells (see Appendix A for AVO theory and Figure 8 for modeling results). The inputs for this were S-wave, P-wave and density logs, with a secondary calibration done with the help of gamma ray and resistivity logs. Furthermore, near, mid, and far angle stack seismic files were created from the original shot gathers with the goals of studying amplitude responses to increasing offset as suggested by the AVO modeling results (Figure 8).

Two wedge models were created for 2 of the wells in order to have a good estimate of the minimum resolvable event with the seismic volumes available.

Twenty-four horizons were mapped with a 4x4 grid (100 meters between picks), out of which, 17 were troughs and 4 were peaks from the full stack time-migrated seismic file plus an additional 3 troughs from the far angle stack file (Figure 5). Most of the horizon picking was done on the original full stack seismic file (not AVO friendly – Figure 9) because of the noise content (lower – see Figure 5) that increased the events continuity and made the mapping process easier. All these horizons were validated by a reconnaissance viewing process on the AVO friendly seismic file. The remaining three horizons picked were from the far angle stacks, which had the purpose of delineating some of the amplitude anomalies. The entire set of horizons were interpolated and used to acquired amplitude and complex

trace attributes from the full stack seismic file with the preserved amplitudes (AVO friendly), the near and the far angle stacks (see Appendix A for seismic attribute analysis theory). These attributes were generated between horizons with the same onset type, keeping a maximum of one cycle between them, and within time windows of +/- 4 to 7 milliseconds. Some of these attribute results were also multiplied and/or divided by their corresponding isochrons in order to correlate amplitude anomalies with thicker intervals. Additionally, to better define the extension of the amplitude anomalies, considered sweet spots for the purpose of this study, the difference between seismic attributes extracted from the far and the near angle stack seismic files was calculated.

Coherency (Chopra and Marfurt, 2007) and sweetness (Hart, 2008) were also generated for both the seismic volume and the horizons (see Appendix A for theory on coherency and sweetness). Finally these two were co-rendered in order to get a better visualization of stratigraphical features present in this Low Stand Systems Track (LST) parasequence set.

RESULTS

1. SEISMIC CALIBRATION AND MAPPING

Seven zero-offset synthetic seismograms were generated using a 10, 18, 50, 72 Hz Butterworth wavelet with a 250 ms length and a zero degree phase rotation. Two of these synthetics suggested a 4 to 6 minor phase shift (Figure 10) of the full stack seismic file (pst8.bri), but because only two wells showed it, it was decided to preserve the phase of the original data.

The synthetics show that the well-to-seismic ties were considerably good below the HRZ and LCU (> 80% correlation), which are two strong regional markers normally used for seismic calibration (Figure 6). The HRZ is a condensed section that marks the peak of a transgression (maximum flooding surface), in theory considered an approximate isochronous surface across most of the North Slope Basin in Alaska, whereas the LCU, is the

regional Lower Cretaceous Unconformity. Above these two markers the ties are rather poor (Figure 6 and 9), where a maximum of 67.3% correlation was achieved (Figure 10), with an average lower than 65%. Stretching and compressing the synthetic seismograms was avoided in order to try to preserve the velocities as much as possible. Five exploded synthetics were generated (Figure 7) to try to understand the nature of the poor tie above the HRZ. These results show how the seismic reflections interfered with each other, causing the different onsets (peaks and troughs) to either partially/totally cancel themselves, or increase their magnitudes, therefore, false AVO signatures were produced while other amplitude responses were masked. These effects might have happened in response to the thin thickness of the shallower events (high slope channels) which are not seismically resolvable (thinner than the vertical resolution), due potentially to lateral lithology variations caused by the depositional pattern established by the slope feeder channels above the HRZ, due to the AVO amplitude anomalies caused by the presence of hydrocarbons, and possibly, due to the time migration applied to the data.

The vertical resolution (minimum resolvable distance) was calculated to be between 21 to 25 m, considering an average interval velocity range of 2900 to 3100 m/s, very characteristic range of values for typical Alaska sands. Frequency values were calculated from the frequency spectrum and the wavelets used to calibrate the data, which resulted to be between 30 and 36 Hz respectively. The Fresnel Zone (Horizontal resolution) was estimated to be between 135 and 160 meters (post-migration).

Time structural maps were generated from all the interpolated markers (24), with all the horizons, including the HRZ (High Radioactive Zone), resulting with their contours having a north-east to south-west trend, and a noticeable west to east pattern that represents the foreset reflection configuration originated by a prograding slope system in standing bodies of water. The slope that defines this system dips in general towards the east,

indicating the west-to-east basin filling pattern characteristic of the North Slope of Alaska (Figure 4). The shape and angle of repose of sediment on this slope system can be interpreted to be influenced by the composition of deposited material, sedimentation rate and quantity of sediment input, salinity of the water, water depth, energy level, position of the sea level and subsidence rate (Veeken, 2007).

Time structural maps, together with the seismic transect from Figure 4 suggest that the shelf margin of this stratigraphic sequence was located to the west on this survey, indicating at this time a west-to-east basin filling trend (Figures 4 and 11). This shelf margin represents a small portion of the entire shelf, which is known to have rotated towards the east as the foreland basin was getting filled up (Houseknecht and Schenk, 2001).

The time structural map that corresponding to the HRZ shows a subtle high or folding (anticline) towards the north-west with the lower most portion of this feature located to the south-east down the slope (Figure 11a). Time structural maps of markers E, I, J, and K (Figure 11b, c, d, and e) suggest the presence of a low (green to light blue contours) that follows the northern high to the south and appears to have gotten partially filled up as marker L got deposited (Figure 11f).

The depositional sequence on this portion of the NPRA was easily interpreted by generating a series of isochrons were the base horizon was the HRZ, and the top or shallower markers were surfaces that kept on getting younger respect to the first (HRZ)(Figure 12). The results were clinoforms originated by a prograding slope system with a west-to-east depositional trend reflected by contours with an approximate south-to-north pattern (Figure 12a, b, c, d, e and f).

Additionally, isochrons for individual intervals suggest that the depocenter of the bodies deposited on top of the HRZ constantly migrated with a northeastern-to-southwestern pattern, giving this way an idea of how the

sediments got deposited, by always looking for the lower part of the basin floor morphology (Figure 13). This behavior and geometry, normally is what reflects as a high-energy slope system and it points to little change in the direction of the prograding slope. It also means a rather uniform filling-in of the basin, as a lot of switching of depocenters would result in different progradation directions. The seismic data used did not have a high enough resolution to solve all the sand bodies present in this area, therefore, the isochrons resulted with some of the bodies from Figure 13 possibly corresponding to more than one sand body or interbedded sands with shales. As a result, it was very hard to differentiate individual lobes, as it happened with interval F-G from Figure 13d that shows scattered shapes.

2. AVO MODELING

Two different types of AVO anomalies were found in the prestack synthetic gathers generated by modeling using a full elastic wave equation; a first Class II (Figure 8) described by a positive or close to zero intercept and a negative gradient (slope), causing an amplitude polarity reversal where a peak becomes a trough in the far offset, or a soft trough becomes more negative (increases its magnitude) in the far angles; and a second Class III, defined by a negative intercept and gradient, where a trough increases its magnitude in the far offsets (Figure 8).

The identified AVO anomalies were classified by letters, starting from A all the way to I. For those peaks underlying the mapped troughs which increased their magnitudes in the far offset (brightening), no analysis was done because these were considered to be a part of the Class III AVO anomalies described by the troughs overlaying them. Markers B, C, D, E and G appear to be Class III AVO anomalies on the synthetic shot gathers (Figure 8), although only C and G cover the desired conditions for further AVO studies: sandstone or interbedded sandstones with shales described by the GR log, a decrease in the P-wave velocity and an increase in the S-wave velocity, with their corresponding decrease on Poisson's ratio, and

lastly, a decrease in density and an increase in resistivity (Figure 14) that suggests an increase in porosity and potential hydrocarbon saturation. Marker B shows a rather strong increase in its gradient (Figure 8) but it does not show any variation in its P-wave sonic. The anomalies described by markers D and E on the shot gathers are not sharp enough (small gradient increase) to be considered AVO anomalies, probably because the thicknesses of these sandstones are not seismically resolvable, therefore, seismic signal mixing occurs and causes the reflections to interfere with each other, resulting in either masking or amplifying the true seismic responses as explained in the exploded synthetic from Figure 7. Finally, letters A, F, H and I describe Class II AVO anomalies, with letter A describing a possible false AVO signature due to its high and Poisson' ratio values (0.27) and no P-wave velocity variation. The rest of these markers (F, H and I) cover the desired conditions to be potential areas for further AVO studies (Figure 8).

Table 2 summarizes the amplitude responses of the synthetic shot gathers to increasing offset by describing the intercept and gradient of individual seismic markers (horizons) and intervals in the cases where either sandstones or interbedded sandstones with shales were present between interpreted horizons. In many cases false AVO signatures were modeled, which were expected results due to the thickness of many of the shallower events (High slope channels) that were not possible to resolve seismically (below seismic resolution), therefore, caused seismic signal interference. Additionally, a low signal to noise ratio, the type of migration applied to the data, and lateral lithology variations could also have affected the modeling results. There are also, some general factors that can produce AVO anomalies in different scenarios, such as reflector dip and depth, receiver array attenuation, inelastic attenuation, thin bed effects, anisotropy, tuning effects, incorrect seismic processing sequences applied, and the presence of specific fluids.

With the AVO modeling results obtained by using the full elastic wave equation, near and far angle ranges were selected in order to generate angle stack seismic files. The angle ranges were from 0 to 20 (near) and from 30 to 40 (far) degrees (Figure 5). As Figure 8 shows, the synthetic shot gathers suggest that the AVO anomalies present in this area are described in two different ways:

1) A peak (e.g. marker I from Figure 8) in the near angles (0 to 20 degrees) becomes a trough in the far angles (30 to 40 degrees), experiencing what is called a phase reversal, where the peak becomes a trough and defines a Class II AVO anomaly. Alternatively, a small trough, close to zero, (e.g. marker A from Figure 8) can also become a stronger trough in the far angle and still be considered the same type of AVO anomaly. This change in amplitude values is described as a negative gradient or slope.

2) A well defined trough (e.g. marker C from Figure 8) in the near angles, increases its magnitude in the far offset, making the event brighter and describing a Class III AVO anomaly with a negative gradient (slope).

Based on the previous definitions of AVO anomalies, we will now call a negative intercept a trough and a positive intercept a peak, whereas the gradient or slope for both types of anomalies described will be negative (see Appendix A for further AVO theory and examples).

With the AVO anomalies defined and the angle stack seismic files generated, seismic attributes were extracted from both the far and the near, then the difference between them was calculated to obtain the amplitude variation with increasing offset for those horizons that had an AVO signature in the shot gathers. This difference, for the purpose of this study, will be referred to as sweet spots. Additionally, a gradient cube was generated using the original shot-gathers to be used as a lithology discriminator and to validate the amplitude anomalies.

3. SEISMIC ATTRIBUTES

With the angle stack files and the modeling results, a number of amplitude and complex trace attributes were extracted by using the full stack (AVO compliant), and the near and far angle stack seismic files. The objective was to try to identify and map the same amplitude responses described by the Class II and III AVO signatures obtained by modeling the synthetic shot gather, but this time, on the seismic volumes. This means that given the conditions of a specific rock to be considered for a further AVO analysis, we would expect troughs and/or subtle peaks to have a high enough gradient to either become a trough (Class II anomaly) or become a stronger trough in the case of a Class III AVO anomaly.

Marker J is defined seismically as a weak trough close to the top of a clean thin sandstone at the Well A location (Figure 14 and 15a). This marker represents a possible high slope channel system with a number of north-west to south-east feeder channels to a submarine fan system located at the base of the slope (Figure 15b), with one located outside of the seismic subcube boundaries (southernmost one). These feeder channels were possibly formed as high-density currents eroded through submarine canyons created on areas of the slope where traction currents produced significant erosion. The resulting submarine fans can be sand-rich, such as the Crati submarine fans off-shore Italy, or shale rich like the Amazon cone located offshore South America (Rebesco et al., 2009).

Since the seismic character of this marker is a trough, the maximum trough amplitude and the average trough amplitude extracted from the fully stacked seismic file (AVO friendly version) captured the geomorphology of these high slope channels close to the shelf edge (Figure 15c). As predicted from the AVO modeling results (Figure 8), the attributes extracted from the near and the far angle stacks, described amplitude magnitudes increasing with increasing offset for the trough that represents the top of the sand (Figure 15d and 15e). These AVO buildups (sweet spots – Figure 15f)

that characterize some of the feeder channels can be estimated by subtracting attributes extracted from the far with the near angle stacks, and potentially can be exploited to directly detect reservoirs and/or indicators of subtle lateral changes in the elastic parameters of sandstones (Figure 15d, 15e, and 15f).

The average reflection strength and total energy, two of the complex trace attributes that were calculated, give access to the imaginary part of the seismic trace, which gives a better handle on the lateral continuity of the reflections (Figure 16). By extracting these two from the near and the far angle stacks the amplitude increases with increasing offset that define this Class III AVO anomaly should be, in theory, better delineated (Figure 16a, 16b, 16d, and 16e). By calculating the difference between both, what we defined as sweet spots are isolated, and should represent the extension of the sand identified on the GR log (Figure 8). Some noise content due to manual picking and the attribute analysis window size is always incorporated as Figures 15f, 16c and 16f show, where some of these values tend to increase the size of the delineated sweet spot.

Figure 17 has the result of 4 different trace attributes displayed on top of seismic marker J in a 3D-visualization software (Geoprobe from Landmark Graphic). Additionally, it has displayed a time structural map (Figure 17a) and the time-migrated full stack seismic file (Figure 17b). The time structure map indicates the same low structure located towards the north-west of the survey that was mentioned in Figure 11d, and that could represent a potential area for sediment deposition by the feeder channels cutting down the slope characterized by a trough (as a seismic character)(Figure 11b). The results of the semblance, sweetness, and instantaneous phase (Figures 17c, d and f) suggest the presence of three rather continuous features; a first to the north-west of the area not easily visualized with the horizon based attributes, a second to the south to the first body identified, and a third towards the southernmost part of the survey. The gradient

(Figure 17e), an attribute normally used for lithology differentiation, identified the three same feature, and within them two different types of responses; a first on yellow-to-orange, that follows the trend of the high slope channels and are suggested to be at least partially filled with sands by the GR log from Figure 14, and a second in blue, that could be filled in by either shales or interbedded sands with shales.

The gradient volume displayed on marker J (Figure 17e) shows negative values (negative slope) on top of some of the AVO anomalies already described by the horizon based seismic attributes on Figures 15 and 16, therefore, it makes more robust the sweet spot definition obtained by calculating the difference between attributes extracted from the far and the near angle stacks.

Furthermore, this marker (top of sand) is described by a decrease in P-wave velocity, an increase in S-wave velocity, a decrease in Poisson's ratio (characteristic of fluid filled reservoir), a decrease in density (suggesting an increase in porosity), a Class III AVO anomaly described in the synthetic shot gathers (Figure 8), and an increase in resistivity that suggest the presence of hydrocarbon (Figure 14). Additionally, the isochron from markers I to J (Figure 18b) indicates that the thickest portion of this interval are located on the same places of some of the interpreted amplitudes anomalies, suggesting that the extensions of this package are at least partially sandstone. The same results were obtained for seismic markers (horizons – markers in blue from Figure 8) H, K and L (Class II), and intervals AB – Sub Ba (Class II), Sub Ba – Sub B (Class II), Ca – D, and E - F/Ea (Figure 8, Table 2 and Appendix f: Map database).

False AVO signatures can be caused by many reasons, and can easily convince the interpreter that there is an amplitude variation with offset due to the presence of hydrocarbons. On Figure 8, seismic marker I (on top of anomaly signature D – in red letter) represents a good example of a false AVO signature. The calculated Poisson's ratio does not decrease even

though its synthetic shot gather shows a negative intercept and gradient (Class III AVO anomaly characteristics). In this case, where the gathers do indicate an amplitude increase with increasing offset, the seismic attributes will respond in the same way (Figure 19), and will result in the definition of a false sweet spots (Figure 19f). For marker I it is easy to look at the computed Poisson's ratio and the density log. Its Poisson's ratio is basically a straight line and has values of approximately 0.3 (not a characteristic shale/sand value when saturated by hydrocarbon), whereas the density log shows a very small decrease in density, suggesting that there is a bit of an increase in porosity, but most probably not significant enough to produce an AVO anomaly as well as that of other markers and intervals (Table 2 and Appendix F). This anomaly could be in response to the presence of brine, seismic signal interfering due to thicknesses below tuning effect, low signal to noise ratio, and the time-migration applied to the data, which is a very subtle migration algorithm, not perfect but clean enough to migrate the seismic events to approximately their real depths considering that there is no structure in the area. Marker I, as Figure 19a shows, this marker (I) is a strong trough that represents the base of a sand below seismic resolution. Figure 19b suggests that this thin sand was deposited regionally and when attributes are calculated from the full stack time-migrated file they clearly define the high slope channel system (Figure 19c), as marker J did (Figure 17c). The main difference between marker I and J is that the increase in amplitude from near to far angles stack for marker I (Figure 19d and e, and Figure 20a, b, d and e) are not as big as those for marker J (Figure 17d and e), therefore the difference between attributes extracted from far and near angle stacks is blurry when compared to that of marker J (Figures 17f, 19f, 20c and d).

Even if these feeder channels to fans are not filled with porous sand, they do still define the morphology of the high slope channel system, and it can be easily appreciated in some markers up to a level at the beginning of the developing fans down the slope (Figure 20b and 20e).

A summary of randomly selected RMS amplitude horizon based maps extracted from the far angle stack seismic file for 9 markers is displayed in Figure 21. This composite figure shows how the seismic attribute captured geometries that correspond to the foreset reflection configuration originated from the prograding slope system in standing bodies of water. As mentioned, some of these correspond to false AVO signatures (see Table 2 for individual marker AVO response description). Furthermore, Figure 22 shows a summary of the difference between maximum trough amplitudes extracted from the far and the near angle stacks, which in some cases resulted in what we defined as sweet spots, but in others, false AVO signatures caused maybe by the same feeder channels but with a different sediment fill. See Table 2 for further detail regarding the nature of the AVO signatures for each interpreted horizon.

DISCUSSION

1. DEPOSITIONAL GEOMORPHOLOGY

Previous work based on logs, core and 2D/3D seismic data suggested that the Torok Formation exhibits the overall seismic geometry of bottomset-clinoform-topset strata that indicates an eastward to northeastward migration of a depositional system that includes deposits of the deep marine basin, marine slope, and outer shelf (Molenaar, 1985, 1988; Houseknecht and others, 1999). Additionally, in the bottomset environment, submarine fans have been identified near the base of the slope onlap. They are characterized by a radial pattern that increases in width into the basin (McMillen, 1987). Part of this study integrated well logs with 3D seismic data and described a prograding clinoform system with an eastward to northeastward trend that represents the direction of the basin filling. The seismic survey used is located on top of a relatively steep slope with a gradient of 4 to 5 degree, and displays part of the shelf break to the base-

of-the-slope and parts of the slope-to-basin transition. On this transition zone, a canyon system formed by the erosive action of sediment gravity flows. These later formed feeder channels higher up the slope, with some of these converging into the slope with a steep gradient, causing a rather sharp channel path instead of a meandering trend as it would normally be expected from low angle slopes. Soon after, these channel feeders formed an unconfined submarine fan system located down the slope as illustrated on the block diagram (Figure 23). Some of these features can be seen on the GR log from Well A (Figure 9 and 14), which describes one of the turbidite lobes (from marker HRZ to E) plus part of the high slope channel system (from marker H to K) (Weimer and Slatt, 2004).

2. AMPLITUDE ANOMALIES

By modeling synthetic shot gathers using a fully elastic wave equation, Class II and III amplitude anomalies were predicted for the Alaska sandstone corresponding to the Torok Formation. These amplitude anomalies are named by letters from A to I, with letters A, F, H and I describing possible Class II AVO anomalies (positive or very subtle negative intercept and a negative gradient), and letters B, C, D, E and G describing probable Class III AVO anomalies (negative intercept and gradient) (Figure 8).

From the identified AVO signatures, only markers C, F, G, H and I were interpreted as real Class II and III AVO anomalies, with all characterized by a decrease in P-wave velocity, and increase in S-wave velocity, a decrease in Poisson's ratio (characteristic of fluid filled reservoirs), an increase in porosity (suggested by a decrease in density) and either a peak (positive intercept) or a trough (negative intercept) with a negative gradient (magnitude increasing in the far offset). Marker A described a classic Class II AVO anomaly in the synthetic shot gathers, although it's Poisson's ratio is equal to 0.27 (Figure 8), which is not a characteristic hydrocarbon value but close to a brine (water containing salt) value. Additionally, it has little if any

sand content. Markers B and D, have a very soft increase in their gradient in the far angles, plus, no sandstone and high Poisson's ratio (>0.27), therefore, these two were also considered false AVO signatures due most probably to the seismic signal interference (Figure 6). Lastly, marker E, covered all the prerequisites of a Class III AVO anomaly, including a 0.24 Poisson's ratio (Figure 8), which is a value within the oil window (0.15 – 0.25), although it's gradient (amplitude magnitude variation) in the synthetic shot gather is considerably small. Most probably, its AVO signature got either masked or partially erased by the signal interfering of other events above and below, which are thin shales and sandstones.

Not all the seismic markers coincide with the location of these amplitude anomalies, since some of these correspond to seismically irresolvable lithologies due mainly to two reasons: 1) event thickness (below seismic resolution) and 2) different resolutions between the wireline logs (higher) and the seismic data (lower). From those that did coincide with either sandstone or interbedded sandstones with shales, and additionally have porosity, suggested by a decrease in density (Figure 8) and potential hydrocarbon saturation (high resistivity) (Figure 14), the most prospective seismic markers (horizons – blue letter on Figure 8) are, markers J, K and L, and intervals AB-to-Sub Ba, Sub Ba-to-SubB, Ca-to-D, and E-to-F/Ea. Due to the low number of wells penetrating these amplitude anomalies it is hard to determine with high precision what causes them, although based on the AVO modeling results and the wireline logs (Figure 14) we can assume that slower sandstones with porosity, a high resistivity and a decrease in the Poisson's ratio values, which is a very characteristic response of fluid filled reservoirs, are the main causes, although it is important to keep in mind that amplitude anomalies can also be caused by reflector dip and depth, receiver array attenuation, inelastic attenuation, thin bed effects, anisotropy, tuning effects, presence of other fluids, and incorrect seismic processing sequences applied. In this particular case, and with the

available data for analysis, we believe that the false AVO signatures present in our data could be due to the following reasons:

a) Seismic signal interference caused by events that are too thin to be resolved by our seismic data. Therefore, as the exploded synthetic shows (Figure 6), amplitudes cancel or add up resulting in stronger/weaker peaks and/or troughs that cause smearing of the signal and end up producing false AVO signatures.

b) The seismic data used was time-migrated, which uses a relatively mild algorithm with the objective of moving the dipping events to their real position, and even though this is a clean process normally applied for AVO complaint data, it is not perfect. In order to move the events to a more accurate position a depth-migration should be done, although this represents a big cost increase and it is normally done in the presence of structures.

c) Strong lateral lithology variations due to the depositional environment (turbidites/basin floor fans). As the GR from Figures 8 and 14 show, there is a high slope channels system that transport sediment toward the basin, where they possibly deposit as fan/lobes. Furthermore, there are also interbedded sands with shales above the HRZ that represent a lower fan system, which will have plenty of lateral lithology variations due to their depositional pattern.

d) Low fold (20 traces/CDP) that results in a low shallow resolution and a low signal-to-noise ratio (noise data).

In summary what can be inferred from these results is that this AVO study indicated the presence of an increase in amplitudes as a function of increasing angle of incidence (offset), which can be exploited to directly detect some reservoir characteristics as porosity, or as a tool to infer lateral changes in the elastic properties of sandstones, although, due to the reduced well number, it will be hard to quantify these values with high

accuracy. The analysis done is not enough to conclude that the anomalies are due to the presence of fluid reservoirs without the results of a fluid substitution modeling.

3. SEISMIC ATTRIBUTE ANALYSIS

Extracting amplitude and complex trace seismic attributes from the far and near angle stacks allowed to get a first general estimate of the amplitude anomalies present in the Torok Formation, although due to seismic resolution limitations, many of these sandstone bodies could not be studied independently and had to be analyzed as an interval, meaning that if volumetric were to be calculated, it would represent a challenge on how to estimate the thickness of each of these sandstones, or how to estimate what percentage of the interval would be sandstone, assuming that this rates will stay constant between wells where the interval is present.

The canyon system alongside the feeder channels that formed the submarine fans were better delineated by using the trace attributes results calculated from the fully stacked seismic cube (Figure 17). Some of these attributes, like the sweetness and the gradient helped validate the previously extracted horizon based seismic attributes from the angle stacks, by matching their sweet spots (sweetness) and their negative gradient (gradient), which indicate locations where there is a negative slope that describes the AVO anomalies (Figure 17).

Due to the eastern seismic data boundaries the submarine fans that presumably developed from the feeder channels coming down the slope could not be visualized nor mapped, so only the high slope channels up to the slope-to-basin transition were captured with the seismic attributes, specially from the far angle stacks due to the increased amplitude values where the anomalies are present (Figure 15 and 16).

CONCLUSIONS

1. Clinoforms of the Torok Formation prograded to the east/northeast representing the North Slope basin filling direction in the NPRA. The bottomset in this study are characterized by a steeply graded slope (4 to 5 degrees) that has a canyon system probably eroded by sediment gravity flows that later formed high slope feeder channels that converge as they passed through the slope-to-basin transition zone and formed submarine fans down the slope that now represent potential highly complex reservoirs.
2. Class II and III AVO anomalies were identified and mapped by integrating the AVO modeling results generated by using a fully elastic wave equation, with seismic attributes extracted from the near and far angle stack seismic files, with seismic markers J, K and L, and intervals AB-to-Sub Ba, Sub Ba-to-SubB, Ca-to-D, and E-to-F/Ea as the most prospective due to a suggested increase in porosity (decrease in density log values), a decrease in the P-wave velocity, an increase in the S-wave velocity, a decrease in Poisson's ratio (characteristic response of fluid reservoirs) and an increase in resistivity (characteristic hydrocarbon response).
3. This AVO study indicated the presence of an increase in amplitude as a function of increasing angle of incidence, which can be exploited to directly detect some reservoir characteristics as porosity, or as a tool to infer lateral changes in the elastic properties of sandstones. False AVO signatures were caused by seismic signal interference due to events thicknesses below the seismic resolution, low signal-to-noise ratio (low fold), lithology lateral variations (anisotropy), and the type of migration algorithm applied to the data, which was not strong enough to entirely correct the events to their real depths.
4. The methodology used in this case study has demonstrated the usefulness of prestack elastic synthetic modeling for lithology interpretation and sweet spot delineation by correlating, extrapolating and doing a few

mathematical manipulations with the AVO modeling results and the seismic attributes extracted from the near and far angle stacks. This workflow can be implemented if the proper data are available (time-migrated shot gathers when no structure is present, depth-migrated with structures present, P-wave and S-wave sonic logs) to delineate exploration and development plays within different depositional environments around the world, although it is important to always remember that as with any other seismic attribute, it will need to be calibrated with well data.

ACKNOWLEDGEMENTS

I will like to give special thanks to my family, Julio Herbas (father), Nelida de Herbas (mother), Andreina Herbas (sister) and Aaron Mendez (brother in law) for all the support and strength they gave me throughout the course of my Master Program, and to my girlfriend Michaela Bjorseth for helping me by being supportive and being very patient while I was writing this thesis. Without all you guys I could not have finished my M.Sc.

I wish to thank Petro-Canada, who cordially sponsored the thesis project over its duration and contributed with great technical and intellectual discussions via my mentors, namely Wayne Park and Andrew Willis; WesternGeco for providing the 3-D seismic survey and allowing me to publish the result of this study. Special thanks to Jeff Bever (Alaska Team Leader) and Derek Evoy (Alaska Regional Manager) for giving me the opportunity to work in their team while doing my M.Sc. thesis; to Todor Todorov for his assistance with the AVO Modeling and analyses, Anne Halladay for all the attribute analysis discussions; to my very good friend Cindy Koo for going over my thesis several times and for the great times in the mountains during the course of my thesis; to Tim McCullagh for allowing me to use his thesis as a guide; to Gerardo Franco for all his AVO technical advice; to Dylan Dersch for his ideas, and to Dr. Bruce Hart for all his guidance, suggestions and thesis corrections.

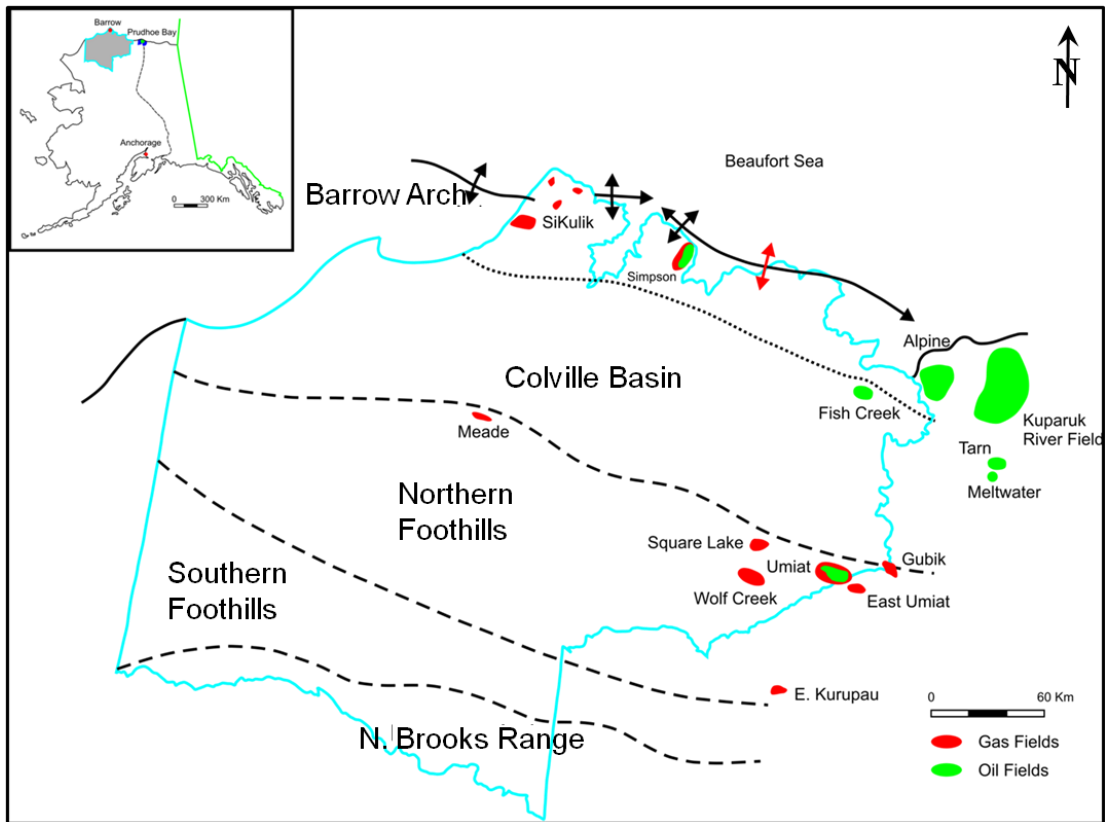


Figure 1. Base map displaying major geologic provinces within the NPRA (boundary indicated by cyan line), namely, the Barrow arch, the Colville foreland basin, the Foothills fold belt, and the Brooks range overthrust. These provinces overlap to varying degrees, but can be divided on the basis of geologic history affecting known and possible petroleum occurrence (Montgomery, 1998). Some of the known oil and gas accumulations are displayed on the map on green and red respectively. The seismic survey used is within the northern part of the NPRA. Its exact location cannot be reveal due to confidentiality agreements. Additionally, the map includes the location of the Tarn and Meltwater fields, which are two of the most recent discoveries made on bottom-sets on the North Slope of Alaska, plus the Kuparuk River Field, which is the second biggest in North America following Prudeau Bay.

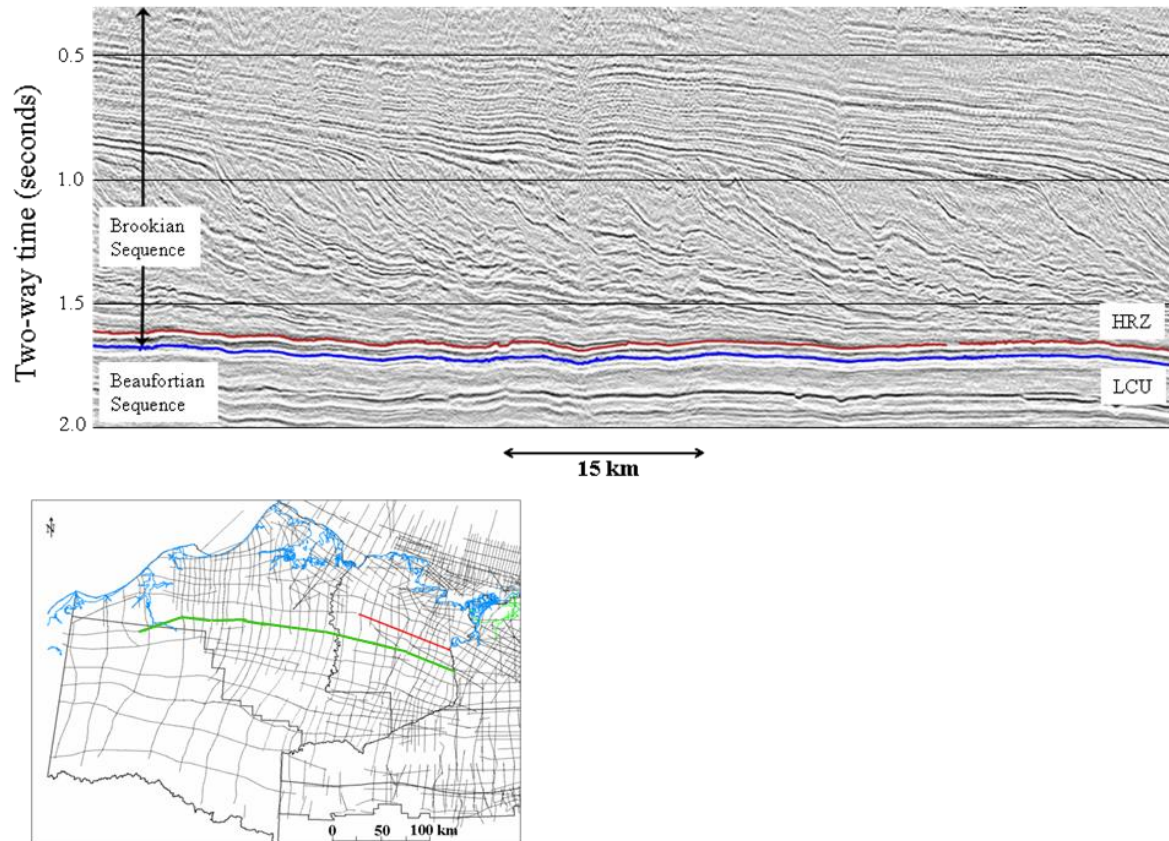


Figure 2. Seismic expression of Brookian depositional style in the eastern part of the NPRA showing topset, clinoform, and bottomset strata geometries and relation to the LCU and Beaufortian sequence. Location of this 2D seismic section is displayed with a red line on base map (left). A secondary green transect is displayed on the base map which represents the west-to-east orientation of the seismic section from Figure 4

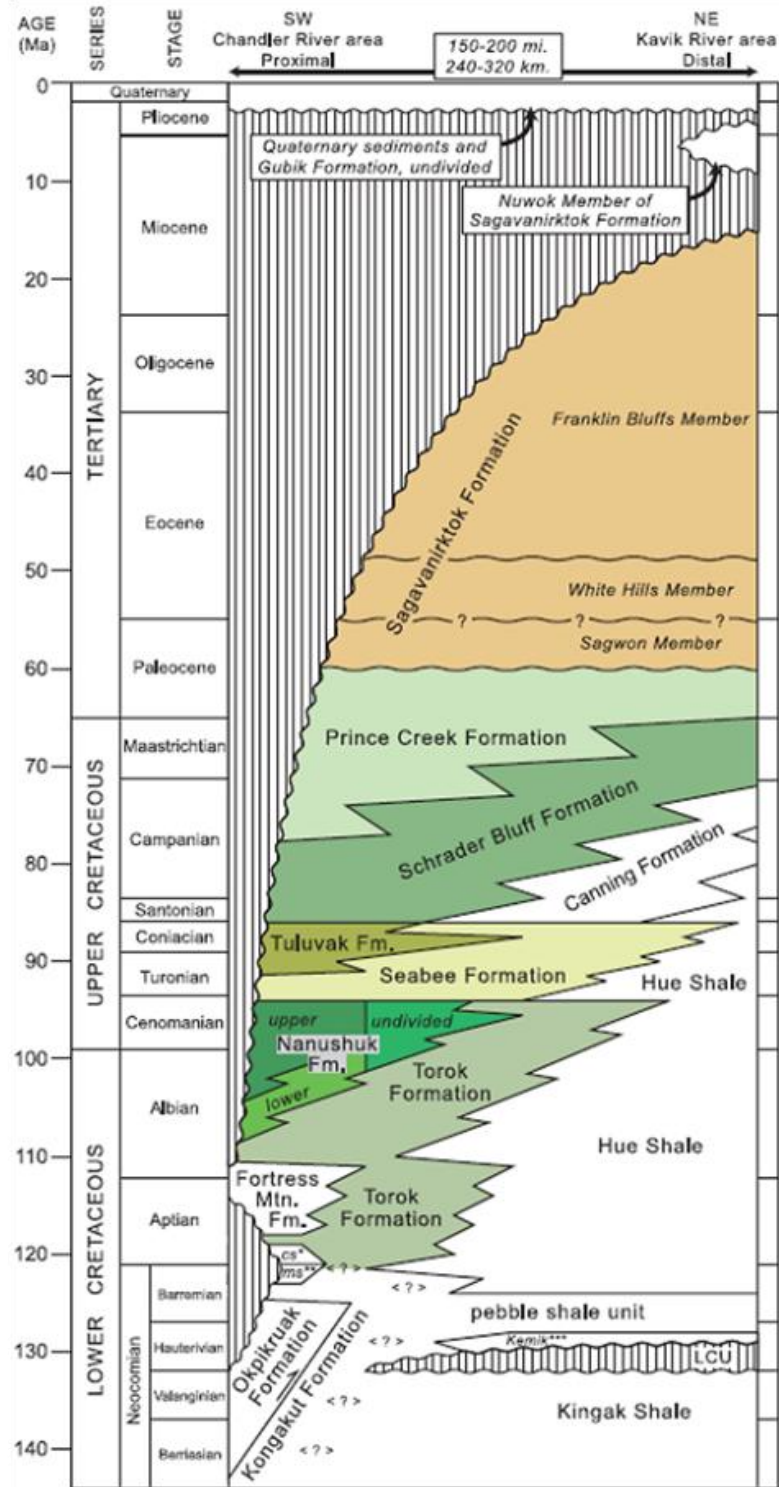
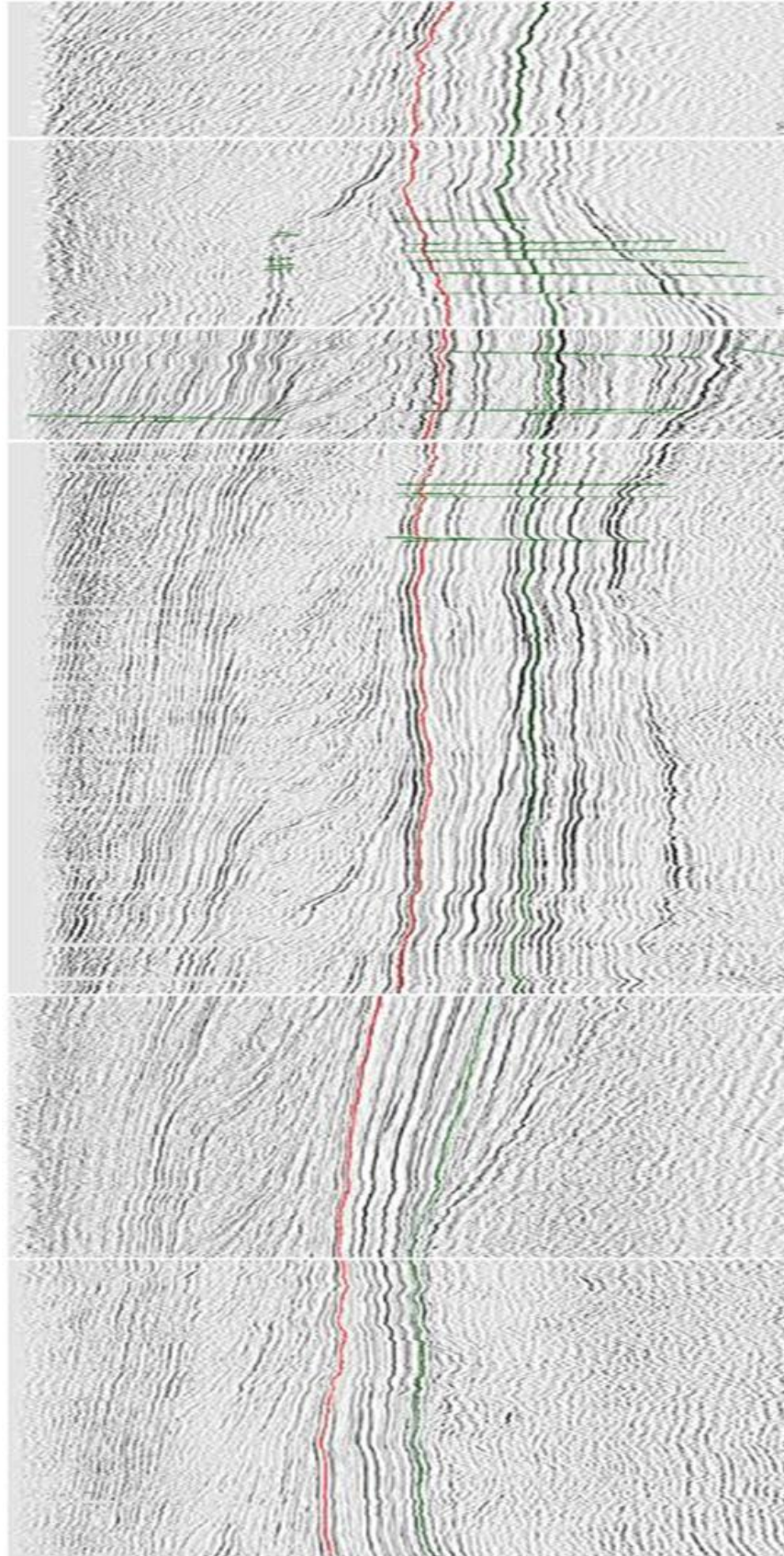


Figure 3. Chronostratigraphic column for the Colville foreland basin, northern Alaska, showing revised stratigraphic nomenclature and ages of units (Mull et al, 2003).

Figure 4 .West-to-east transect built out of 2D lines extracted from the USGS (Unite States Geological Survey) data base. Two strong reflectors were interpreted; the LCU (upper in red), and the Shublik (lower in green), plus the major faults towards the east. Above the LCU lies the HRZ (one of the well known source rocks in the NPRA), which has on top prograding clinoforms towards the east that represent the basin filling pattern. Location of this transect is displayed on top of a base map on Figure 2 with green.

East



West

Figure 5. Seismic section with a west-to-east orientation with 4 different seismic files: a) full stack time-migrated seismic data processed with a non AVO friendly sequence, b) full stack time-migrated seismic data processed with an AVO friendly sequence, c) near angle stack seismic data generated by stacking shot gathers from 10 to 20 degrees, and d) far angle stack seismic data generated by stacking shot gathers from 30 to 40 degrees. All the sections have well A overlain, which has a GR log (purple) displayed on its left, a sonic log on its right (green), and a synthetic seismogram in the middle (green). Amplitude increases between the near (c) and the far (d) angle stacks are very prominent and easy to visualize, in particular on some of the troughs closer to the left of the section. The full stack time-migrated seismic file (a) was used for horizon picking since the events are more continuous, although for seismic attribute extraction purposes, the AVO friendly was the one used because the compliant processing sequence applied preserves the amplitudes.

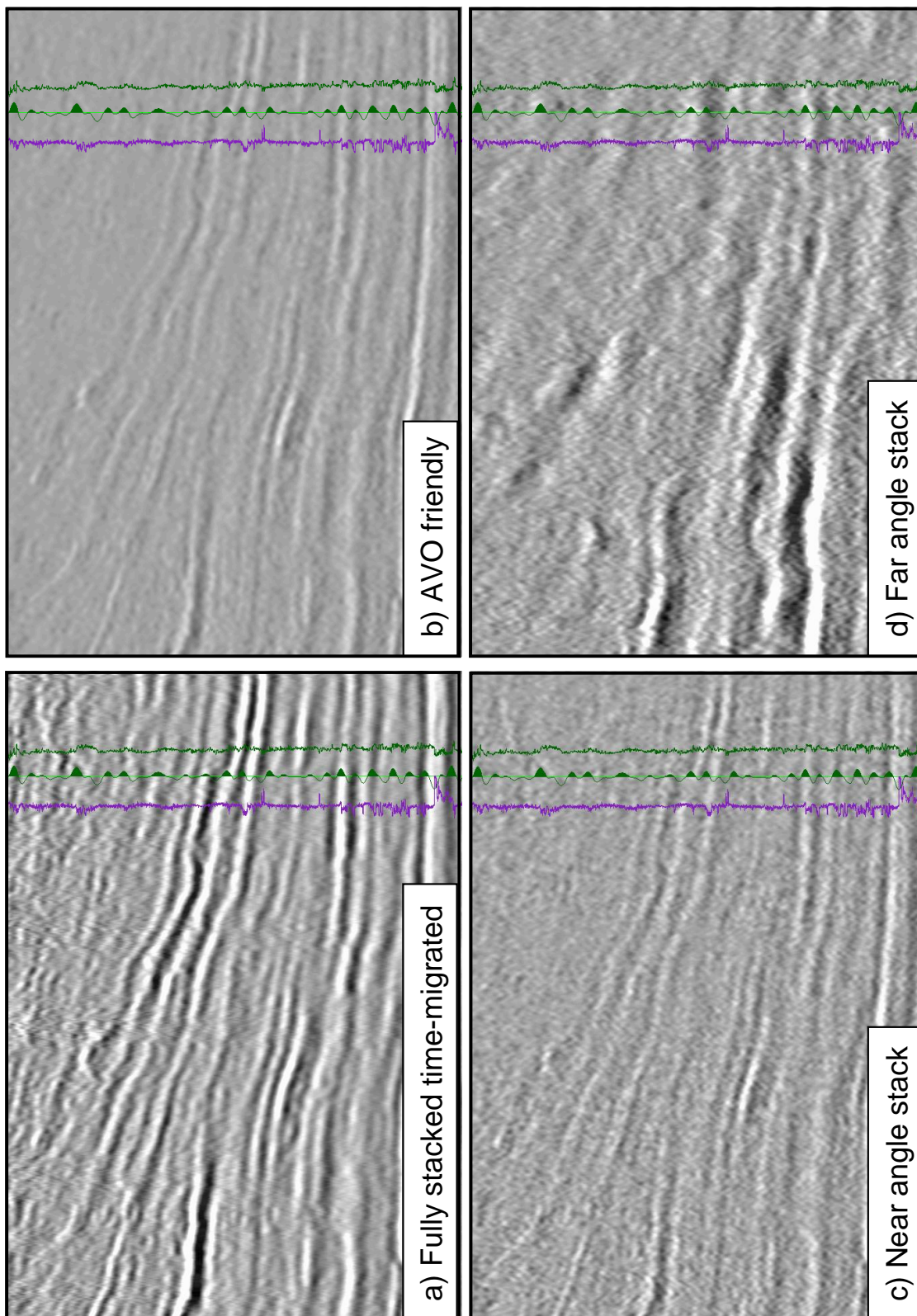


Figure 6. Well A displaying zero-offset synthetic seismograms generated with three different types of wavelets (Butterworth, Ormsby and Ricker). Best result was achieved with the 10, 18, 50, 72 Hz Butterworth with no phase rotation. Two strong markers (HRZ and LCU) used for calibration are displayed at the bottom. GR logs are displayed on the left (purple curves) and DT logs to the right (green curves). High slope channels (shallower) and the basin floor fans (deeper – above the HRZ marker) are displayed on the GR log. Synthetics seismograms have not been stretched nor compressed in order to try and preserve velocities as much as possible. Yellow rectangles show the correlation window used, with the best values achieved at the bottom below the HRZ and LCU markers, whereas above these, the ties were rather poor, possibly due to the event thicknesses (below seismic resolution), lateral lithology variations, and/or the type of migration (time migration) and algorithm used. See Figure 6 for exploded synthetic.

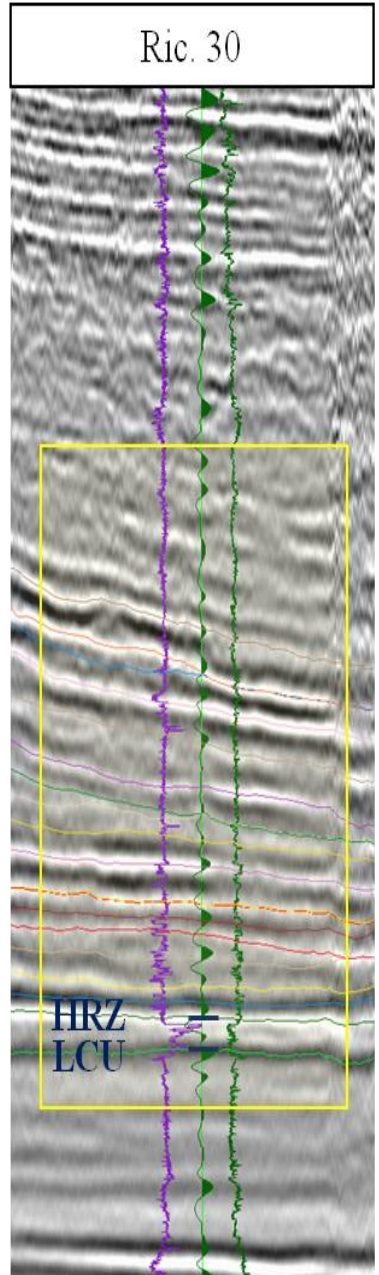
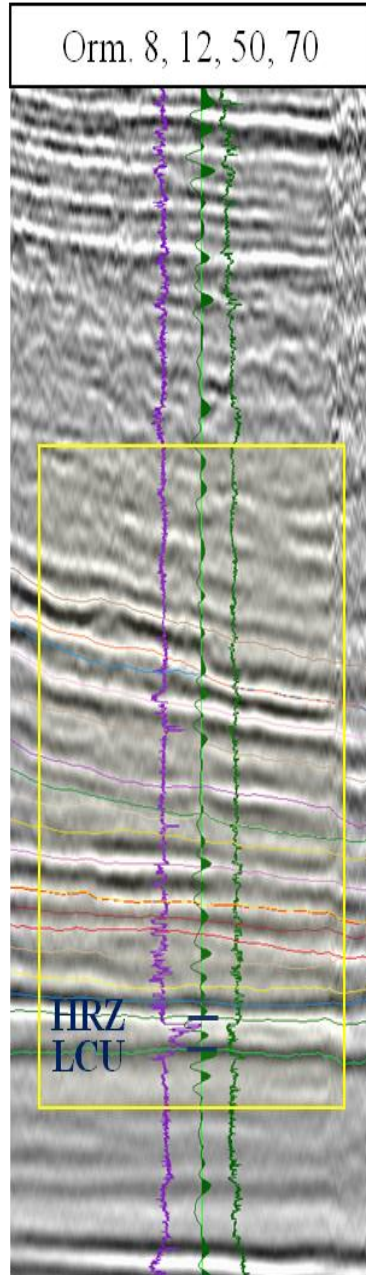
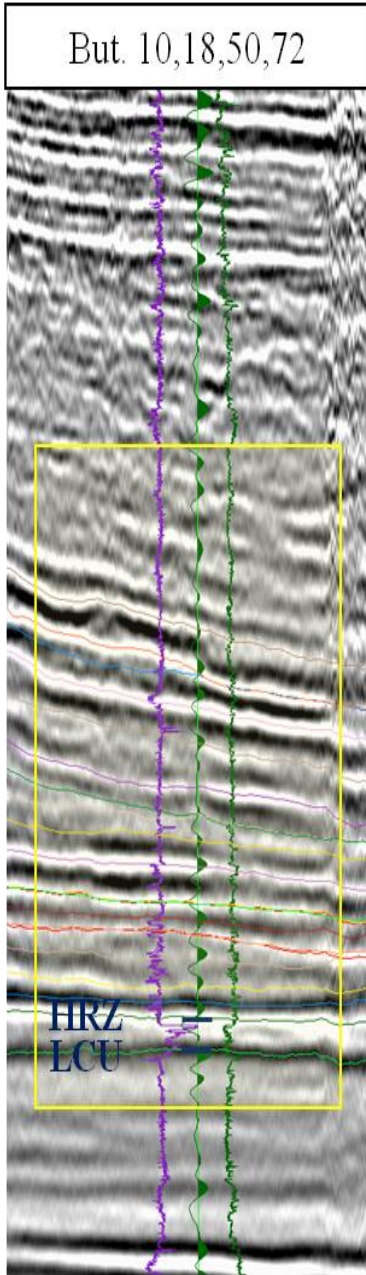


Figure 7. Exploded synthetic seismogram for well A generated by reducing the resolution of both, the DT(red in far left) and the RHOB (blue in far left) logs, by forcing them to have a maximum of 100 blocks. From left to right, the exploded synthetic is located in the middle with red and blue colours to differentiate from one trace to the next; the synthetic seismogram, product of adding the individual traces displayed by the exploded synthetic, is in black to its right; and lastly the full stack seismic file is located to the far right. Fifteen Torok Sand markers are activated with a red horizontal line across the entire display for analyses purposes. The exploded synthetic shows on top of each of these Torok Sand markers how the amplitudes cancel or add up resulting in stronger/weaker peaks and/or troughs in the synthetic seismogram, therefore smearing some of the reflections and resulting in a poor synthetic tie as it can be concluded by correlating the synthetic with the Full stack seismic data.

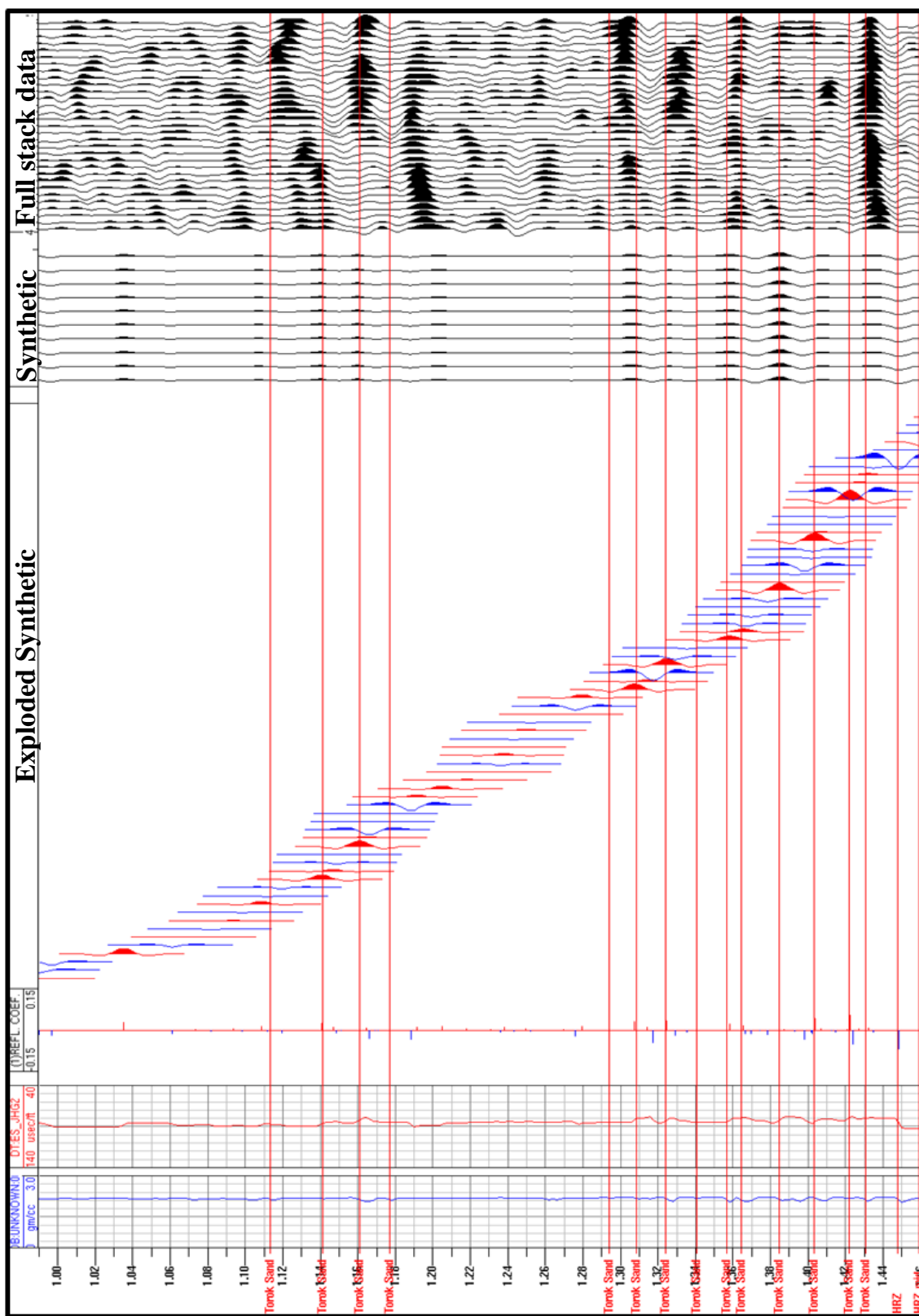


Figure 8. Synthetic shot-gathers for Well B generated with a full-elastic wave equation. Seismic markers present at this well location are displayed with small blue letters on the left. The word math on the well logs means that they have been filtered to reduce the noise content. Red and green arrows with respective letters above them, suggest what is interpreted as potential AVO anomalies Class III and II, respectively. As described on the exploded synthetic (Figure 6), the seismic reflections are interfering with each others, causing the different onsets (peaks or troughs) to either partially or totally cancel themselves, or increase their magnitudes, therefore, erroneous AVO signatures are produced within the synthetic shot gathers (far right). This effect is the result of having events thinner than the minimum resolvable distance by the seismic data. Markers A, F, H and I, appear to be Class II AVO anomalies, where a peak or a subtle trough becomes a strong trough in the far offset, whereas markers B, C, D and E come out as Class III AVO anomalies, defined as a trough increasing its magnitude in the far angles. From the markers with a Class II AVO anomalies response, A shows no P-wave velocity variation, has almost no sand, if any, and has a high Poisson's ratio, consequently it can be interpreted as a false AVO signature. From the markers with a Class III AVO anomaly response, B and D have no sand and have high Poisson's ratio values, therefore these can be consider false AVO signatures as well. The rest of the markers (C, G, F, H and I) are all characterized by a decrease in P-wave velocity, an increase in S-wave velocity, a decrease in density (suggesting an increase in porosity), a decrease in Poisson's ratio (typical response of fluid-filled reservoirs) and a Class II or III AVO signature (shot gathers)

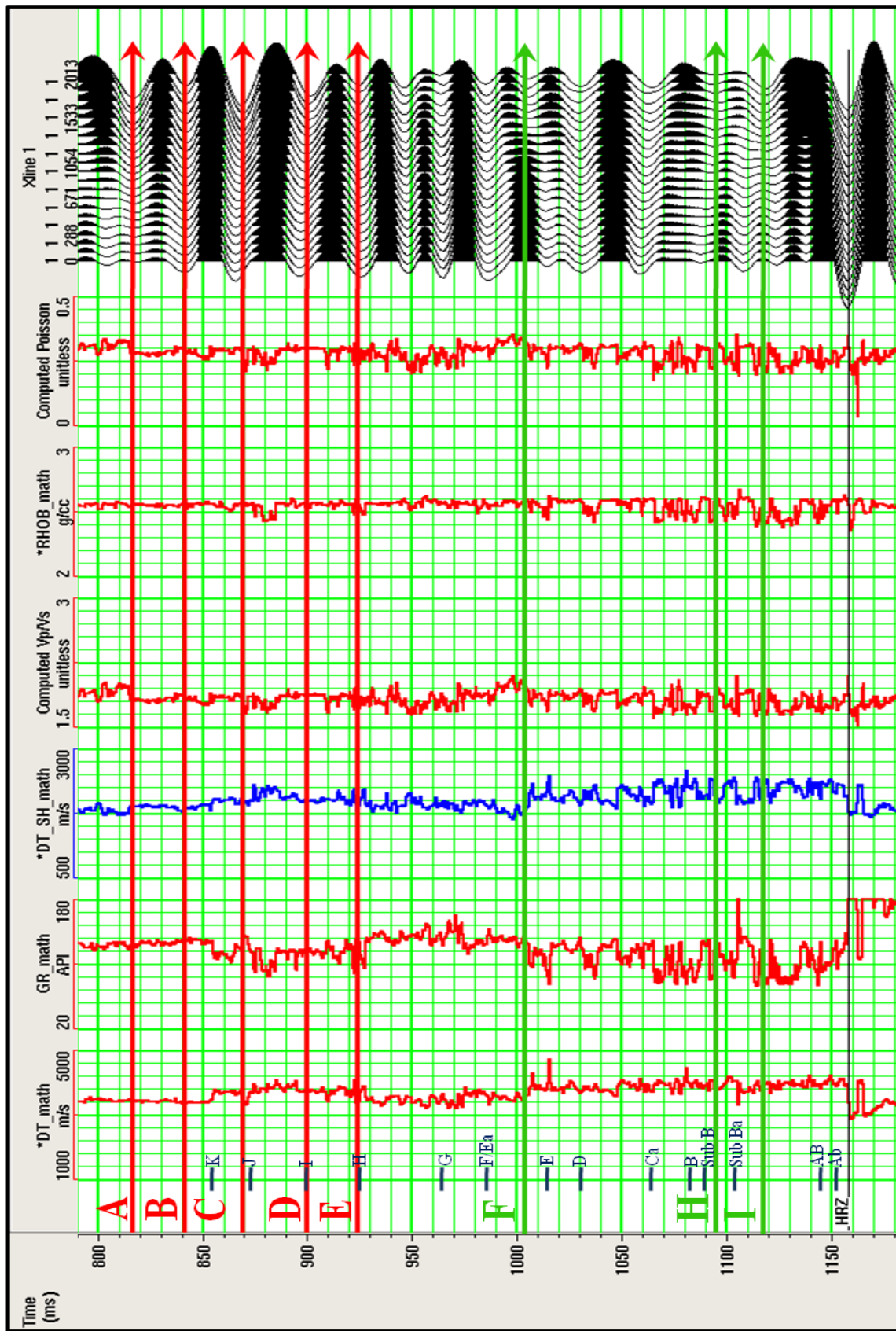


Figure 9. Seismic section with Well A displayed on top of the fully stacked time-migrated seismic data (not AVO friendly). The well has displayed a GR log (left), a DT log (right), and a synthetic seismogram (center). These logs together show the seismic character of 17 of the main interpreted markers. The lower portion of the GR (above the HRZ up to Torok E) shows interbedded sands with shales that represent the lower fan system, whereas above this interval, the present sands correspond to high slope channels. As the GR shows, the thickness of some of these sands at this well location are considerably below the seismic resolution, making it impossible to map as individual packages, so they were mapped as groups between the two same most proximal onset types (e.g. from trough to trough). As explained with the exploded synthetic (Figure 6), the well-to-seismic ties above the HRZ are poor due to unresolvable events by the seismic data, time-migration and algorithm applied, AVO anomalies present, and lateral lithology variations due to the deposition environment (turbidites/basin floor fans).

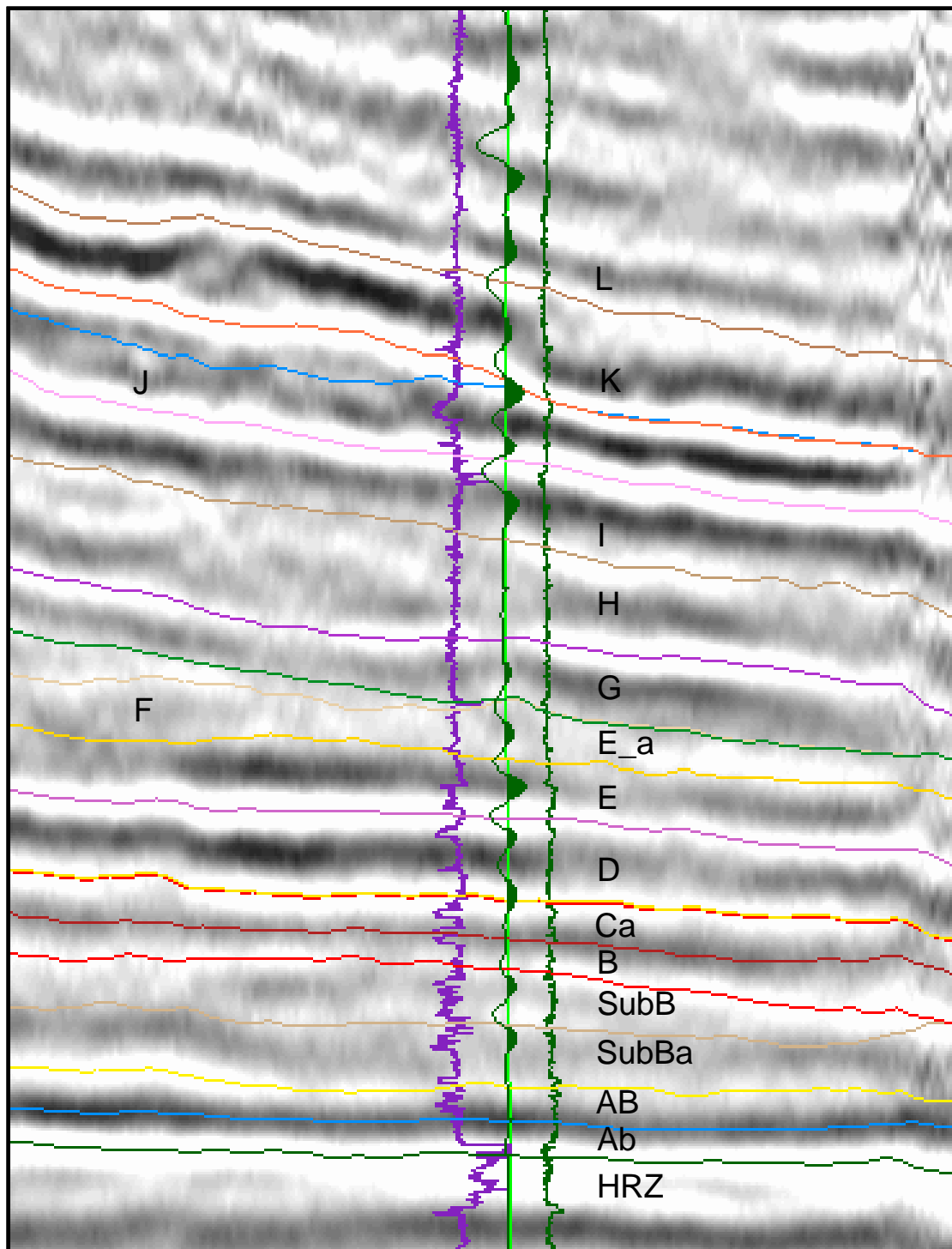


Figure 10. Correlation from a time window starting at 0.6942 to 1.1065 ms from a synthetic seismogram generated with a 10, 18, 50, 72 Hz Butterworth wavelet from Well A. The polarity used was normal and the maximum correlation coefficient achieved was 0.673. The correlation coefficients suggested that a bulk time shift of 208 ms was needed plus a relative phase rotation of 6 degree, which was not corrected due to its numerical size. This synthetic was generated from the southernmost well, where the clinoforms tend to thin down. The low correlation could be due in part to the thickness of the high slope channels and the interbedded sands with shales being below tuning (below seismic resolution), lateral lithology variations caused by the presence of many channels, low signal to noise ratio, and/or the presence of the AVO anomalies above the HRZ marker

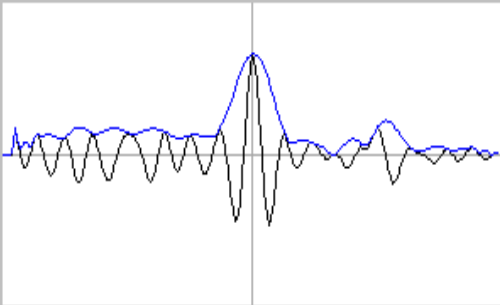
Trace Data

Synthetic: (1)Normal

Seismic: (1) SeisWorks 3D Proc Tr: 15

Start time: 0.6942 sec. End time: 1.1065 sec.

Phase Time



Max. amplitude envelope: 0.68
Correlation coefficient: 0.673

0 208.0 Total shift (ms)
6.0 Relative shift (ms)

OK Cancel Help

Figure 11. Time structural maps of markers HRZ, E, I, J, K, and L. Hot colours (towards yellow) indicate shallow values whereas colder (towards blue) are indicating deeper intervals. These time structural maps suggest that the highs are located to the west with a northeastern to southwestern orientation that dips towards the east, which follows the basin filling pattern of the North Slope of Alaska (Figure 13). The HRZ map suggests the presence of a subtle high or anticline (black arrow in map a) that thins as it passes down the slope to the south east, whereas as it gets shallower, markers I, J, and K suggest an additional pattern towards the south, where there is a pronounced low (black arrow on maps c, d and e) that appears to get partially filled up as marker L is reached (map f)

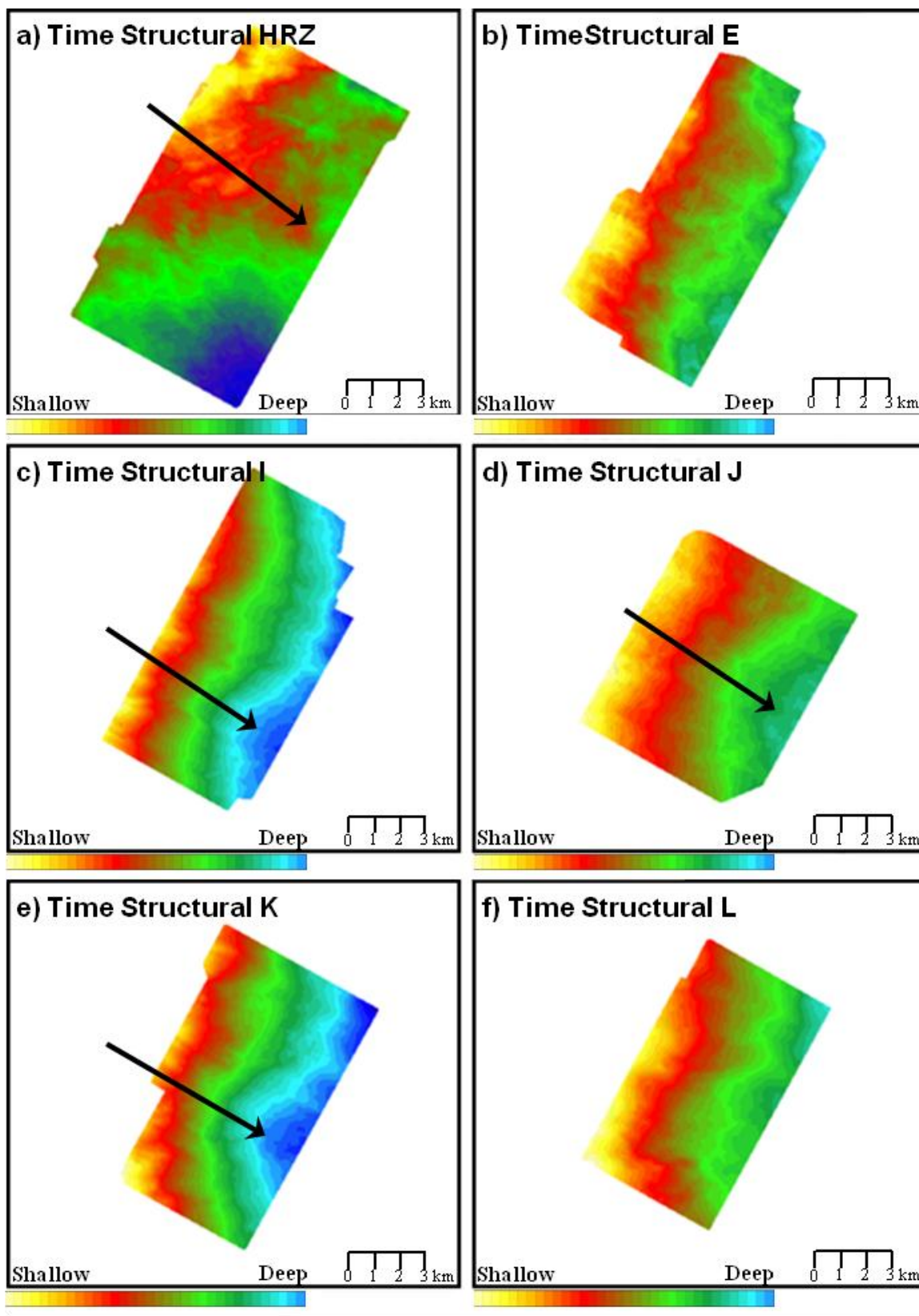


Figure 12. Composite of isochrons where the base of each map corresponds to the HRZ, the top or shallower markers are surfaces that get younger in age starting with marker G (a) all the way to marker L (f). Color bars used are the same for the six maps, with red to yellow displaying shallow values, and dark blue representing deeper contours. This set of maps clearly show the west-to-east depositional filling pattern reflected by contours with an approximate south-to-north trend and an east dip that indicates the filling pattern over the slope towards the basin as the seismic transect from Figure 4 also suggests. Isochrons for intervals H, I, J, K, and L suggest the presence of a low (black arrow in each map), easily recognized with the white trend line between the yellow and light blue colors. This low could potentially be a good location for sediment deposits that were carried by currents down the slope

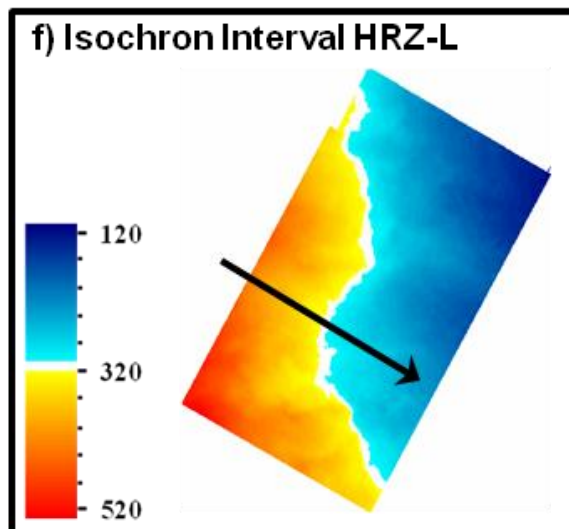
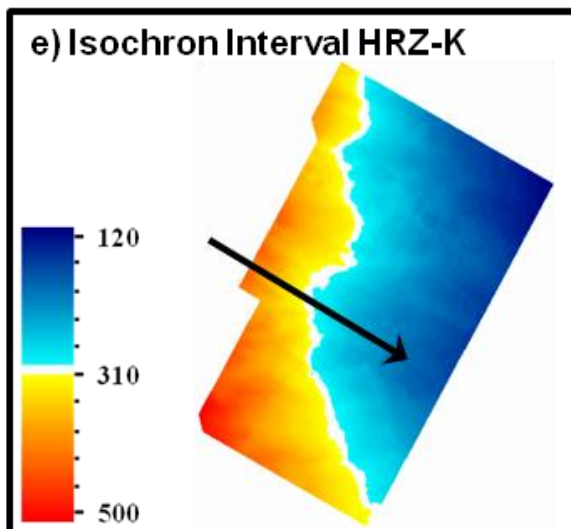
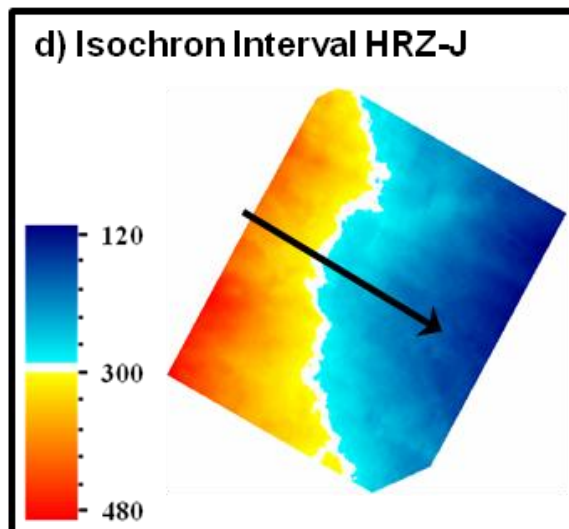
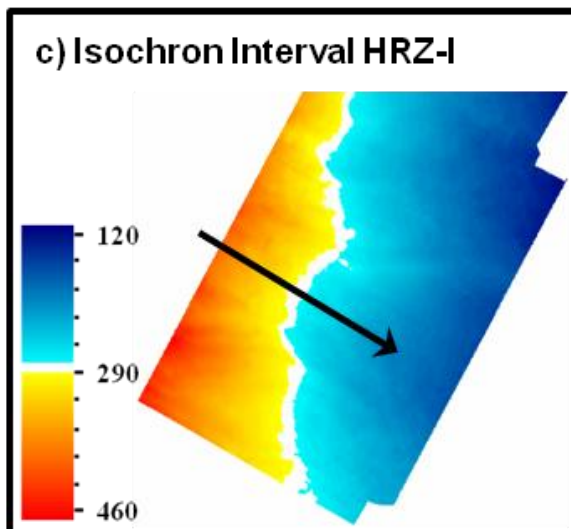
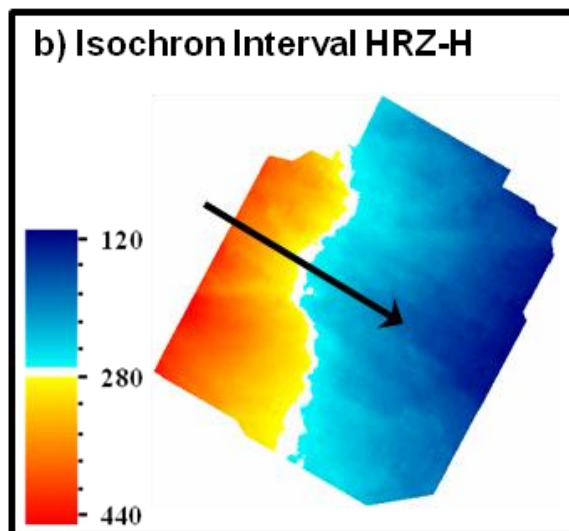
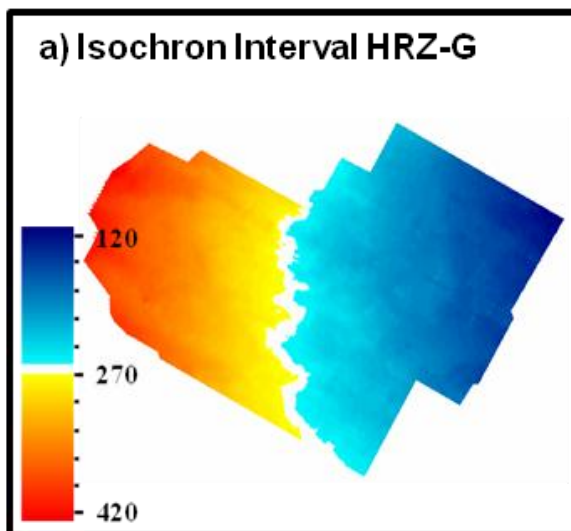


Figure 13. Composite isochrons for individual intervals with constant color bar, where hot colors (towards red) represent thicker intervals and cold colors (towards dark blue) thin intervals. These isochrons together suggest that the depocenter of the bodies (red-to-yellow) deposited on top of the slope migrated with a north-eastern-to-south-western trend, giving this way an idea of how the sediments got deposited by always looking for the lower part on the relief of the slope that corresponded to the previous lobes. This is the expected behavior as currents always look for the deeper or lower paths to go through and thus deposit part of their sediment loads on their paths. a) interval D-E with two dashed arrows that show the trends of the thickest parts of the isochron where it was assume that the biggest sediment load was deposited; b) interval E-Ea with one dashed arrow that follows the thickest part of this body which appear to be accommodated approximately between the two previous depocenters from D-E; c) interval Ea-F, again with two dashed arrows, one that migrated to the south, whereas the other (northern one) seems to have filled in the thinner part (blue) from interval E-Ea; d) interval F-G showing scattered bodies that are the response of probably thin sands or interbedded sands with shales below the seismic resolution; e) interval J-K with two dashed arrows to the south on top of what could be one or two depocenters; and f) interval K-L with two dashed arrow following two potential depocenters that partially filled what seemed to be thinner intervals from J-K.

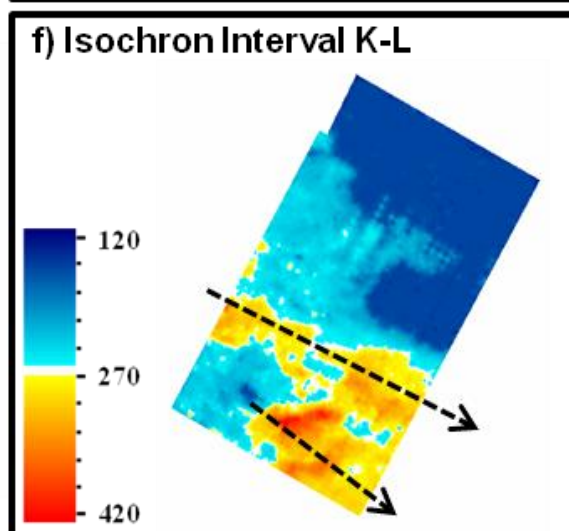
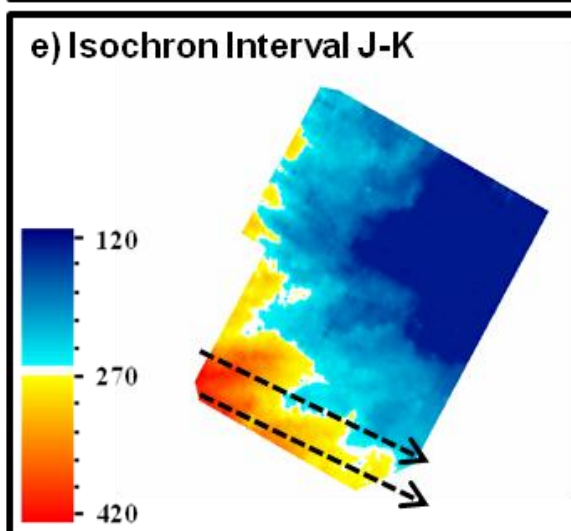
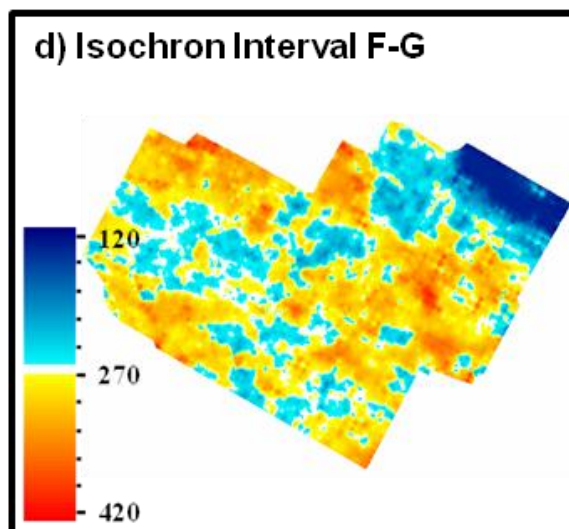
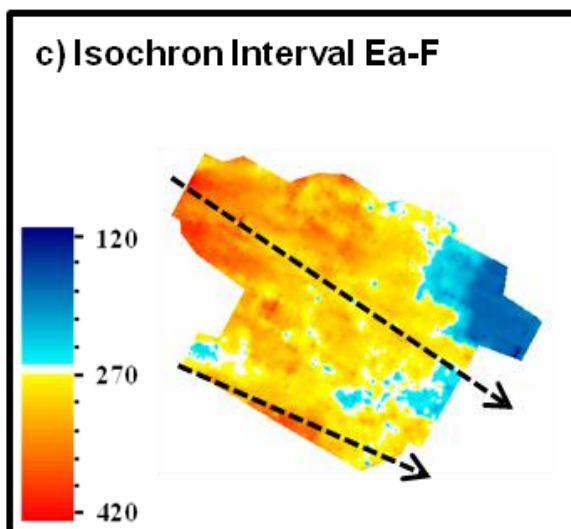
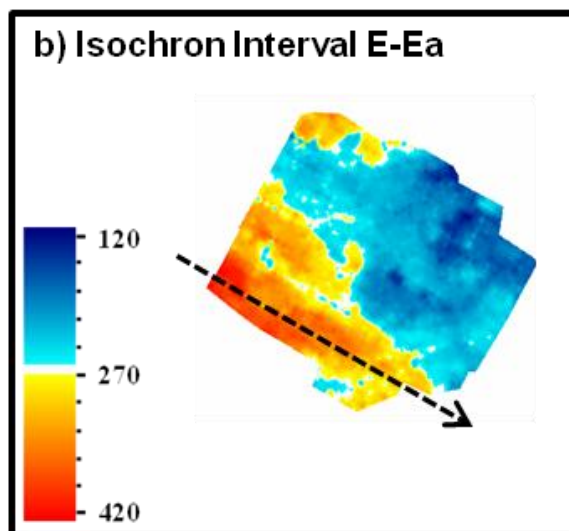
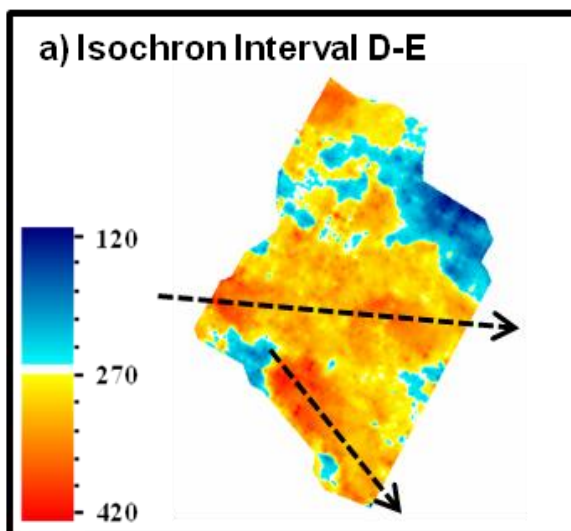


Figure 14. Wireline logs corresponding to Well A with seismic markers J (green), I (red) and HRZ (blue) displayed. Two cut-off values were applied; a first one of 120 to indicate sandstones (yellow) on the GR, and a second of 10 ohm.m on the resistivity logs (red vertical line) to indicate potential hydrocarbon presence or fresh water sandstones. Marker J corresponds to the top of a relatively thin sandstone package (low GR reading) which is characterized by a increase in P-wave (DT), a decrease on the S-wave (DT_SH), a decrease in density (RHOB), and an increase in resistivity, normally interpreted as a hydrocarbon indicator, since hydrocarbons, as the rock's matrix, are not-conductive, therefore, as the hydrocarbon saturation of the pores increases, the rock's resistivity also is expected to increase. Marker I represents potentially the base of a thin sandstone, but in this case this pick is characterized by basically no changes on P nor S-waves, a relatively small decrease on density but no increase on resistivity, suggesting no hydrocarbon saturation

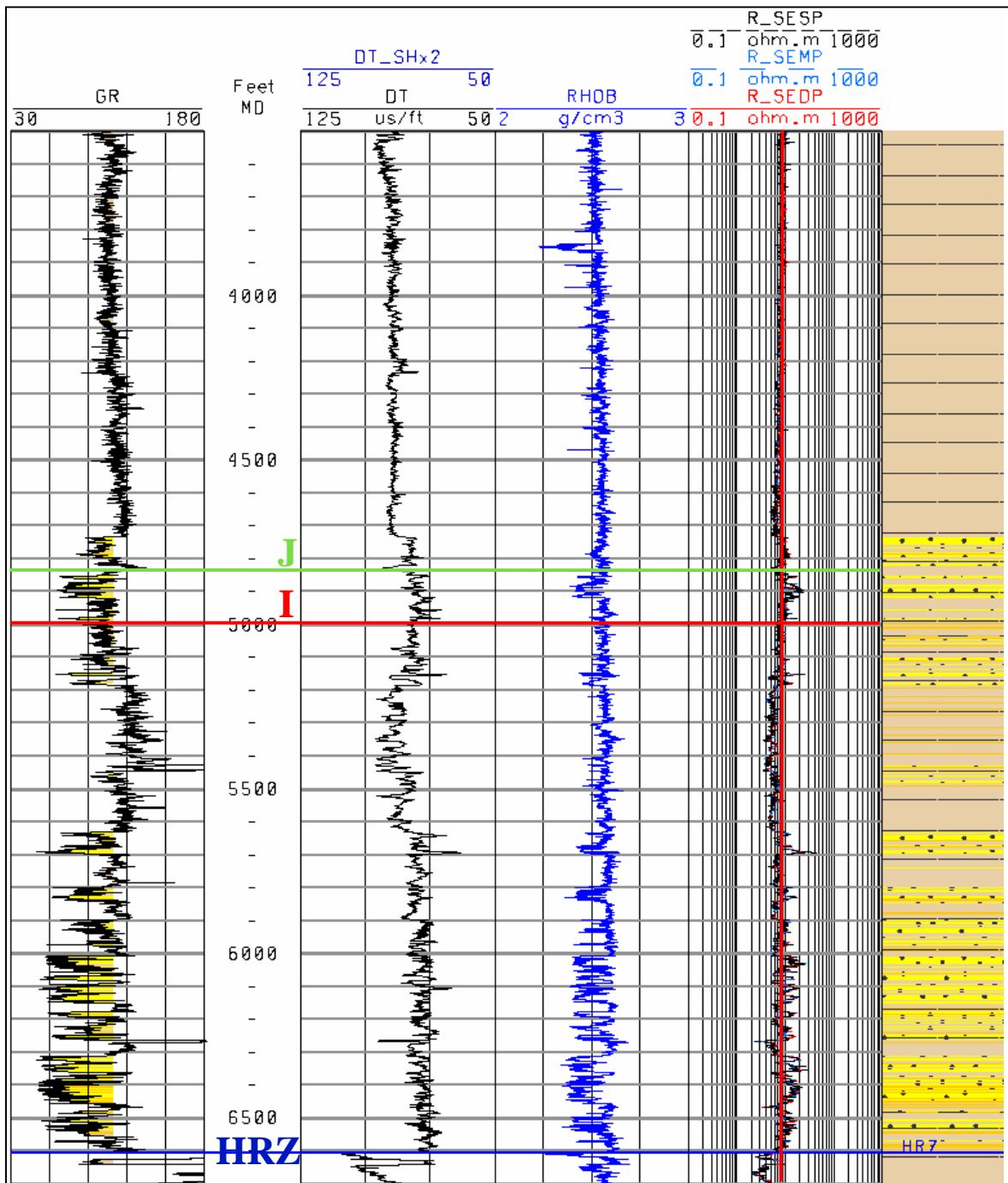


Figure 15. Composite image of seismic marker J (horizon J on Figure 8 close to AVO signature marker C); a) West-to-east section from the fully stack time-migrated seismic file is displayed with Well A overlain. Additionally, a GR (left), a synthetic seismogram (middle), and a sonic log (right) are displayed for further interpretation. The GR log defines marker J as the closest seismic marker to the top of a sandstone characterized by a decrease in the P-wave velocity; b) time structural map (upper middle) with hot colours (towards yellow) representing shallower values, and cold colours (towards blue) representing deeper values. Map is showing the orientation of the slope with a set of arrows pointing at lows that could be interpreted as feeders with some high slope channels developing down the slope towards the basin; c) corresponds to the maximum trough amplitude extracted from the fully stacked seismic file (AVO friendly). Color bar shows low amplitudes in black and high amplitudes in red. The high amplitude values define potential high slope channels that appear to form fans/lobes like features down the slope towards the basins (right); d) and e), correspond to the maximum trough amplitudes extracted from the near (NAS) and the far angle stacks (FAS), respectively, both with color bars that define low maximum trough values in black and high maximum trough values in red. Furthermore, the difference between FAS and NAS was calculated (f). This variation corresponds to the absolute increase in amplitude that was interpreted from the AVO signatures from the synthetic shot gathers (Figure 8), which we will call, for the purpose of the analysis, “sweet spots”. The color bar for this map (f) shows in light brown and dark blue, the lowest amplitude differences, which in this case can be interpreted to be the calculated attribute from bad manual picking or noise that was incorporated inside of the attribute analysis time window, therefore only the highest amplitude (lighter blue), are considered as potential sweet spots.

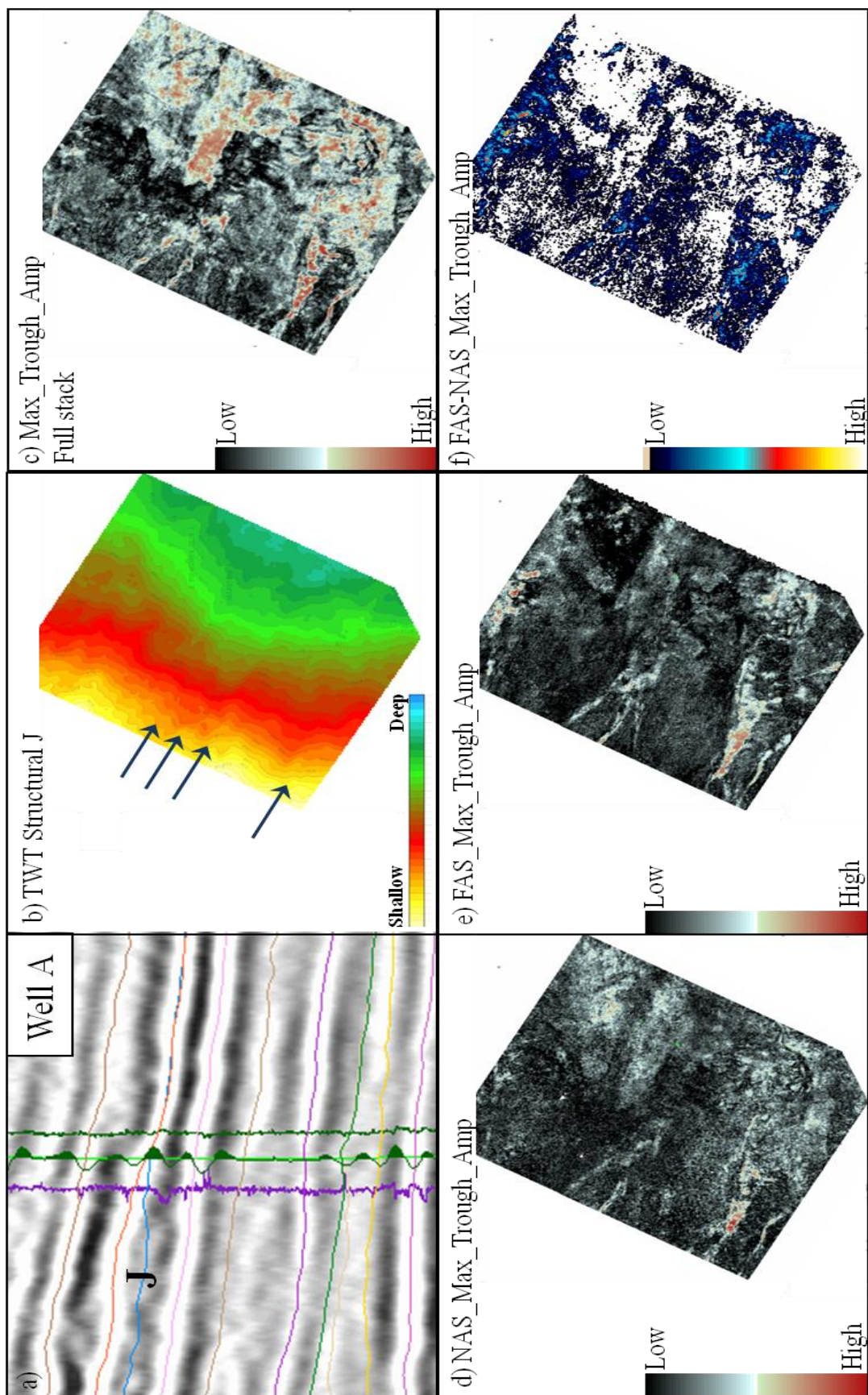


Figure 16. Composite image of seismic marker J (horizon J close to AVO signature marker C) showing two complex trace attribute analyses (see Appendix A for complex trace attribute analysis theory), average reflection strength (a, b and c maps), also known as envelope amplitude, and the total energy (d, e, and f maps). Both attributes were extracted from the NAS and FAS, and additionally, the difference between the FAS and the NAS was calculated (c and f) as for the maximum trough amplitude on Figure 14. The color bars for the NAS and FAS define low amplitudes as colours towards black and high amplitude as colours towards red. The NAS maps (a and d) roughly define what can be interpreted as a high slope channel system, with most of these channel like features suggesting a steep slope due to their almost straight trend. The FAS (b and e) sharpen the amplitudes that define some of these events. This was an expected response from the modeling results (Figure 8), maximum trough amplitude analysis (Figure 15), and also an anticipated response from the Alaskan sandstones with Class II to III AVO anomalies. Maps c) and f) show the calculated difference between the FAS and the NAS (potential sweet spots), and as indicated by the color bars, the light brown colours correspond to the lowest amplitude differences, which as for the maximum trough amplitude case, are considered the results of bad manual picking or noise that comes in from the time window used to extract these attributes, therefore only the highest differences (blue features following the high slope channel features trend) are considered sweet spots

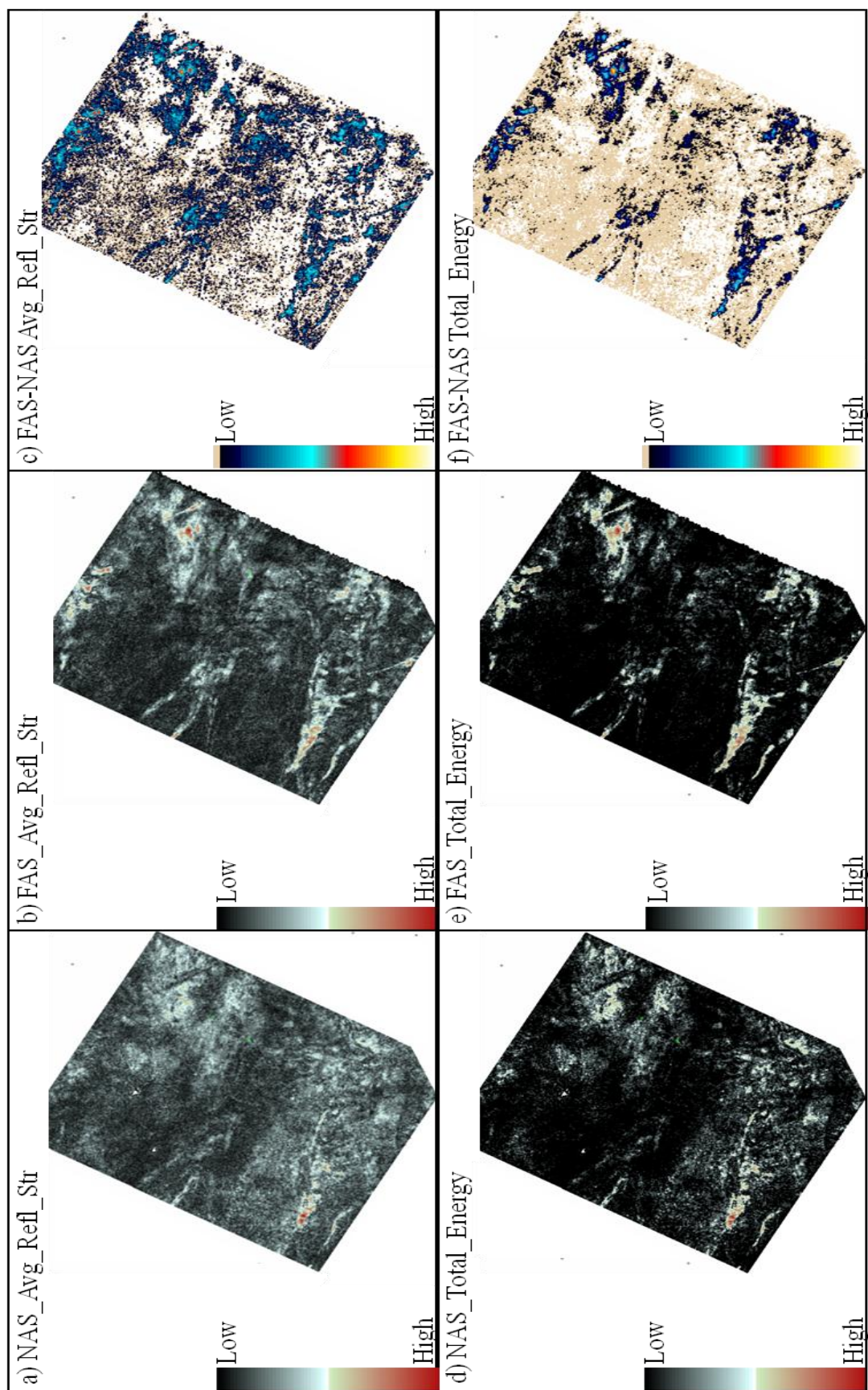


Figure 17. Composite of post-stack trace attributes with seismic files displayed on top of seismic marker J on a 3D visualization software. All trace attribute were calculated from the full stack time-migrated seismic file (AVO friendly) (Appendix A). a) Time structural map with red colours indicating shallower depths and blue colours deeper values; b) full stack time-migrated seismic file with troughs in yellow and peaks in darker blues. The highest negative amplitude values correspond to the same locations as the features interpreted as high slope channels from Figures 15 and 16; c) semblance cube with black colours corresponding to 0 correlation (indicating discontinuities) and brighter blue colours corresponding to total correlation (correlation equal to 1). Three distinctive trends can be identified; a first to the north-east, a second to the south of the first, and a third located to the south with a west-to-east trend. The two southernmost correspond to the same locations as two of the probable fan/lobes deposited by the feeder channel coming down the slope, whereas the northernmost was capture by the horizon based attributes from Figures 15 and 16 but it is not sharp enough to make a conclusion on what it could be; d) sweetness ($I_{amp}/(I_{freq})^{1/2}$), as the semblance results, this attribute shows the same three distinctive features (red and yellow colours), but with better boundaries delineated, most probably due to the scale of the attribute itself, which is not constrain from 0 to 1 as semblance is; e) gradient (generated from shot gathers), used in many cases as a lithology differentiator. In this case, two distinctive trends are differentiated, a first yellow-to-orange that follow the trends of the high slope channels and are suggested to be at least partially filled with sands by the GR log from Figure 14, and a second in blue that represents what was interpreted to be unconfined fans/lobes that could be filled in by either shales or interbedded sands with shales; and f) instantaneous phase, an attribute known to emphasize spatial continuity, shows in grey the continuity of the troughs (compare to map b), whereas in red parts of the peaks and not-continuous events.

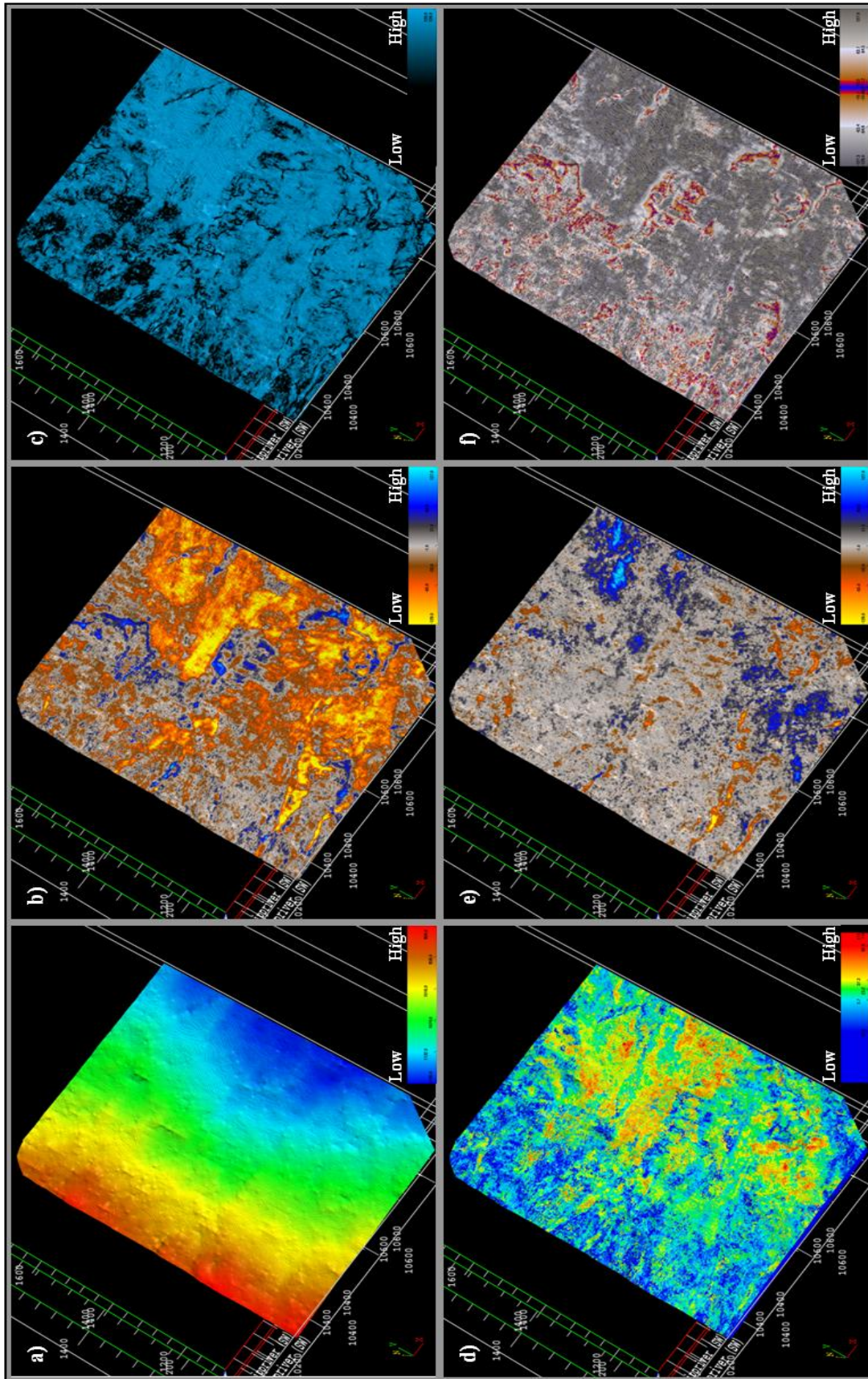


Figure 18. Composite image of a thin sandstone interval enclosed between seismic markers I and J. a) West-to-east seismic section of the full stack seismic file with Well A displayed. Three logs describe the interval starting from left to right with a GR (purple), a zero-offset synthetic seismogram and a DT (green). a) Isochron of interval I-J with blue colors showing the thickest parts, whereas grays described the thinnest parts of the interval. The isochron suggests that the sediment at that corresponding geological time was deposited preferentially in lows

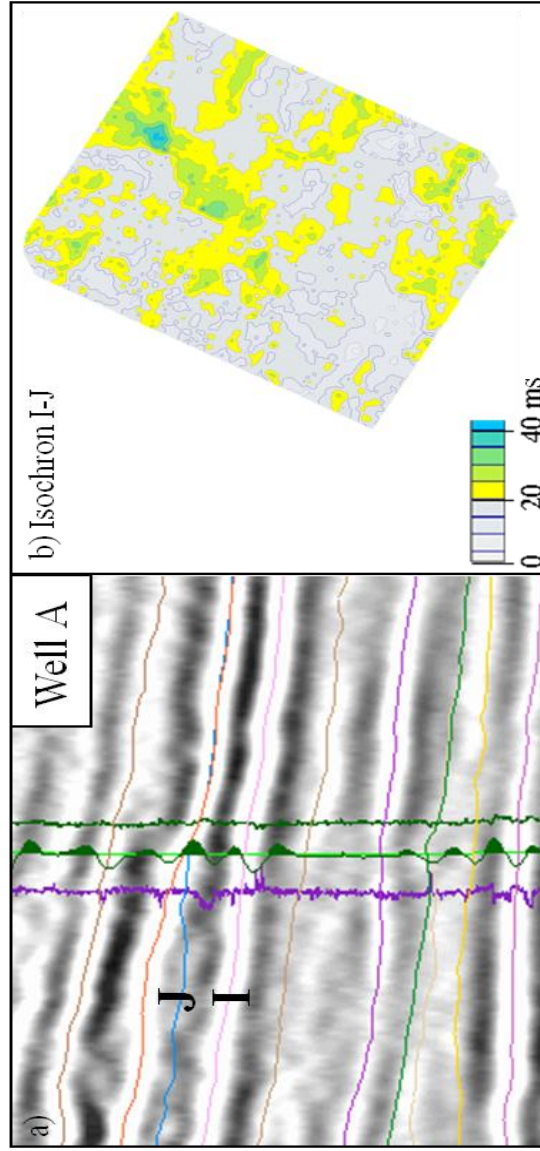


Figure 19. Composite image of marker I. a) Seismic section corresponding to a west-to-east line from the time-migrated seismic file with Well A displayed on top. Additionally, a GR (left), a synthetic seismogram (middle), and a sonic log (right) are displayed. The seismic character of this horizon is a strong trough that appears very close to the base of a thin sandstone (GR log). b) Time structural map showing multiple possible feeders (arrows) with high slope channels developing down the slope toward the beginning of the basin. c) Average reflection strength or amplitude envelope calculated from the full stack time-migrated seismic file. The lower three maps correspond to maximum trough amplitudes extracted from the near (d) and the far (e) angle stacks, plus the difference between them that defines potential sweet spots (f). The synthetic shot gathers generated by modeling (Figure 14) indicate that this marker is characterized by an amplitude response with increasing offset that corresponds to a false AVO signature.

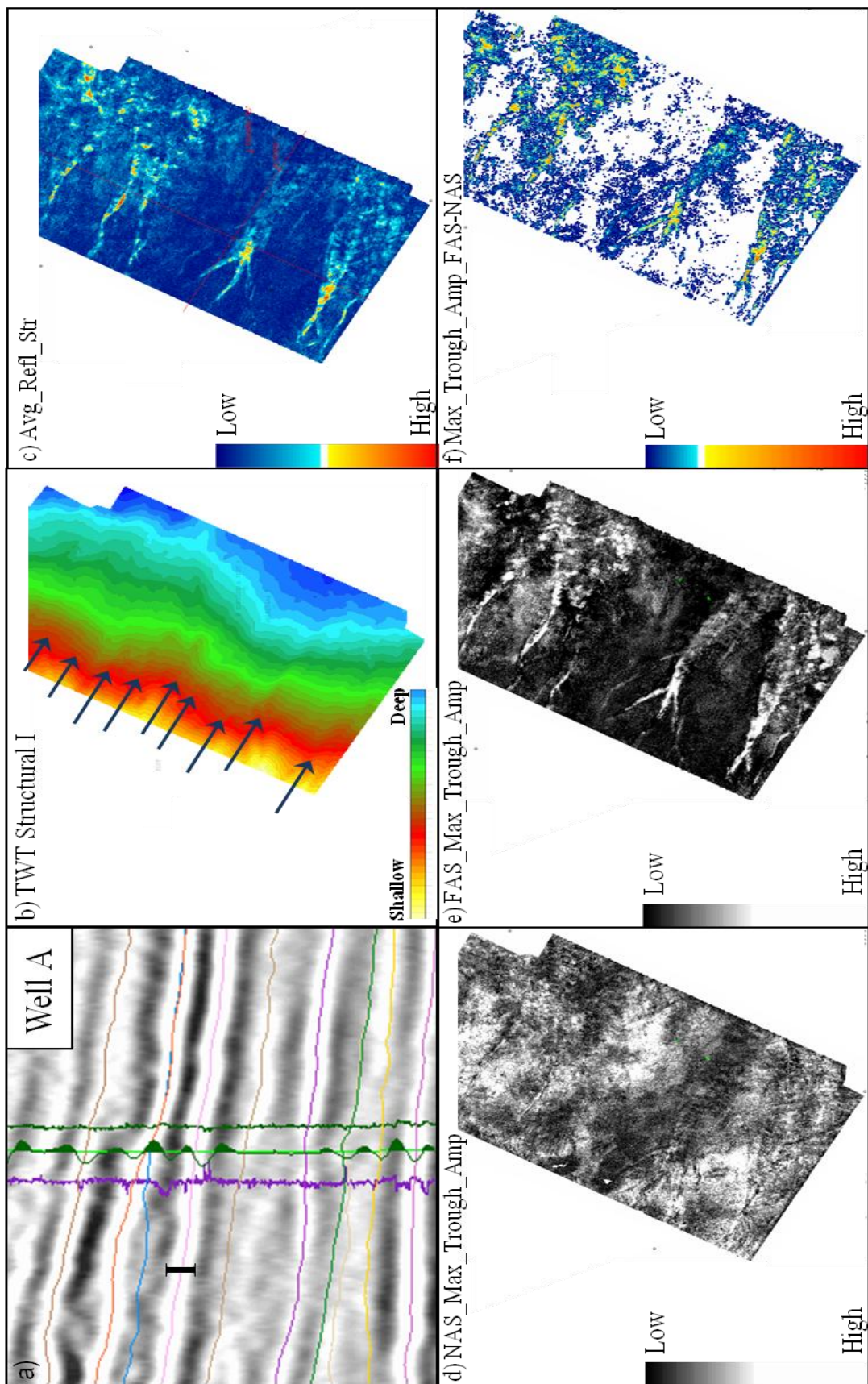


Figure 20. Composite of two similar amplitude statistic seismic attribute maps, RMS amplitude and total energy. The upper maps correspond to RMS calculated from near (a) and far (b) angle stacks, plus the difference between them (c), whereas the lower correspond to total energy calculated from the same angle stacks. The far minus the near angle stacks (offset) define the difference in amplitude with increasing offset, which according to the synthetic shot gathers correspond to amplitude responses that correspond to seismic background. Color bars for the total energy (d, e, and f) outputs where adjusted in order to sharpen the false AVO signatures described in the far angles.

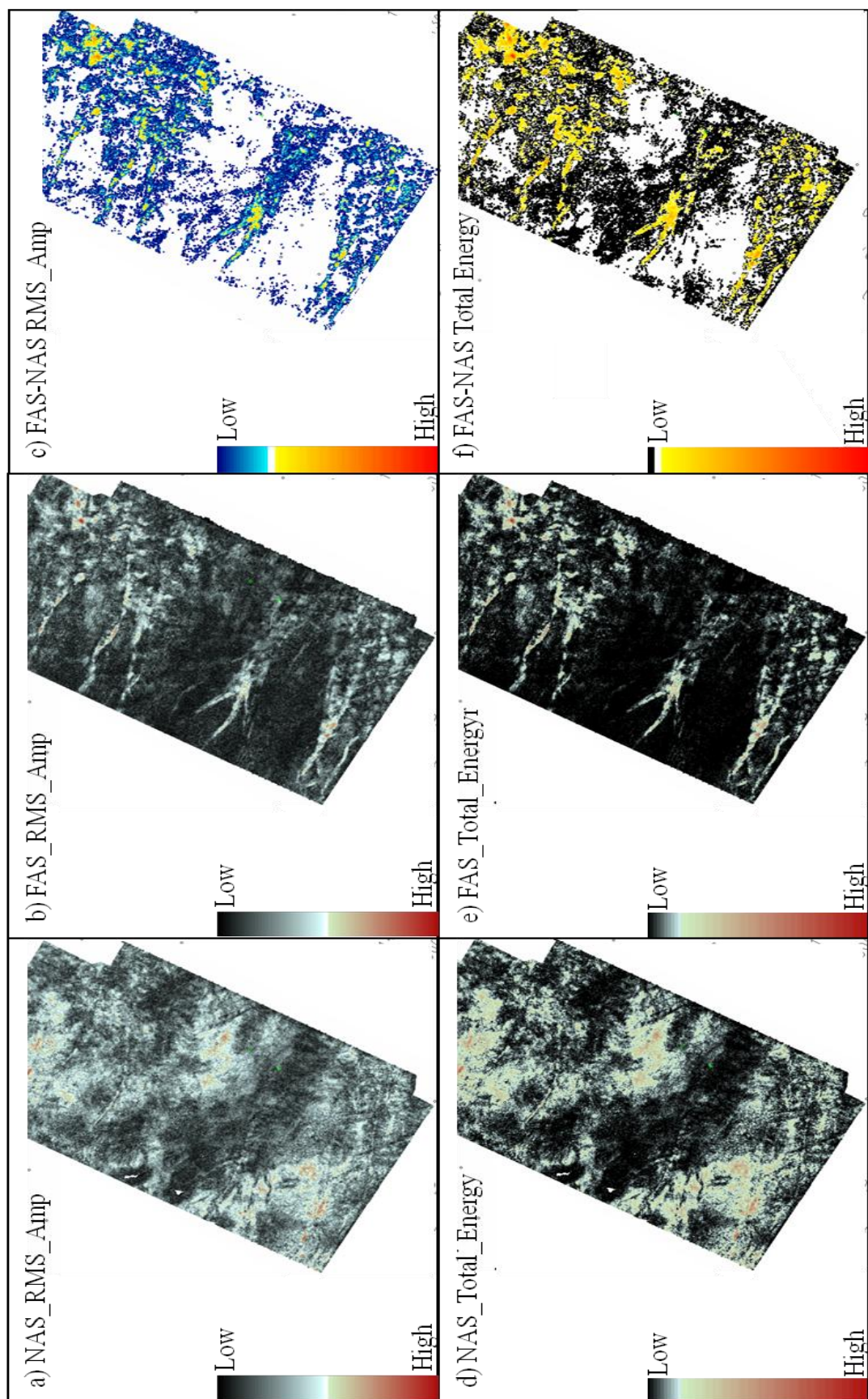


Figure 21. Summary of RMS amplitudes of randomly selected markers within the Torok Formation calculated from far angle stacks (FAS) to isolate the amplitude responses with increasing offset. By isolating these responses from the FAS, amplitude responses with increasing offset that define possible deep water geomorphologies can be better analyzed due to their increased sharpness. Some of these responses are what characterize AVO anomalies Class II and III, although before classifying them it is necessary to analyze the synthetic shot gathers acquired from the AVO modeling (Figure 8)

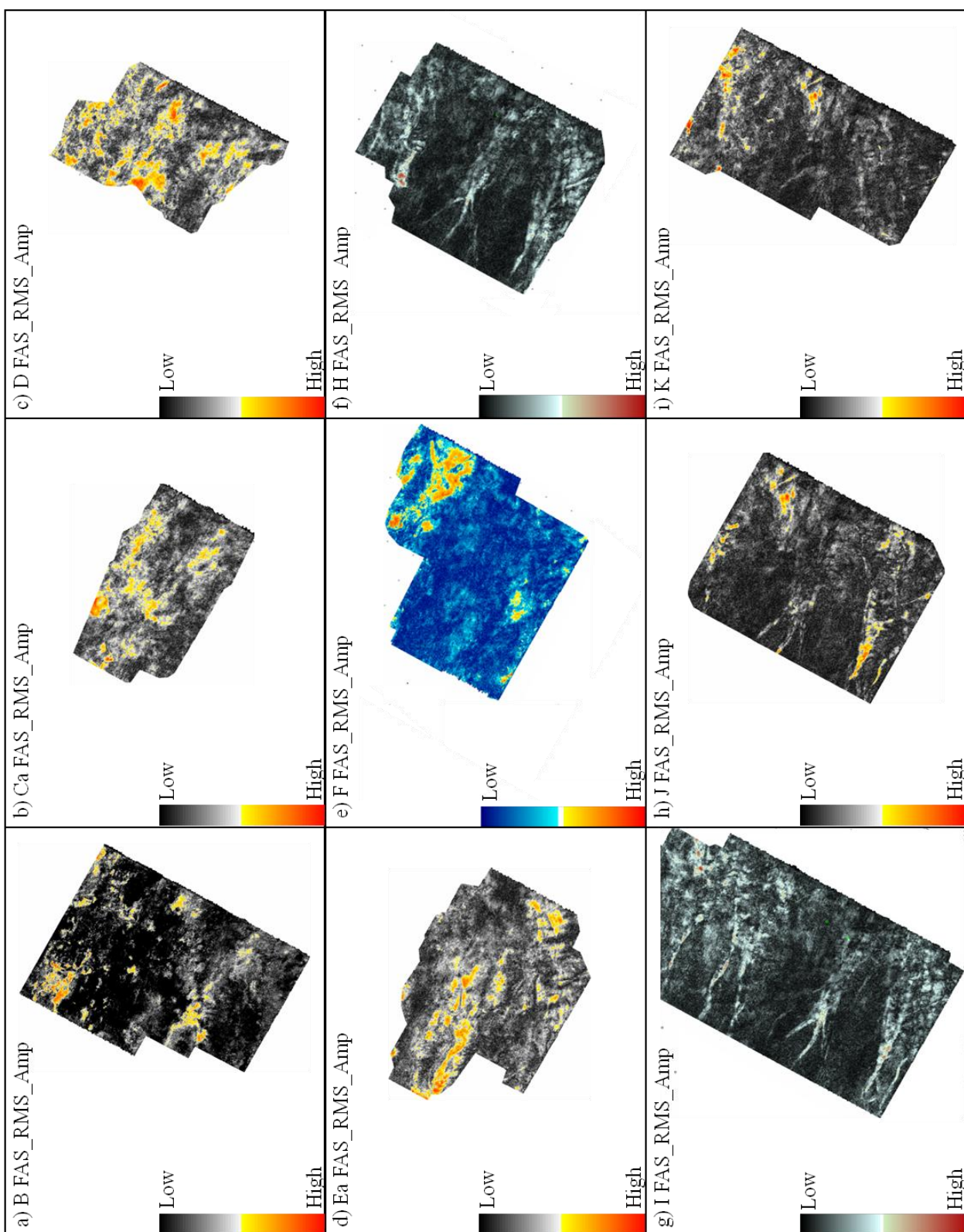
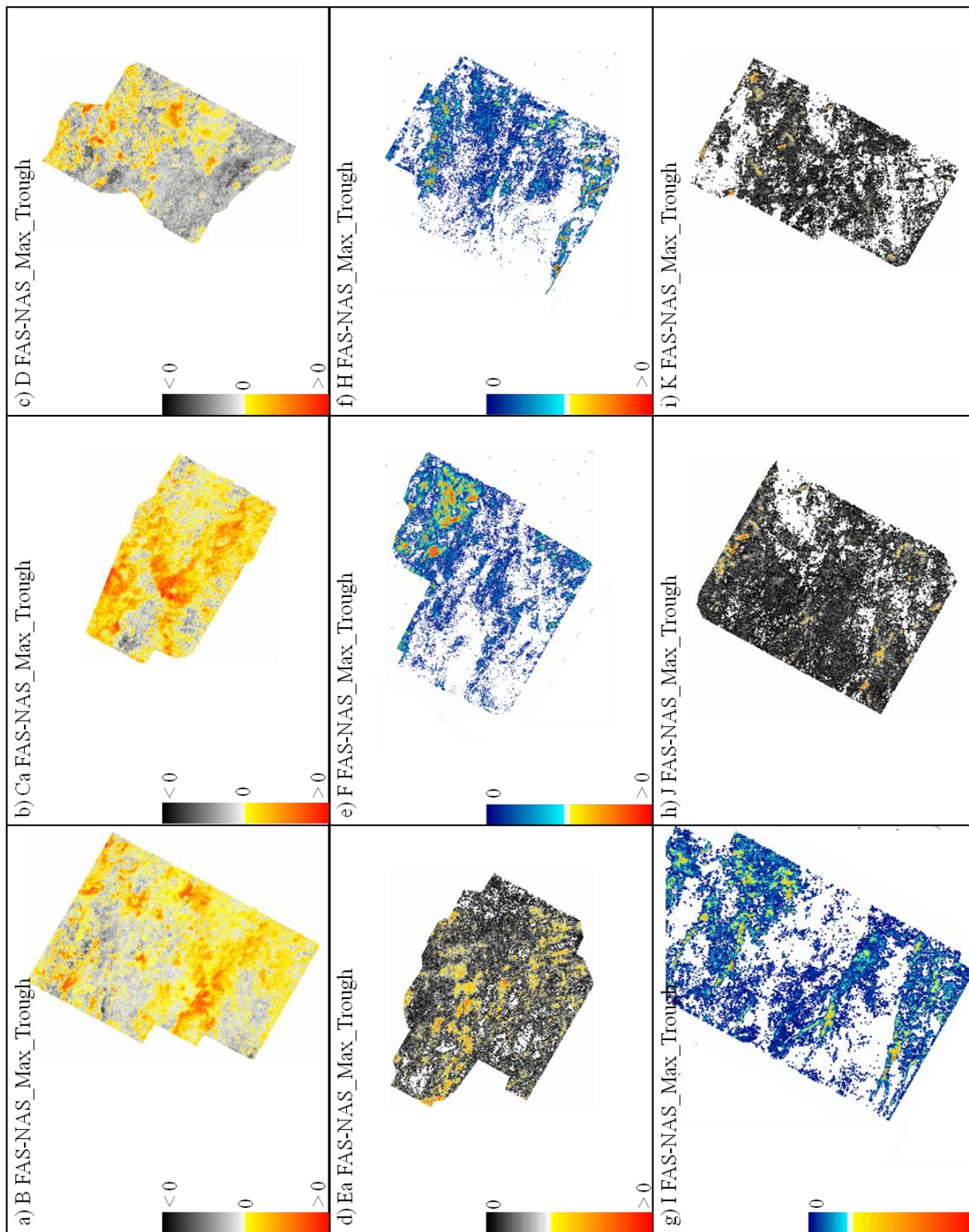


Figure 22. Summary of the differences between maximum trough amplitude calculated from the far and near angle stack seismic files from randomly selected markers within the Torok Formation. Normally, when in the presence of Class II or III AVO anomalies, the difference between attributes calculated from far and near angle stacks will define the sweet spots or bodies with anomalous amplitude, but as it can be seen from either Figure 14 or Table 2, there is always the possibility of obtaining an AVO response from the seismic background, which can be due to factors such as a shale with a decrease in P-wave and an increase in S-wave velocity, small porosity variations, wrong seismic processing sequence applied, and the presence of volcanic ash, among others



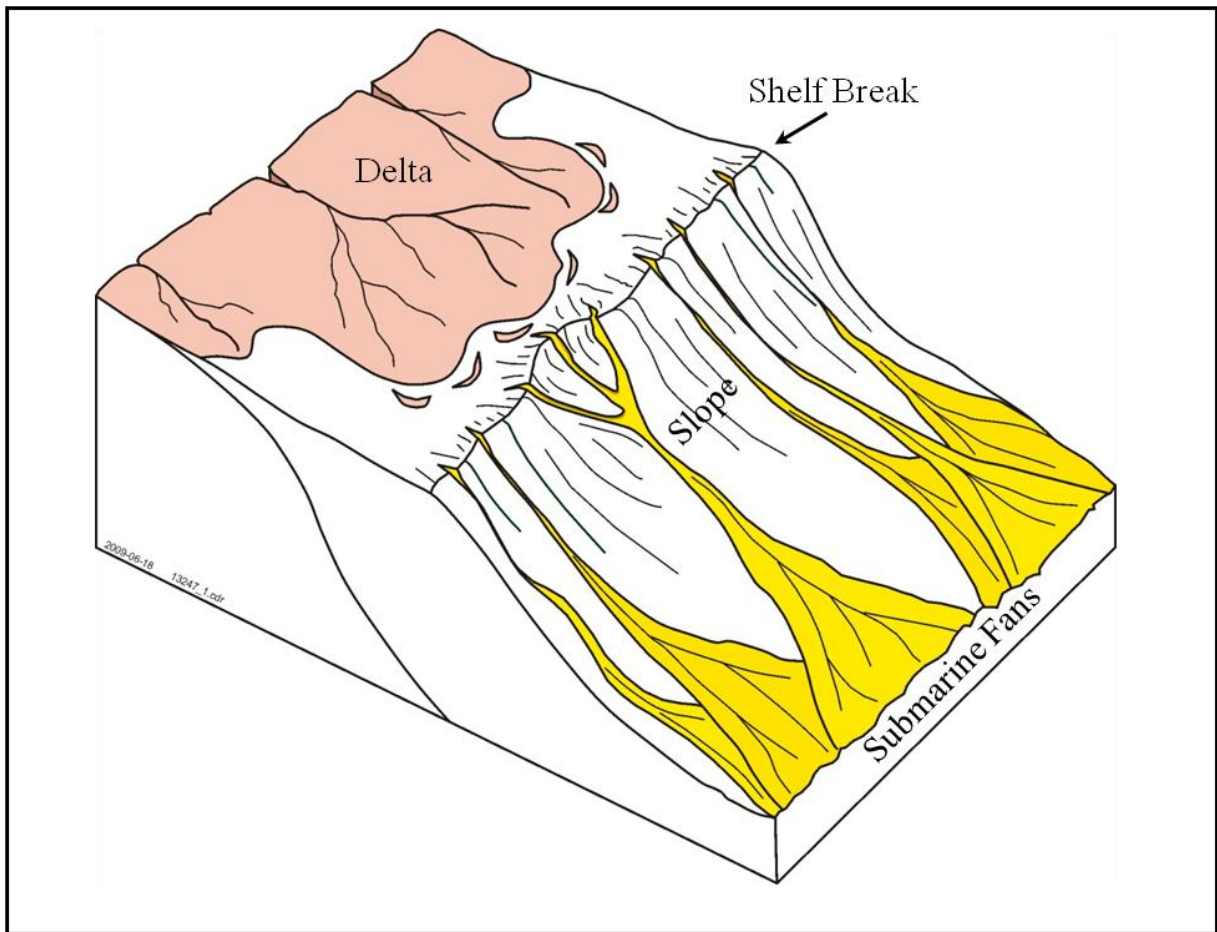


Figure 23. Schematic block diagram illustrating submarine fan deposition based on the slope channel system defined by integrating the time structural maps with the seismic attributes extracted mainly from the far angle stacks. The slope dip angle was interpreted to range between 3 to 5 degrees, based on the path defined by the feeder channels that cut through the slope and later form potential submarine fans, although, due to the surveys boundaries, the fan development cannot be validated. The composition (lithology) of the high slope channel system and submarine fans is unknown due to a lack of wells penetrating them

Well Name	DT	DT_SH	GR	RHOB
Well A	✓	✓	✓	✓
Well B	✓	✓	✓	✓
Well C	✓	✓	✓	✓
Well D	✓	X	✓	✓
Well E	✓	X	✓	✓
Well F	✓	X	✓	✓
Well G	✓	X	✓	✓

Table 1. Well data base showing the wireline log availability for each well used for both the seismic calibration (DT, GR, and RHOB) and the AVO modeling (DT, DT_SH, GR, and RHOB)

Table 2. Classification of the different amplitude responses to increasing offset based on the elastic modeling results obtained for the three different wells with S-wave sonics. The classification is done for individual markers and intervals in cases where sandstone bodies or interbedded sandstones with shales are present between two horizons. Amplitude responses are described based on the intercept (starting onset type) and gradient (slope). In some cases the AVO anomalies observed on both the synthetic shot gathers and the angle stack files correspond to false anomalies, which could be due to reflector dip and depth, receiver array attenuation, inelastic attenuation, thin bed effects, anisotropy and/or an erroneous seismic processing sequence

Horizon Name	Intercept	Gradient	AVO Class	Comments
L	+	-	II	Density log suggests a porosity increase
K	+	-	III	Peak becomes brighter in the far angle stack.
J	-	-	III	Top of interbedded sandstones with shales. Typical Class III AVO anomaly
I to J	+	-	III	A couple of sand boddies with shale in between and AVO responses
I	-	-	N/A	No sandstone nor decrease in Poisson's ratio. AVO response due to background
H to I	N/A	N/A	N/A	Thin sandstone with no porosity
H	-	-	III	Top of thin sandstone with small porosity increase
G	N/A	N/A	N/A	Thin sandstone body with no porosity nor amplitude anomaly
E to F/E_a	+	-	III	No sandstone boddies present
E	N/A	N/A	N/A	Thin sandstone with no decrease in DT (p-wave) nor amplitude anomaly
D to E	N/A	N/A	N/A	Thin sandstone body with no porosity nor amplitude anomaly
Ca to D	-	-	III	Very subtle amplitude anomaly present
B to Ca	N/A	N/A	N/A	Sandstone present with porosity (density) but no AVO effect
SubB to B	N/A	N/A	N/A	No amplitude anomalies in the synthetic shot gathers
Sub Ba to SubB	+	-	II	No increase in DT_SH (s-wave sonic)
AB to Sub Ba	+	-	II	Density log suggest a porosity increase (interbedded sandstones with shales)
AB	N/A	N/A	N/A	Sandstone present with porosity (density) but no AVO effect

CHAPTER 3: CONCLUSIONS

The primary objective of this thesis was to identify potential reservoir sands within the Torok Formation in a southern portion of a 3D survey located in the Northern Slope of Alaska by integrating complex trace attributes with AVO modeling. As a result, I successfully subdivided the lower portion of the Torok Formation into 24 different horizons, which made it possible to perform a detailed seismic attribute analysis of each seismic marker. By modeling synthetic shot gathers using a fully elastic wave equation, Class II and III AVO anomalies were identified; the first (Class II) were defined by a positive or very subtle negative intercept and a negative gradient, and the last (Class III) were described by a negative intercept and gradient.

By acquiring amplitude and complex trace attributes from the near and far angle stack seismic files, it was possible to map and capture the approximate extensions of some of these anomalies considered to be sweet spots. The integration with wireline logs resulted with seismic markers J, K and L, and intervals AB-to-Sub Ba, Sub Ba-to-SubB, Ca-to-D, and E-to-F/Ea as the most prospective due to a suggested increase in porosity (suggested by a decrease in density log values), a decrease in the P-wave velocity, an increase in the S-wave velocity, a decrease in Poisson's ratio (characteristic response of fluid filled reservoirs) and an increase in resistivity (characteristic hydrocarbon response). Some of the prospective markers delineated the geomorphology of a high slope channel system close to the shelf edge, which presumably transported sediments down the slope, and would end up accumulating them further down as fans/lobes filled up with either sands or interbedded sands with shales.

Some false AVO signatures were identified and mapped, which could have been caused by seismic signal interference due to events thicknesses below the seismic resolution, low signal-to-noise ratio (low fold), lithology lateral variations (anisotropy), and the type of migration algorithm applied to

the data, which was not strong enough to entirely correct and move the events to their real depth.

In addition to defining potential reservoir sand intervals within the Torok Fm, this study will also help in the further analysis and development of other prospective areas with similar geological settings within the North Slope of Alaska by being used as an analogous case study, and by helping to better understand reservoirs where AVO signatures are present.

REFERENCES

- Aki, R., Richards P.G., 1980, Quantitative seismology: Theory and methods: W.H. Freeman and Co., New York.
- Barnes, A.E., 1998, The complex seismic trace made simple, *The Leading Edge*, Society of Exploration Geophysicists, v. 17, No. 4, p. 473-476.
- Barnes, A.E., 2007, A tutorial on complex seismic trace analysis, *Geophysics*, Society of Exploration Geophysicists, v. 72, No. 6, p. W33-W43.
- Bird, K. J., and Molenaar, C. M., 1992, The North Slope foreland basin, Alaska, Foreland basins and fold belts, *The American Association of Petroleum Geologists*, Memoir 55, p. 363-393.
- Bird, K. J., 1994, The Ellesmerian petroleum system, North Slope of Alaska, The petroleum system - From source to trap, *The American Association of Petroleum Geologists*, Memoir 60, p. 339-358.
- Bird, K.J., 2001, Alaska: A Twenty-First –Century Petroleum Province, *The American Association of Petroleum Geologist*, Memoir 74, p137-165.
- Brown, A.R., 1996, Interpreter's Corner - Seismic attributes and their classification, *The Leading Edge*, Society of Exploration Geophysicists, 15, 10, 1090.
- Castagna, J.P., 1993, AVO Analysis – Tutorial and Review, *Offset-Dependent Reflectivity–Theory and Practice of AVO Analysis*, p. 3-36.
- Castagna, J.P., 1993, Petrophysical imaging using AVO, *The Leading Edge*, Society of Exploration Geophysicists, 12, p. 172- 178.
- Castagna, J.P., Batzle, M.L., and Kan, T.K., 1995, Rock Physics – The Link Between Rock Properties and AVO Response, in Castagna, J.P.,

- and Backus, M.M., Offset-dependent Reflectivity - Theory and practice of AVO Analysis, Society of Exploration Geophysicists, Tulsa, OK. p. 135-171.
- Castagna, J.P., and Swan, H.W., 1997, Principles of AVO crossplotting, The Leading Edge, Society of Exploration Geophysicists, 17, p. 337-342.
- Castagna, J.P., Swan, H.W., and Foster, D.J., 1998, Framework for AVO gradient and intercept interpretation, Geophysics, Society of Exploration Geophysicists, v. 63, No. 3, p. 948-956.
- Chopra, S., 2002, Coherence Cube and beyond, First Break, v. 20.1, p. 27-33.
- Chopra, S., and Marfurt. K. J., 2005, Seismic attributes – A historical perspective, Geophysics, Society of Exploration Geophysicists, v. 70, No. 5, p. 3-27.
- Chopra, S., and Marfurt, K.J., 2007, Seismic Attribute for Prospect Identification and Reservoir Characterization, ISBN, SEG Geophysical Developments Series No.11, Chapter 3, p. 45-72.
- Claerbout, J.F., 1976, Fundamentals of geophysical data processing, McGraw-Hill Book Co. Inc.
- Cole, F.K., Bird, K.J., Toro, J., Roure, F., O'Sullivan, P.B., Pawlewicz, M.J., and Howell, D.G., 1997, An integrated model for the tectonic developments of the frontal Brooks Range and Colville Basin 250 km west of the Trans-Alaska Crustal Transect, Journal of Geophysical Research, v. 102, No. B9, p. 20685-20708.
- Decker, P.L., 2007, Brookian Sequence Stratigraphic Correlations, Umiat Field to Milne Point Field, West-Central North Slope, Alaska, State of

Alaska – Department of Natural Resources, Division of Geological & Geophysical Surveys, p. 1-19.

Erickson, J. W., and Sneider R. M., 1997, Structural and hydrocarbon histories of the Ivishak (Sadlerochit) reservoir, Prudhoe Bay field: SPE Reservoir Engineering, v. 12, p 18-22.

Galloway, W.E., 1998, Siliciclastic Slope and Base-of-Slope Depositional System: Component Facies, Stratigraphic Architecture, and Classification, The American Association of Petroleum Geologist, v. 82, No. 4, p. 569-595.

Gingrich, D., Knock, D., and Masters R., 2001, Geophysical interpretation methods applied at Alpine Oil Field: North Slope, Alaska, The Leading Edge, Society of Exploration Geophysicists, v. 20, p. 730-738.

Graul, M., 2001, AVO: Yesterday, Today, and (a peek at) Tomorrow, Canadian Society of Exploration Geophysicists, Recorder, p. 35-38.

Hart, B., 2008, Channel detection in 3-D seismic data using sweetness, The American Association of Petroleum Geologist, v. 92, No. 6, p. 733-742.

Homza, T.X., 2004, A structural interpretation of the Fish Creek Slide (Lower Cretaceous), northern Alaska, The American Association of Petroleum Geologists, v. 88, No. 3, p. 265-278.

Houseknecht, D.W., and Schenk, C.J., 2001, Depositional Sequence and Facies in the Torok Formation, National Petroleum Reserve – Alaska (NPRA), U. S. Geological Survey, 956, p. 179-199.

Houseknecht, D.W., and Schenk, C.J., 2002, Depositional Sequences and Facies in the Torok Formation, National Petroleum Reserve – Alaska (NPRA), U.S. Geological Survey, Core Workshop, p. 5- 26.

- Hubbard, R.J., Edrich, S.P., and Rattey, P.R., 1987, Geologic evolution and hydrocarbon habitat of the 'Arctic Alaska Microplate', *Marine and Petroleum Geology*, v. 4, p. 2-34
- Jamison, H. C., Brockett, L. D., and McIntosh, R. A., 1980, Prudhoe Bay: a 10-year perspective, Giant oil and gas fields of the decade, *The American Association of Petroleum Geologists, Memoir 30*, p. 281-289.
- Jones, H. P., and Speers, R. G., 1976, Permo-Triassic reservoirs of Prudhoe Bay field, North Slope, Alaska, in J. Braunstein ed., *North America oil and gas fields, The American Association of Petroleum Geologist, Memoir 24*, p. 23-50.
- Kirschner, C.E., Grantz, A., and Mullen, M.W., 1992, Impact Origin of the Avak Structure, Arctic Alaska, and Genesis of the Barrow Gas Field, *The American Association of Petroleum Geologists*, v. 76, No. 5, p. 651-679.
- Kornbrath, R.W., Myers, M.D., Krouskop, D.L., Meyer, J.F., Houle, J.A., Ryherd, T.J., and Richter, K.N., 1997, Petroleum Potential of the Eastern National Petroleum Reserve-Alaska, *Alaska Division of Oil and Gas*, p. 1-30.
- Li, Y., Downton, J., and Xu, Y., 2007, Practical aspects of AVO modeling, *The Leading Edge, Society of Exploration Geophysicists*, v. 26, p. 295-310.
- Lillis, P. G., Lewan, M. D., Warden, A., Monk, S. M., and King, J. D, 1999, Identification and characterization of oil types and their source rocks, The oil and gas resource potential on the 1002 Area, Arctic National Wildlife Refuge, Alaska: U.S. Geological Survey Open-File Report 98-34, 2 CD-ROMs, p. OA1-OA56.

- Magoon, L. B., 1994, The geology of known oil and gas resources by petroleum system – Onshore Alaska, The geology of Alaska: Geological Society of America, The geology of North America, v. G-1, p. 905-936.
- Magoon, L. B, and Dow, W. G, eds, 1994, The petroleum system – From source to trap, The American Association of Petroleum Geologist, Memoir 60, p. 655.
- Magoon, L. B., Bird, K. J., Burruss, R. C., Hayba, D., Houseknecht, D. W., Keller, M. A., Lillis, P. G., and Rowan, E. L., 1999, Evaluation of hydrocarbon charge and timing using the petroleum system, in ANWR Assessment Team, ed., The oil and gas resource potential of the 1002 Area, Arctic National Wildlife Refuge, Alaska: U.S. Geological Survey Open-File Report 98-34, 2 CD-ROMs, p. PS1-PS66.
- Marfurt, K.J., Kirlin, R.L., Farmer, S.L., and Bahorich, M.S., 1998, 3-D seismic attributes using a semblance-based coherency algorithm, Geophysics, Society of Exploration Geophysicists, v. 63, p. 1150-1165.
- Masterson, W. D., Holba, A., and Dzou, L., 1997, Filling history of America's two largest oil fields: Prudhoe Bay and Kuparuk, North Slope, Alaska (abs.), The American Association of Petroleum Geologist, Annual Convention Abstracts and Program, v. 6, p A77.
- Masterson, W. D., He, Z., Corrigan, J., Dzou, L. I. P., and Holba, A. G., 2000, Petroleum migration and filling history models for the Prudhoe Bay, Kuparuk and West Sak fields, North Slope, Alaska (abs), The American Association of Petroleum Geologist, Annual Meeting, New Orleans, Abstract with Program, p. A93.

- May, J.A., Przywara, M.S., Clark, R., Mazza, T., and Perez, J.G., 2007, Amplitude anomalies in a sequence stratigraphic framework: Exploration successes and pitfalls in a subgorge play, Sacramento Basin, California, *The Leading Edge*, Society of Exploration Geophysicists, v. 26, p. 1516-1526.
- Mayall, M., Jones, E., and Casey, M., 2006, Turbidite channel reservoir – Key elements in facies prediction and effective development, Elsevier Science Ltd, *Marine and Petroleum Geology* 23, p. 821-841.
- Mayfield, C. F., Tailleux, I. L., and Ellersieck, I., 1988, Stratigraphy, structure, and palinspastic synthesis of the western Brooks Range, northwestern Alaska, *Geology and exploration of the National Petroleum Reserve in Alaska*, U.S. Geological Survey Professional Paper 1399, p. 143-186.
- McMillen, K.J., 1991, *Seismic Stratigraphy of Lower Cretaceous Foreland Basin Submarine Fans in the North Slope, Alaska*, Springer-Verlag New York, Chapter 15, p. 289-302.
- Molenaar, C. M., 1982, Umiat field, and oil accumulation in a thrust-faulted anticline, North Slope of Alaska, *Geologic studies of the Cordilleran thrust belt*: Rocky Mountain Association of Geologists, p. 537-548.
- Montgomery, S.L., 1998, National Petroleum Reserve-Alaska: A Review of Recent Exploration, the American Association of Petroleum Geologists, v. 82, p. 1281-1299.
- Moore, T. E., Wallace, W. K., Bird, K. J., Karl, S. M., Mull, C. G., and Dillon, J. T., 1992, Stratigraphy, structure, and geologic synthesis of northern Alaska, U.S. Geological Survey Open-File Report OF 92-330, p. 183.

- Morrow, H., 1985, Seismic Subsequence Foothills Foldbelt, National Petroleum Reserve in Alaska (NPRA), The American Association of Petroleum Geologist, v. 69, p. 577-587.
- Mull, C. G., 1982, The tectonic evolution and structural style of the Brooks Range, Alaska: an illustrated summary, Geological studies of the Cordilleran thrust belt, Rocky Mountain Association of Geologists, v. 1, p. 1-45.
- Mull, C.G., Houseknecht, D.W., and Bird, K.J., 2003, Revised Cretaceous and Tertiary Stratigraphic Nomenclature in the Colville Basin, Northern Alaska, U.S. Geological Survey, U.S. Geological Survey Professional Paper 1673, Version 1.0, p. 1-12.
- Ostrander, W.J., 1984, Plane-wave reflection coefficients for gas sands at non-normal angles of incidence, Geophysics, Society of Exploration Geophysicists, v. 49, No. 10, p. 1637-1648.
- Pyles, D.R., 2008, Multiscale stratigraphic analysis of a structurally confined submarine fan: Carboniferous Ross Sandstone, Ireland, The American Association of Petroleum Geologist, v. 92, No. 5, p. 557-587.
- Rebesco, M., Neagu, R. C., Cuppari, A., Muto, F., Accettella, D., Dominici, R., Cova, A., Romano, C., and Caburlotto., 2009, Morphobathymetric analysis and evidence of submarine mass movements in the western Gulf of Taranto, International Journal of Earth Sciences, v. 98, p. 791-805.
- Regueiro, J. S., 1993, AVO analysis in low-and high-porosity gas sand reservoirs. Offset-Dependent Reflectivity – Theory and Practice of AVO analysis, Society of Exploration Geophysicists Investigations in Geophysics No 8.

- Richards, M., Bowman, M., and Reading, H., 1997, Submarine fans systems I: characterization and stratigraphic prediction, Elsevier Science Ltd, Marine and Petroleum Geology 15, p. 689-717.
- Richards, M., and Bowman, M., 1998, Submarine fans and related depositional system II: variability in reservoir architecture and wireline log character, Elsevier Science Ltd, Marine and Petroleum Geology 15, p.821-839.
- Rutherford, S.R., and Williams, R.H., 1989, Amplitude-versus-offset variations in gas sands, Geophysics, Society of Exploration Geophysicists, v. 54, p. 680-688.
- Saller, A.H., Noah, J.T., Ruzuar, A.P., and Schneider, R., 2004, Linked lowstand delta to basin-floor fan deposition, offshore Indonesia: An analog for deep-water reservoir system, The American Association of Petroleum Geologist Bulletin, v. 88, No. 1, p. 21-46.
- Saller, A., Werner, K., Sugiaman, F., Cebastian, A., May, R., Glenn, D., and Barker, C., 2008, Characteristics of Pleistocene deep-water fan lobes and their application to an upper Miocene reservoir model, offshore East Kalimantan, Indonesia, The American Association of Petroleum Geologist, v. 92, No. 7, p. 919-949.
- Seifert, W. K., Moldowan, J. M, and, Jones, R. W., 1980, Application of biological marker chemistry to petroleum exploration: Proceeding of the 10th World Petroleum Congress, Bucharest, p. 425-440.
- Sprat, R.S., Goins, N.R., and Fitch, T.J., 1993, Pseudo Shear - The analysis of AVO, in Castagna, J.P., and Backus, M.M., Offset-dependent-Reflectivity-Theory and practice of AVO Analysis, Society of Exploration Geophysicists, p. 37-56.

- Swan, H.W., 2007, Automatic compensation of AVO background drift, *The Leading Edge*, Society of Exploration Geophysicists, v. 26, no 12, p. 1528- 1536.
- Taner, M.T., Sheriff, R.E., 1977, Application of amplitude, frequency and other attributes to stratigraphic and hydrocarbon determination, *Seismic Stratigraphy: Application to Hydrocarbon Exploration*, The American Association of Petroleum Geologist, Memoir 26, p. 301-327.
- Taner, M.T., Koehler F., and Sheriff, R.E., 1929, Complex seismic trace analysis, *Geophysics*, Society of Exploration Geophysicists, v. 44, p. 1041-1063.
- Taner, M.T., 2001, *Seismic Attributes*, Canadian Society of Exploration Geophysicists Recorder, p. 48-56.
- Varkman, D., 1998, *Signals, oscillations, and waves*, Artech House, Inc.
- Veeken, P., and Rauch-Davies, M., 2006, AVO attribute analysis and seismic reservoir characterization, *Technical Article*, *First Break*, v. 24, p. 41-52.
- Weimer, P., 1987, *Seismic Stratigraphy of Three Areas of Lower Slope Failure, Torok Formation, Northern Alaska*, Department of Geological Sciences, The University of Texas at Austin, p. 481- 496.
- Werner, M.R., 1987, West Sak and Ugnu Sands: Low-Gravity Oil zones of the Kuparuk river Area, Alaskan North Slope, *Pacific Section SEPM & Alaskan Geology*, p. 109-118.
- Wicks, J. L., Buckingham, M. L., and Dupree, J. H., 1991, Endicott field – U.S.A., North Slope Basin, Alaska, in N. H. Foster and E. A. Beaumont, compilers, *Structural traps V: AAPG Treatise of petroleum geology*, *Atlas of oil and gas fields*, P. 1-25.

APPENDIX A: THEORETICAL BACKGROUND

SEISMIC ATTRIBUTES

A seismic attribute is a quantitative measure of a geometric, kinematic, dynamic, or statistical seismic characteristic of interest. Attributes are not independent of each other, but simply different ways of presenting and studying a limited amount of basic information. This basic information can be time, amplitude, frequency, and/or attenuation, and these form the basis of their classification. As a broad generalization, time-derived attributes provide structural information, amplitude-derived attributes provide stratigraphic and reservoir information and frequency-derived attributes provide additional useful reservoir information (Brown, 1996).

Attributes can be computed from prestack or from poststack data, before or after time migration. The procedure is the same in all cases, but in most studies attributes are derived from the fully stacked migrated 3D data volume or from seismic data that has variations of basic measurements as a function of angle of incidence (and hence source-to-receiver offset) which provides a further source of information. The main examples of pre-stack attributes are those related to amplitude variations with offset (Brown, 1996).

Seismic attributes were introduced in the mid 1960's and since then they have gained considerable popularity (Chopra et al. 2005). Today, the analysis of seismic attributes is an integral means of the reflection seismic interpretation process, and they have become a valid analytical tool for lithology prediction and reservoir characterization (Taner, 2001). The evolution of seismic attributes has been closely linked to advances in computer technology, meaning that they have grown in number and variety over the last four decades at a very fast pace.

Many authors (e.g. Sheriff, 1984; Taner 1994; Liner 2004) have attempted to classify attributes into families. The classification adapted by Liner

includes amplitude, time, dip and azimuth attributes, complex amplitude and frequency, generalized Hilbert attributes (also known as complex trace attributes), illumination, edge detection/coherency/semblance, Amplitude Variation with Offset (AVO), and spectral decomposition. Attributes are based on either the physical or morphological character of the data tied to lithology or geology and are therefore generally applicable from basin to basin around the world. In contrast, some attributes have a less well-defined basis in physics or geology. Although a given attribute may correlate well to a geologic feature or to reservoir productivity in one dataset it does not mean that these correlations will be valid in a different dataset (Liner, 2004).

In this thesis, only a subset of available attributes (amplitude and complex trace attributes, AVO, coherency/semblance, and sweetness) was used to study the seismic responses of potentially hydrocarbon charged sandstone reservoirs within the Torok Formation. These attributes will now be explained in detail.

1.) Amplitude Attributes. Lateral changes in amplitude have been used in stratigraphic studies to separate areas of concordant stratigraphy from chaotic beds in an interval. In general, isolated sands in shales can give strong amplitudes, whereas shale rich environments often have low seismic amplitudes (Hart, 2008). This is a general assumption, not a rule, since there are cases where entirely stacked turbidite sands have almost no internal reflection (e.g. the North Sea). These changes in the sand-shale ratio are in some cases possible to identify by viewing amplitude attributes in map views. The amplitudes attributes extracted during this study were:

1.1) Root Mean Square (RMS) Amplitude. RMS amplitude is calculated as the square root of the average of the squares of the amplitude values found within the analysis window (Figure A-1).

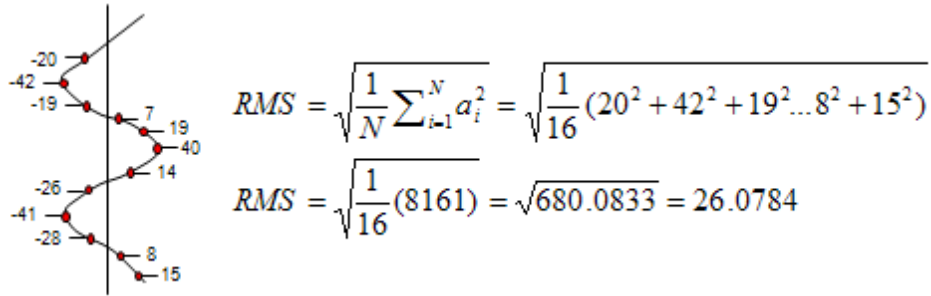
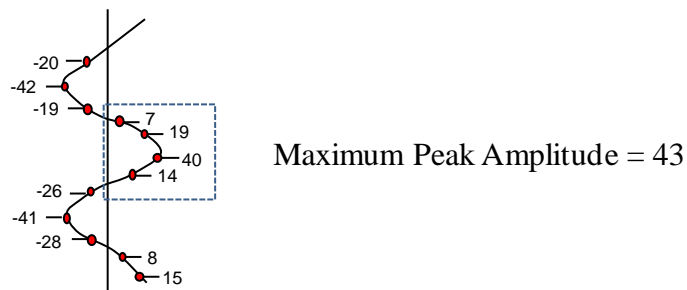


Figure A-1. Seismic trace (left) used to extract amplitude values for RMS calculation as shown on the equation on the right.

1.2) Maximum Peak Amplitude. For each trace, a parabolic fit is done through the highest positive amplitude value and the two samples on each side of it. Then the maximum value along that curve is interpolated and output as part of the attribute horizon output file (Figure A-2).



1.3) Average Peak Amplitude. All the positive values within the analysis window are added, then, this total is divided by the number of positive samples within the same window (Figure A-3).

Figure A-2. Seismic Trace (left) used to calculate the maximum amplitude on the interpolated peak. In most cases the maximum peak amplitude will not be the same as the highest sampled positive amplitude.

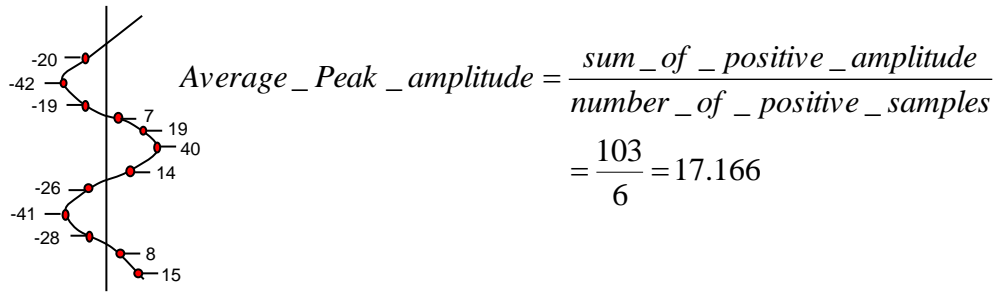


Figure A-3. Seismic trace (left) used to extract the amplitude values to calculate the average peak amplitude as shown on the equation on the right.

1.1) Total Energy. A very similar response as for the RMS Amplitude is achieved by squaring and adding all the amplitude values within the window of interest (Figure A-4).

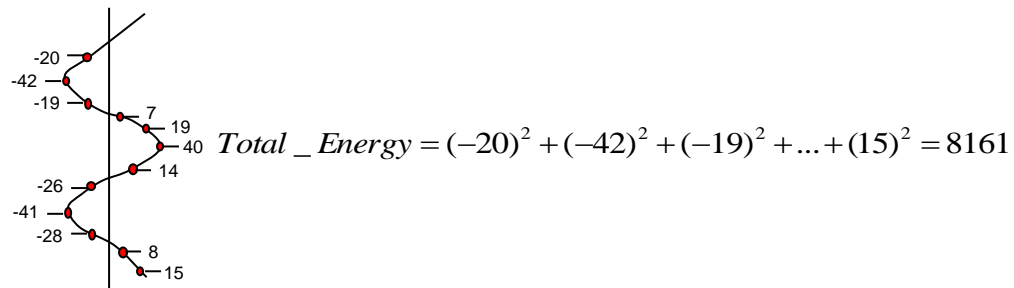


Figure A-4. Seismic trace (left) used to extract amplitude values used to calculate total energy as shown on the equation to the right of the seismic trace.

2.) Complex Seismic Trace Attributes. Complex seismic trace attribute analysis is the most popular method for computing poststack seismic attributes. Their invention was spurred by the discovery of bright spots (local increase of amplitude on a seismic section) in the late 1960s and early 1970s, which was an important event that demanded a new way of

thinking about seismic data and later helped proof that the apparent brightness of a seismic reflection on a true-amplitude display depends on several factors besides geology. In particular, differences in reflection polarity and phase, which tend to obscure the significance of bright spots (Barnes, 2007).

In the early 1970s Anstey came up with a good approach to measure the reflection strength with the trace envelope. This pioneering work was influential and laid the foundation of modern seismic attribute analysis (Taner, 2001; Chopra and Marfurt, 2005).

The trace envelope used by Anstey lacks a consistent definition, but it can be described as a slowly carrying function that connects the waveform peaks. To be independent of polarity, the envelope, reversed in sign, must connect the waveform troughs, and because it should also be independent of phase, it's required that it remains unchanged but still connect the peaks even as the seismic trace is rotated in phase by a constant angle (Barnes, 2007). This effectively defines the envelope of a seismic trace at a given time to be the maximum value that the trace can attain through a constant phase rotation. The mathematical form of this trace envelope is defined on Equation A-1.

$$a(t) = \sqrt{x^2(t) + y^2(t)} \quad (\text{A-1})$$

Where $x(t)$ is the seismic trace and $y(t)$ is the seismic trace rotated -90° , which is called the quadrature trace or Hilbert transformed trace (Appendices B and C).

An expression for the phase rotation angle $\theta(t)$ falls out as a byproduct of the mathematics as defined by Equation A-2.

$$\theta(t) = \arctan \left[\frac{y(t)}{x(t)} \right] \quad (\text{A-2})$$

The phase rotation angle is the angle required to rotate the trace to the maximum. The phase angle and envelope together form the foundation of the complex seismic trace analysis, which has proven to be a versatile method for quantifying seismic properties as attributes (Barnes, 2007).

With this said, we will call the trace envelope the instantaneous amplitude and the rotation angle the instantaneous phase. Instantaneous amplitude and phase are the fundamental complex trace attributes from which all others are derived. They are related to the seismic and quadrature traces through a Cartesian-to-polar coordinate conversion (Figure A-5). Turning this around, the seismic and quadrature traces are expressed in terms of the envelope and phase as described on Equations A-3 and A-4 respectively (Barnes, 2007).

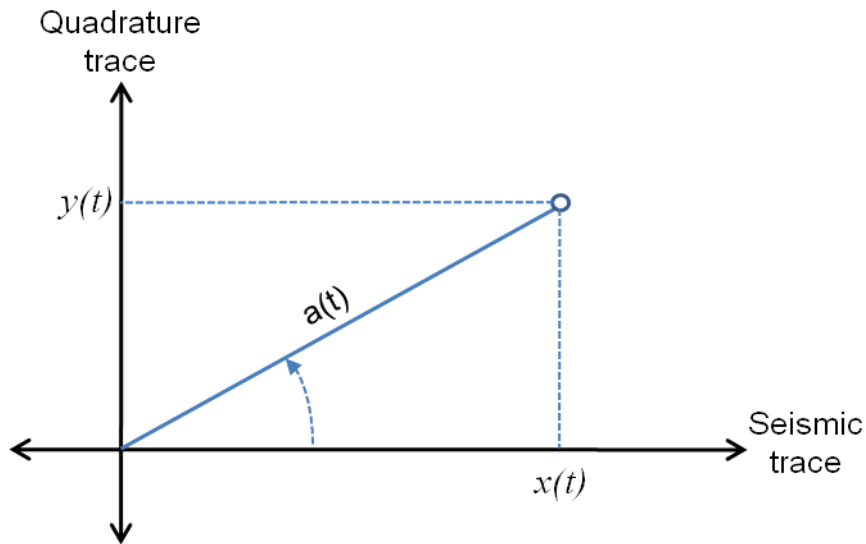


Figure A-5. The instantaneous amplitude $a(t)$ and instantaneous phase $\theta(t)$ derive from the seismic trace $x(t)$ and the quadrature trace $y(t)$ through a polar coordinate conversion.

$$x(t) = a(t)\cos\theta(t) \quad (\text{A-3})$$

$$y(t) = a(t)\sin\theta(t) \quad (\text{A-4})$$

Thus, a seismic trace can be represented as the product of two independent and separable functions, instantaneous amplitude and cosine of the instantaneous phase. This is the essence of complex seismic trace analysis – separating the amplitude information from the phase information in the seismic data (Barnes, 2007).

In summary, three main complex attributes can be derived, and these are described below:

2.1) Reflection Strength (instantaneous envelope or amplitude envelope). This attribute is calculated as the square root of the total energy of the seismic signal at an instant (equation A-1) and it is defined as the total energy of the seismic trace (Taner et al. 1977).

Reflection strength can be thought as amplitude independent of phase with its values always being greater than or equal to zero (Taner et al. 1977). This attribute is very sensitive to changes in acoustic impedance and thus to lithology, porosity, hydrocarbon content from layer to layer. For example, lateral changes in its values will often be associated with major lithological changes or with hydrocarbon accumulations, and gas reservoirs in unconsolidated sands will normally appear as high amplitude (bright spot) reflections (Taner et al. 1977).

Reflection strength is used in many cases to distinguish massive reflector from thin-bed composites. In the case of unconformities, the attribute will vary as subcropping bed changes (Taner et al. 1977).

2.1.1) Slope of the reflection strength, a derived attribute from the reflection strength that uses its output values, then by a least-squares regression curve it fits the reflection strength values within the window of interest, with the slope of this curve being the output of the attribute horizon file. If the values remain fairly constant, the slope is considered to be close to zero, if the values increase toward the bottom of the interval, the slope will be

positive, and in the opposite case the slope will be negative (Partyka et al. 1998).

This attribute is useful for mapping dominant vertical stratigraphic trends, and in some cases can be a strong tool for defining the lateral locations of gas and oil zones (Chopra and Marfurt, 2005).

2.2) Instantaneous Phase. This attribute emphasizes spatial continuity/discontinuity of reflections by providing a way for weak and strong events to appear with equal strength (Taner et al. 1977). View $\theta(t)$ on Equation A-3 for a mathematical understanding of this attribute.

Instantaneous phase makes strong events clearer and is effective in highlighting discontinuities, faults, pinch outs, angularities, and bed interfaces. Seismic sequence boundaries, sedimentary layer patterns and regions of onlap/offlap patterns often exhibit extra clarity (Partyka et al. 1998). It is a physical attribute normally used as a discriminator for geometrical shape classification and in phase velocity computation (Taner et al. 2001).

2.3) Instantaneous Frequency. This attribute is defined as the rate of change of the instantaneous phase. It is a measure of time dependent mean frequency and is independent of phase and amplitude (Partyka et al. 1998). This attribute responds to both wave propagation effects and depositional characteristics. Hence it is a physical attribute and can be used as an effective discriminator (Taner et al. 2001) in some cases such as:

- Fracture zone indicator, since fractures may appear as lower frequency zones.
- Bed thickness indicator. Higher frequencies indicate sharp interfaces while lower frequencies are indicative of more massive bedding geometries.

Other important pieces of information that can also be extracted from this attribute are the locations where instantaneous frequencies jump or exhibit a negative sign. These sign reversals are caused by closely-arriving reflected wavelets. This means, that the time derivative of the phase function will contain the indicator for thin beds in the form of large variations of instantaneous frequency (Taner et al. 2001)

Furthermore, destructive interference caused by seismic processing artifacts such as incorrect Normal Move Out (NMO) or statics corrections (prior to stacking) can artificially reduce the frequency content affecting the frequency distribution and consequently this attribute interpretation (Partyka et al. 1998).

3.) Amplitude variation with offset (AVO). In conventional utilization of the seismic reflection method, we assumed that the seismic signals can be viewed as a band-limited normal incidence reflection coefficient series with appropriate traveltimes and amplitude variation due to propagation through an overburden. Ostrander (1984) demonstrated that the reflection coefficients in gas-saturated sandstones vary in an anomalous way with increasing offset and showed how to use this behavior as a direct hydrocarbon indicator. His work constitutes part of the basis of what today is known as amplitude variation with offset (AVO) analysis (Castagna et al. 1995; Shuey, 1985; Aki and Richards, 1980).

The variation of reflection and transmission coefficients with incident angle and thus offset is commonly known as offset-dependent reflectivity. The Zoeppritz equations (Appendix D) describe how seismic waves are transmitted and reflected at media boundaries by relating amplitudes of P-waves and S-waves at each side of the interface. In the general case for an interface between two solids when the incident angle is not zero, four waves are generated: reflected P-wave and S-wave and transmitted P-wave and S-wave. The partition of energy among these is found from four boundary conditions which require continuity of normal and tangential

displacement and stress (Zoeppritz equations). Using Snell's Law a relationship for these variables that define all the angles can be established (equation A-5).

$$\frac{\sin \theta_{p1}}{V_{p1}} = \frac{\sin \theta_{s1}}{V_{s1}} = \frac{\sin \theta_{p2}}{V_{p2}} = \frac{\sin \theta_{s2}}{V_{s2}} \quad (\text{A-5})$$

For an incident plane P-wave of unity amplitude, the continuity conditions yield the four Zoeppritz equations (Appendix D).

The Zoeppritz equations are nonlinear with respect to velocities and density, therefore many forms of approximations have been used that try to linearize them, with one of the most popular being by Aki and Richards (1980) who assumed small layer contrasts to try to simplify the equations (Appendix D).

The Zoeppritz equations are nonlinear with respect to velocities and density, therefore many forms of approximations have been used that try to linearize them, with one of the most popular being by Aki and Richards (1980) who assumed small layer contrasts to try to simplify the equations (Appendix D).

The P-wave reflection coefficient at an interface separating two media differs with the angle of incidence, and the way in which this varies is affected by velocity, density, and the relative values of Poisson's ratio in the two media (Ostrander et al. 1984). Poisson's Ratio is defined as the ratio of the strain of expansion in the direction of a stress to the strain of contraction perpendicular to that stress, or for an easier understanding, a simple relationship between P-wave (V_p) and S-wave (V_s) velocities as described in Equation A-6. See Appendix E for more information about velocity and their relationship to the elastic modulus.

$$\sigma = \frac{1/2(V_p/V_s)^2 - 1}{(V_p/V_s)^2 - 1} \quad (\text{A-6})$$

Theory and laboratory measurements have confirmed that high porosity sandstones saturated with fluids tend to exhibit abnormally low Poisson's ratios that often increase in amplitude with incident angle/offset, however these anomalies are not always caused by hydrocarbon accumulations, they can be caused by non-gaseous bodies, abnormally high or low velocity layers, changes in the degree of lithification, change in mineralogy, or numerous other causes (Ostrander et al. 1984).

The Gasmman equations, from 1951, provided the basis for direct hydrocarbon detection, which then were used by other authors (Ostrander et al. 1984, Swan et al. 1995, Castagna et al. 1995, etc) to popularize the methodology which has come to be known as AVO. These equations predict a large drop in V_p and an increase in V_s when gas is introduced into the pore space of compressible brine-saturated sand. This V_p drop, together with the corresponding density change, changes the P-wave reflection coefficient, resulting in a bright spot, dim spot, or phase change (depending on the relative acoustic impedances of the sand and the overlying lithology) and causes a noticeable drop in V_p/V_s (which produces the AVO anomaly). Note that the shalier the sand the less well this technique works (Ostrander et al. 1984).

AVO interpretation is facilitated by cross-plotting the amplitude of an event against $\sin^2\theta$ or \sin^2x (Figure A-6), where θ is the incidence angle (x corresponds to the offset), and the slope (gradient) of a best fit line that is measured as described in Equation A-7.

$$A(\theta) = A + B.\sin^2\theta, \quad (A-7)$$

Where A is the intercept and B the gradient (slope)

In practice, the gradient can also be approximated by the ratio of amplitudes of long (far) to short (near) offset stacks, however these partial stacks can have rather large noise content because the measurements come from pre-stack data.

By using the plot on Figure 6 three classes of AVO anomalies were initially proposed by Rutherford and Williams (1982), and a fourth class was later proposed by Castagna and Swan (1997). Table A-1 summarizes these classes based on their relative impedance response, their quadrant of appearance and the amplitude variation with offset.

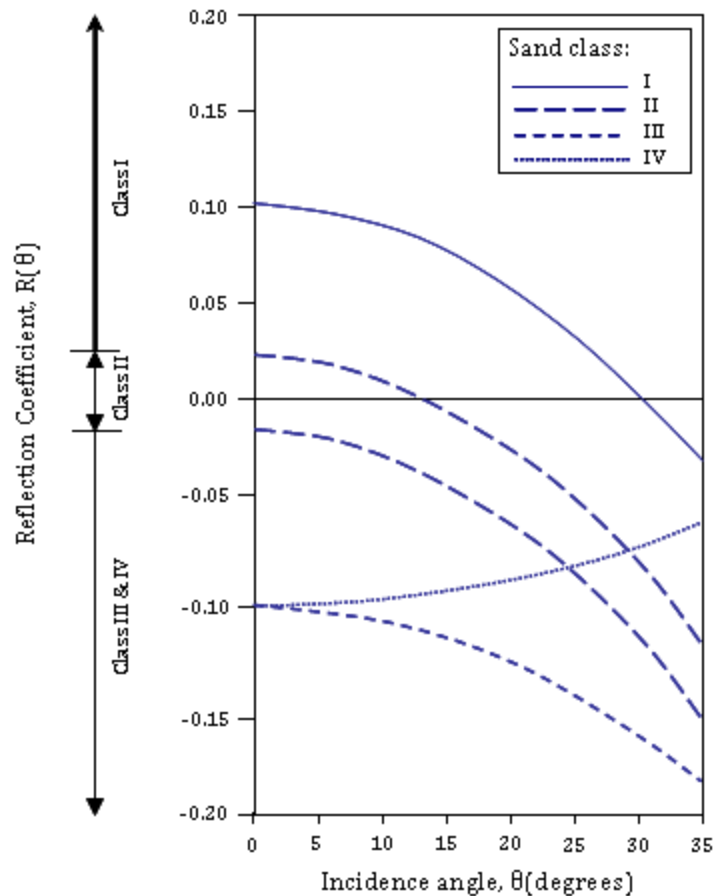


Figure A-9. Class I to III gas-sands classification done by Rutherford and Williams (1989), based on normal incidence reflection coefficients, with a Class IV gas-sand superimposed proposed by Castagna (1997). The vertical axis is reflection coefficient and the horizontal axis is local angle of incidence. Note that Class III and IV may have identical normal incidence reflection coefficients decreases with increasing angle of incidence while Class III reflection coefficient magnitudes increase.

AVO modeling forms one of the main components of AVO analysis, and consists of generating pre-stack synthetic gathers using a full elastic wave equation. The inputs for this task are a P-wave sonic, S-wave sonic, and a density log, with the results being a pre-stack synthetic seismogram for a multilayer Earth model.

The analysis to be performed consists of predicting whether there is an anomalous amplitude response with increasing offset, and if so, what

defines this response (type of AVO anomaly). If an AVO anomaly is present, then a seismic attribute analysis by using near, mid and far angle stack as input seismic files could help to define the extensions of the anomalies, and by subtracting far from near angle stack attributes, sweet spots (favorable location to drill a well defined by an amplitude anomaly) can be mapped.

Class	Relative Impedance	Quadrant	A	B	Amplitude vs. Offset
I	Higuer than overlying unit	IV	+	-	Decreases
II	About the same as overlying unit	II, II, or IV	+ or -	-	Increase or decrease
III	Lower than overlying unit	III	-	-	Increases
IV	Lower than overlying unit	II	-	+	Decreases

Table A-1. Chart summarizing the AVO classes associated with gas sands normally encountered in exploration (Rutherford and Williams, 1982, and Castagna et al. 1997).

Integrating the AVO modeling results with seismic attributes and some additional well logs (gamma ray, density and resistivity) can be a powerful tool for identifying potential hydrocarbon reservoirs, as is shown in the example from Figure A-10.

4. Coherency. Coherence is a geometric seismic attribute introduced in 1995 by Amoco Production Research (Bahorich and Farmer, 1995). This attribute represents a measurement of lateral changes in the seismic response caused by variation in structure, stratigraphy, lithology, porosity, and the presence of hydrocarbons (Marfurt et al. 1998).

Coherence measurements in three dimensions represent the trace-to-trace similarity and therefore produce interpretable changes. Similar traces are

mapped with high coherence coefficients, while discontinuities have low coefficients. For example, a region where faults are cutting the seismic traces will result in sharp discontinuities of trace-to-trace coherence, resulting in delineation by low coherence along fault planes (Chopra et al. 2002).

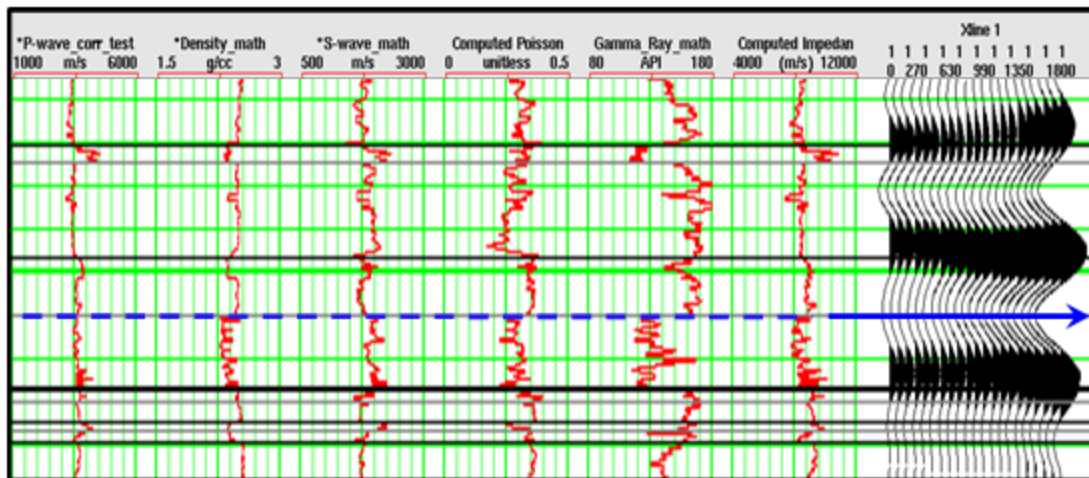


Figure A-10. Sample AVO modeling results from a well located in the Meltwater Field (East of the NPRA). The blue dashed line represents the top of interbedded sandstones with shale reservoir (see GR log) that has a decrease in P-wave and a noticeable increase in S-wave velocity suggesting the presence of a fluid and causing a decrease in the Poisson's ratio values, which is a very characteristic response of sandstone fluid reservoirs (Castagna et al. 1995). The density log at the same marker shows a decrease in density that suggests an increase in porosity, while the pre-stack synthetic shot gathers can be described by a negative intercept and gradient (trough increases its magnitude in the far offset). By integrating this information it can be concluded that this reservoir describes a Class II to III AVO Anomaly based on Rutherford and Williams's (1989) classification.

Many different statistical measures have been used to calculate coherence cubes, with the following three being among the most common used today:

4.1) Cross-correlation-based Coherence. All coherence methods operate on a spatial window of neighboring traces with the simplest of all being the cross-correlation algorithm that operates on three neighboring traces.

Assuming that we have a couple of traces, with one being the master trace and the second the target trace, we can slide the target trace by an amount τ_x and define a vertical analysis windows to range between $\pm K$ samples above and below our analysis point at a time t , if so we can write the normalized cross-correlation coefficients ρ_x as described on Equation A-8.

$$\rho_x(t, \tau_x) = \frac{\sum_{k=-K}^{+K} \{ [u_0(t + k\Delta t) - \mu_0(t)] [u_1(t + k\Delta t - \tau_x) - \mu_1(t - \tau_x)] \}}{\sqrt{\left\{ \sum_{k=-K}^{+K} [u_0(t + k\Delta t) - \mu_0(t)]^2 \sum_{k=-K}^{+K} [u_1(t + k\Delta t - \tau_x) - \mu_1(t - \tau_x)]^2 \right\}}} \quad (\text{A-8})$$

Where the running window mean of the n th trace is defined by $\langle u_n \rangle(t)$ (equation A-9).

$$\langle u_n \rangle(t) = \frac{1}{2K + 1} \sum_{k=-K}^{+K} u_n(t + k\Delta t) \quad (\text{A-9})$$

In most cases $\langle u_n \rangle(t)$ is assumed to be equal to zero, because we know that the true mean of properly processed seismic data is 0, which is a reasonable approximation if the analysis window is greater than a seismic wavelet (Chopra and Marfurt, 2007).

So in summary what this type of coherency does is to estimate the apparent dips in the in-line and cross-line directions. Then, an approximate coherence is calculated by combining cross-correlation coefficients along these two apparent dips, and finally a cube of 3D coherence is created by continuing this process for all samples and all traces in the volume (Chopra, 2002).

4.2) Semblance-based Coherence. The semblance approach needs a space and a time, or a 3D analysis window to be defined for the data. Additionally a dip and azimuth also needs to be defined for each point in the data volume that can be done through flattening using a semblance-driven dip scan method defined by Marfurt et al. (1999).

If we define a rectangular analysis window containing J traces centered about the analysis point, we can define then the semblance $\sigma(t,p,q)$ to be the ratio of the energy of average trace to the average energy of all the traces along a specified dip (equation A-10).

$$\sigma(t, p, q) = \frac{\left[\frac{1}{J} \sum_{j=1}^J u_j(t - px_j - qy_j) \right]^2}{\frac{1}{J} \sum_{j=1}^J \{ [u_j(t - px_j - qy_j)]^2 \}} \quad (\text{A-10})$$

Where the subscript j denotes the j th trace falling within the analysis window; x_j and y_j are the x and y distances of the j th trace from the center of the analysis window, and the apparent dips p and q are measured in milliseconds per meter of foot and define a local planar event at time t (Chopra and Marfurt, 2007). This semblance can be interpreted as the ratio of the energy of the average trace within the analysis window to the average energy of the independent traces (Chopra, 2002).

4.3) Eigen-value-based Coherence. This is a third generation algorithm based on Eigen-structure decomposition (Gersztenkorn and Marfurt, 1999). In this calculation, the reflector dip/azimuth is obtained from smoothed estimates acquired by the more computationally efficient semblance algorithm (Marfurt et al. 1998). Then, the data is flattened in each analysis window; a covariance matrix between the traces is created, and from there the largest Eigen-value is calculated. The Eigen-vector that corresponds to this largest Eigen-value defines a relative trace-to-trace amplitude variation along the reflector that best fits the data for all time samples within the analysis window. Physically, the data represented by a single Eigen-vector will have arbitrary amplitude variations but an identical waveform within the analysis window. With this interpretation, this third generation estimate of coherence is defined as the ratio of energy that can be represented by this Eigen-vector to the energy of the independent traces. Given this definition, we can conclude that this type of coherence cube is only sensitive to

waveform and not to amplitude variations, and will in general provide a sharper delineation of discontinuities. However, this algorithm degenerates as the temporal analysis window becomes smaller, when it becomes increasingly easy to fit all the data in the window with a single spatial amplitude variation (Chopra, 2002).

6. Sweetness. This seismic attribute was developed by Radovich and Oliveros (1998) with the goal of identifying shales and sandstones in clastic successions. Mathematically, it is derived by dividing instantaneous amplitude (also known as reflection strength or instantaneous envelope) by the square root of the instantaneous frequency (equation 11). The units for sweetness are difficult to understand physically, so, this attribute is best thought as a relative value (Hart, 2008).

$$Sweetness = \frac{I_{Amp}}{\sqrt{I_{freq}}} \quad (A-11)$$

Shale-dominated intervals tend to be characterized by low amplitudes (small acoustic impedance contrasts) and relatively closely spaced reflections (high frequency), whereas isolated sandy intervals, such as channel fills and frontal splays, in the shales correspond to high amplitude (high acoustic impedance contrast with the shales) and low frequency (Hart et al. 2008).

Parts of the seismic volume described by both high amplitudes and low frequencies will have high sweetness values; consequently, low amplitudes with high frequencies will have low sweetness values (Figure A-11).

Sweetness, although a very useful attribute in many cases does not respond properly when the contrast between sand and shales is low, or if the destructive interference from reflections above and below the sand prevent high amplitude reflections from developing (Hart, 2008).

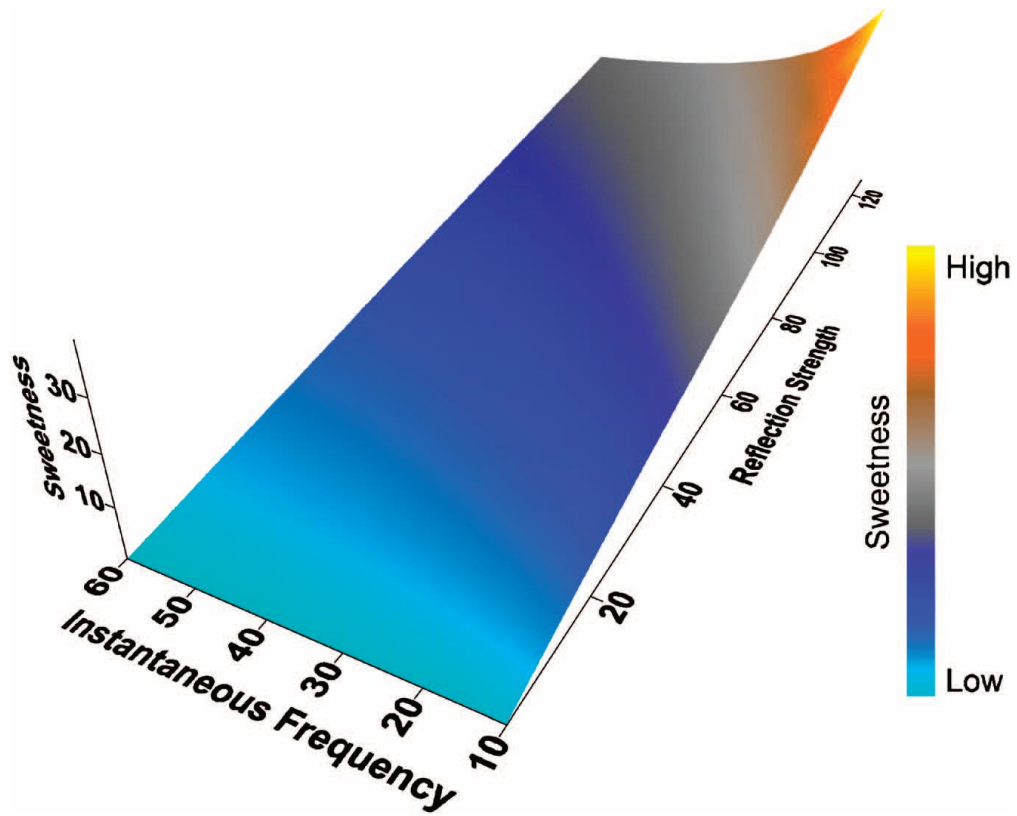


Figure A-11. Three dimensional plot showing sweetness on the vertical axis as a function of instantaneous frequency and reflection strength. High sweetness values are directly associated to high reflection strength and high instantaneous frequency values (Hart, 2008).

APPENDIX B: Derivation of trace envelope

The trace envelope can be defined as a function that, at any given time, is the maximum value that a seismic trace can attain through a constant phase rotation. This definition takes us to a mathematical expression for the envelope as well as to a formula for the phase rotation angle (Barnes, 2007).

Ideally, a phase rotation changes the phase spectrum by a constant angle without altering the amplitude spectrum. A phase rotator that subtracts an angle θ can be expressed as a time-domain convolutional operator $p(t, \theta)$ given by equation B-1.

$$p(t, \theta) = \delta(t) \cos \theta + h(t) \sin \theta \quad (\text{B-1})$$

Where $\delta(t)$ is the delta function and $h(t)$ is the quadrature filter or Hilbert transform operator (Appendix C). Applying the quadrature filter to a seismic trace $x(t)$ produces a quadrature trace $y(t)$. Applying the phase subtractor $p(t, \theta)$ to a seismic trace $x(t)$ produces a rotated trace $x'(t)$ given as described on equation B-2.

$$x'(t) = p(t, \theta) * x(t) = x(t) \cos \theta + y(t) \sin \theta \quad (\text{B-2})$$

The change of the rotated trace with respect to the rotation angle θ is given in equation B-3:

$$\frac{\partial x'(t)}{\partial \theta} = -x(t) \sin \theta + y(t) \cos \theta \quad (\text{B-3})$$

Let $\theta(t)$ be the rotation angle that at time t maximizes the value of the rotated trace. By definition, the envelope $a(t)$ equals this maximum value. Hence from Equation B-2 we obtain equation B-4:

$$a(t) = x(t) \cos \theta(t) + y(t) \sin \theta(t) \quad (\text{B-4})$$

When the rotated trace equals the envelope, its change with respect to rotation angle θ is zero and $\theta = \theta(t)$. Hence from equation B-3:

$$\frac{\partial a(t)}{\partial \theta(t)} = 0 = -x(t) \sin \theta(t) + y(t) \cos \theta(t) \quad (\text{B-5})$$

$$x(t) \sin \theta(t) = y(t) \cos \theta(t) \quad (\text{B-6})$$

An expression for trace envelope follows by squaring equation B-4 and B-5 and adding them to obtain equation B-7.

$$a(t) = \sqrt{x^2(t) + y^2(t)} \quad (\text{B-7})$$

And lastly, an expression for the phase rotation angle is obtained from equation B-6 as displayed on equation B-8:

$$\theta(t) = \arctan \left[\frac{y(t)}{x(t)} \right] \quad (\text{B-8})$$

APPENDIX C: Hilbert Transform

The Hilbert transform or quadrature filter is an ideal phase rotator that subtracts 90° of phase from a seismic trace. Convolving the Hilbert transform operator $h(t)$ with a cosine wave that has arbitrary amplitude a , arbitrary but nonzero constant frequency f , and constant phase θ produces a sine wave of the same amplitude, frequency, and phase, just as described on equation C-1.

$$h(t) * a \cos(2\pi ft + \theta) = a \sin(2\pi ft + \theta) \quad (\text{C-1})$$

With the constraint of linearity, equation C-1 uniquely defines the Hilbert transform (Vakman, 1998). Some authors define the Hilbert transform such that it adds 90° phase, which reverses the sign of the quadrature trace (e.g., Claerbout, 1985).

The Hilbert transform operator $h(t)$ has the form of equation C-2.

$$h(t) = \frac{1}{\pi t} \quad (\text{C-2})$$

While the Fourier transform $H(f)$, has the form described on equation C-3.

$$H(f) = \begin{cases} -i & f > 0 \\ +i & f < 0 \\ 0 & f = 0 \end{cases} \quad (\text{C-3})$$

The discrete Hilbert transform operator $h(n)$, where n is the sample index is defined in equation C-4.

$$h(n) = \begin{cases} \frac{2}{n\pi} & n \text{ odd} \\ 0 & n \text{ even or } 0 \end{cases} \quad (\text{C-4})$$

This operator drops off slowly with sample n and so requires long lengths in application, though half the samples are zero and can be ignored.

Hilbert transformation is a key step in complex seismic trace analysis. It is often accomplished in the frequency domain as follows. The Hilbert transform of a seismic trace $x(t)$ is the quadrature trace $y(t) = h(t)*x(t)$; these have Fourier transform $X(f)$ and $Y(f) = H(f)X(f)$. The seismic and quadrature traces are combined to form a complex trace $z(t) = x(t)+iy(t)$, which has Fourier transform $Z(f) = iY(f)$. Substituting $H(f)X(f)$ for $Y(f)$ and, by equation B-3, substituting $-i\sin(f)$ for $H(f)$, it can be shown that $Z(f)$ is one-sided according to equation C-5.

$$Z(f) = \begin{cases} 2X(f) & f > 0 \\ 0 & f \leq 0 \end{cases} \quad (\text{C-5})$$

Equation C-5 implicitly performs Hilbert transformation and is used to produce a complex seismic trace directly from a real seismic trace. This illustrates the mathematical convenience afforded by the complex trace.

An ideal phase rotator that subtracts an angle θ can be expressed in terms of the Hilbert transform. The spectrum of an ideal phase subtractor $P(f, \theta)$ is defined on equation C-6.

$$P(f, \theta) = \begin{cases} \exp(-i\theta) = \cos \theta - i \sin \theta & f > 0 \\ \exp(+i\theta) = \cos \theta + i \sin \theta & f < 0 \\ \cos \theta & f = 0 \end{cases} \quad (\text{C-6})$$

Recalling the frequency-domain representation of the Hilbert transform (equation C-3), equation C-6 can be written as:

$$P(f, \theta) = \cos \theta + H(f) \sin \theta \quad (\text{C-7})$$

Inverse Fourier transforming yields the time-domain operator $p(t, \theta)$ for the ideal phase subtractor described on equation C-8.

$$p(t, \theta) = \delta(t) \cos \theta + h(t) \sin \theta \quad (\text{C-8})$$

APPENDIX D: Zoeppritz equations.

The Zoeppritz equations are used in AVO studies to describe the reflection and transmission coefficients as a function of incident angle and elastic media properties (density, P-wave and S-wave velocities). They apply to the reflection of plane-waves between two half-spaces, and do not include wavelet interferences due to layering (Castagna et al. 1993).

The Zoeppritz equations for an incident plane P-wave of unity amplitude are described by a convenient matrix equation given by $Q=P.R$.

$$P = \begin{pmatrix} \cos \theta_{p1} & -\sin \theta_{s1} & \cos \theta_{p2} & \sin \theta_{s2} \\ \sin \theta_{p1} & \cos \theta_{s1} & -\sin \theta_{p2} & \cos \theta_{s2} \\ Z_1 \cos 2\theta_{s1} & -W_1 \sin \theta_{s1} & -Z_2 \cos 2\theta_{s2} & -W_2 \sin 2\theta_{s2} \\ (V_{s1}/V_{p1})W_1 \sin 2\theta_{p1} & W_1 \cos 2\theta_{s1} & (V_{s2}/V_{p2})W_2 \sin 2\theta_{p2} & -W_2 \cos 2\theta_{s2} \end{pmatrix}$$

$$R = \begin{pmatrix} A \\ B \\ C \\ D \end{pmatrix} ; \quad Q = \begin{pmatrix} \cos \theta_{p1} \\ -\sin \theta_{s1} \\ -Z_1 \cos 2\theta_{s1} \\ (V_{s1}/V_{p1})W_1 \sin 2\theta_{p1} \end{pmatrix}$$

From the previous matrixes, $Z_i = \rho_i V_{pi}$, $W_i = \rho_i V_{si}$, and A, B, C, D are respectively the amplitude of the reflected P and S-waves and the transmitted values at and beyond the critical angle (Castagna et al. 1993).

Because the Zoeppritz equations are highly nonlinear with respect to velocities and density, many approximations have been made in order to linearize them. Aki and Richards (1980) assumed small layer contrasts, simplifying the relationship as described in equations D-1.

$$R(\theta) = \frac{1}{2 \cos^2(\theta)} I_p - 4\gamma^2 \sin^2(\theta) I_s + (2\gamma^2 \sin^2(\theta) - 0.5 \tan^2(\theta)) D, \quad (D-1)$$

Where,

$$I_p = \left(\frac{\Delta V_p}{V_p} + \frac{\Delta \rho}{\rho} \right), \quad (\text{D-2})$$

$$I_s = \left(\frac{\Delta V_s}{V_s} + \frac{\Delta \rho}{\rho} \right), \quad (\text{D-3})$$

$$D = \frac{\Delta \rho}{\rho}, \quad (\text{D-4})$$

With:

$$\Delta V_p = V_{p2} - V_{p1}, \quad (\text{D-5})$$

$$\Delta V_s = V_{s2} - V_{s1}, \quad (\text{D-6})$$

$$\Delta \rho = \rho_2 - \rho_1, \quad (\text{D-7})$$

$$V_p = \frac{(V_{p2} + V_{p1})}{2}, \quad (\text{D-8})$$

$$V_s = \frac{(V_{s2} + V_{s1})}{2}, \quad (\text{D-9})$$

$$\rho = \frac{(\rho_2 + \rho_1)}{2} \quad (\text{D-10})$$

The relative contrasts in P-impedance, S-impedance and density are given by I_p , I_s and D , respectively. θ represents the reflection angle and γ is an estimate of the background shear to compressional velocity ratio V_s/V_p .

The reflectivity curves corresponding to either a unit perturbation in P-impedance contrast ($I_p = 1$, $I_s = 0$, $D = 0$), S-impedance contrast or density contrast can be seen in Figure D-1. For a unit perturbation in relative P-impedance contrast, the P-impedance inversion curve dominates at small angles of incidence and increases with offset. For a unit perturbation in relative S-impedance contrast, the S-impedance inversion curve is zero at normal incidence and is increasingly negative with increasing offset. Over

the conventional range of surface reflection data acquisition geometry illumination, which is typically 0° to 35° , the density inversion curve is not significant, as most of the density contrast contributes to the reflection AVO through the impedance contrast alone. As the reflection amplitudes are mostly a combination of the P and S-impedance contrast inversion curves, reflectors with P and S-impedance contrasts of the same polarity and magnitude are expected to show approximately constant amplitude versus offset. On the other hand, reflectors with P and S-impedance contrasts of opposite polarities, indicating a transition zone of changing rock pore fluid properties, should show increasing amplitudes versus offset (Castagna et al. 1993).

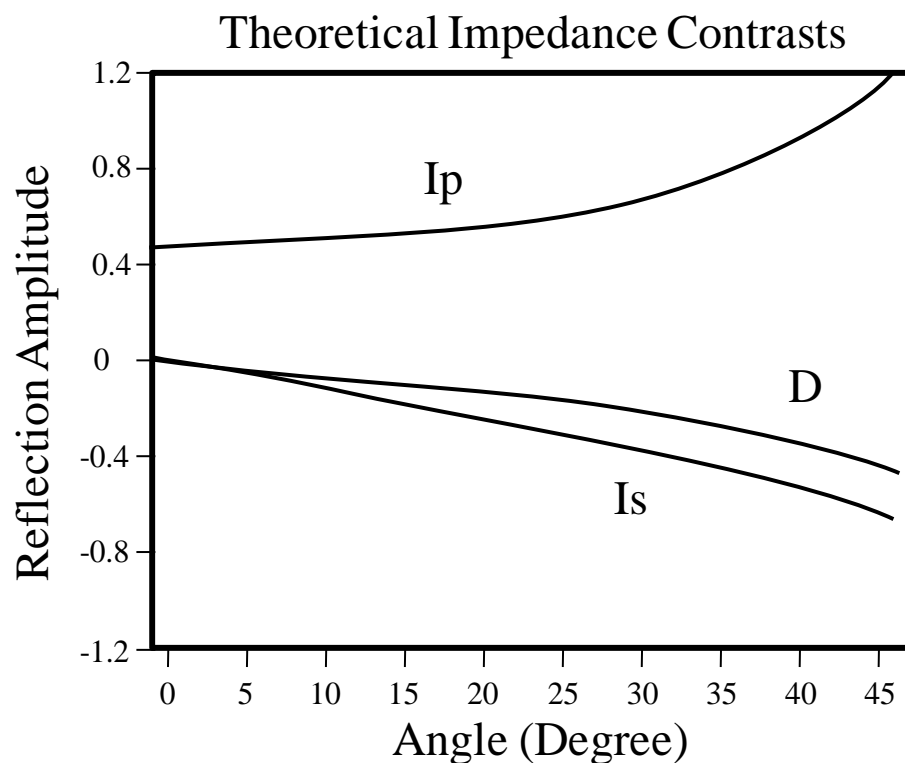


Figure D-1 Theoretical P-wave, S-wave, and Density impedance inversion curve (Stanford Exploration Project 1998).

APPENDIX E: Velocity and Elastic Moduli.

There are two types of waves that are of great interest to us when analyzing seismic data, the compressional wave, or P-wave, and the transverse wave, or S-wave. Equation E-1 and E-2 describe these two wave velocities in an isotropic, homogeneous, and elastic medium.

$$V_p = \left[\frac{k + 4/3\mu}{\rho} \right]^{1/2} \quad (E-1)$$

$$V_s = \left[\frac{\mu}{\rho} \right]^{1/2} \quad (E-2)$$

Where

V_p = compressional wave velocity

V_s = shear wave velocity

k = rock bulk modulus (rock incompressibility)

μ = rock shear modulus (rock rigidity)

ρ = rock bulk density

Equations E-1 and E-2 provide the fundamental link between seismic velocities and rock properties. For example, Domenico (1976, 1977) demonstrated that the rock bulk modulus may be strongly dependent on the pore fluid bulk modulus while the rock shear modulus may be largely unaffected by the presence of fluids. Hence, when a compressible free gas replaces liquids in the pore space, the rock V_p will decrease significantly, whereas the rock V_s velocity will be slightly increased due to the decreasing bulk rock density, with the exception of carbonates and well-cemented sandstones, where the V_s increase will be very subtle if any. Consequently, the ratio of compressional to shear wave velocity (V_p/V_s) is expected to be a considerably good indicator of free gas in the pore space. This is the basis for direct hydrocarbon detection using AVO (Castagna et al.1995).

For a homogeneous isotropic material which is deforming elastically under uniaxial compression, Poisson's ratio (σ) is defined as the negative fractional change in length. Poisson's ratio is directly related to the V_p/V_s ratio by equation E-3.

$$\sigma = \frac{0.5(V_p / V_s)^2 - 1}{(V_p / V_s)^2 - 1} \quad (\text{E-3})$$

A Poisson's ratio equal to zero corresponds to V_p/V_s equal to 1.41. Fluids have a Poisson's ratio of 0.5, where V_p/V_s equals infinity.

The shear modulus (μ) is the ratio of shear stress to shear strain. Similarly, the bulk modulus (k) is the ratio of volumetric stress to volumetric strain and is the reciprocal of the compressibility (Castagna et al. 1995).

APPENDIX F: Map database

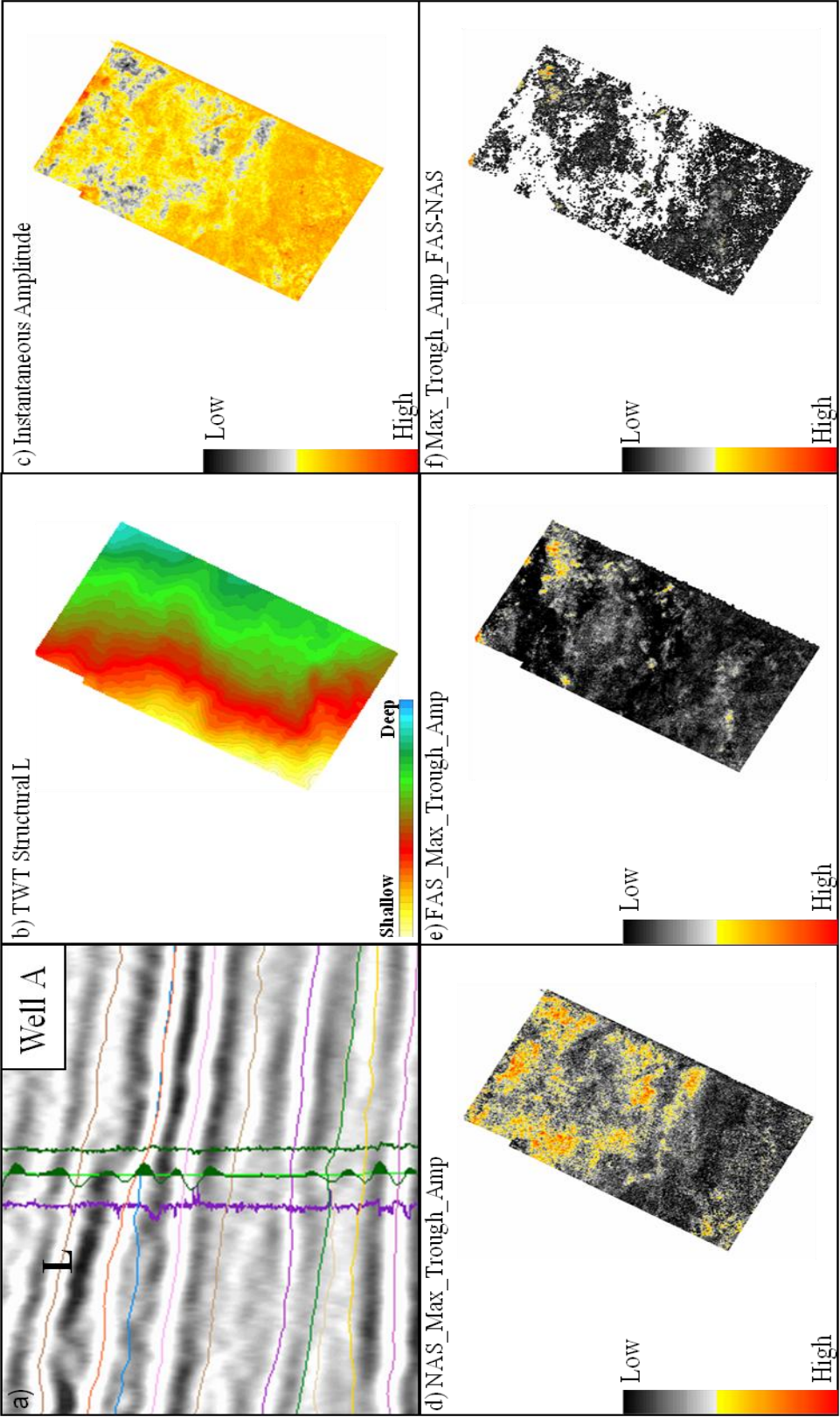


Figure F1. Composite image of marker L. a) west-to-east seismic section showing the seismic character of marker L, b) TWT structural map, c) instantaneous amplitude map, d) maximum trough amplitude calculated from the near angle stack, e) maximum trough amplitude calculated from the far angle stack, and f) difference between far and near maximum trough amplitude.

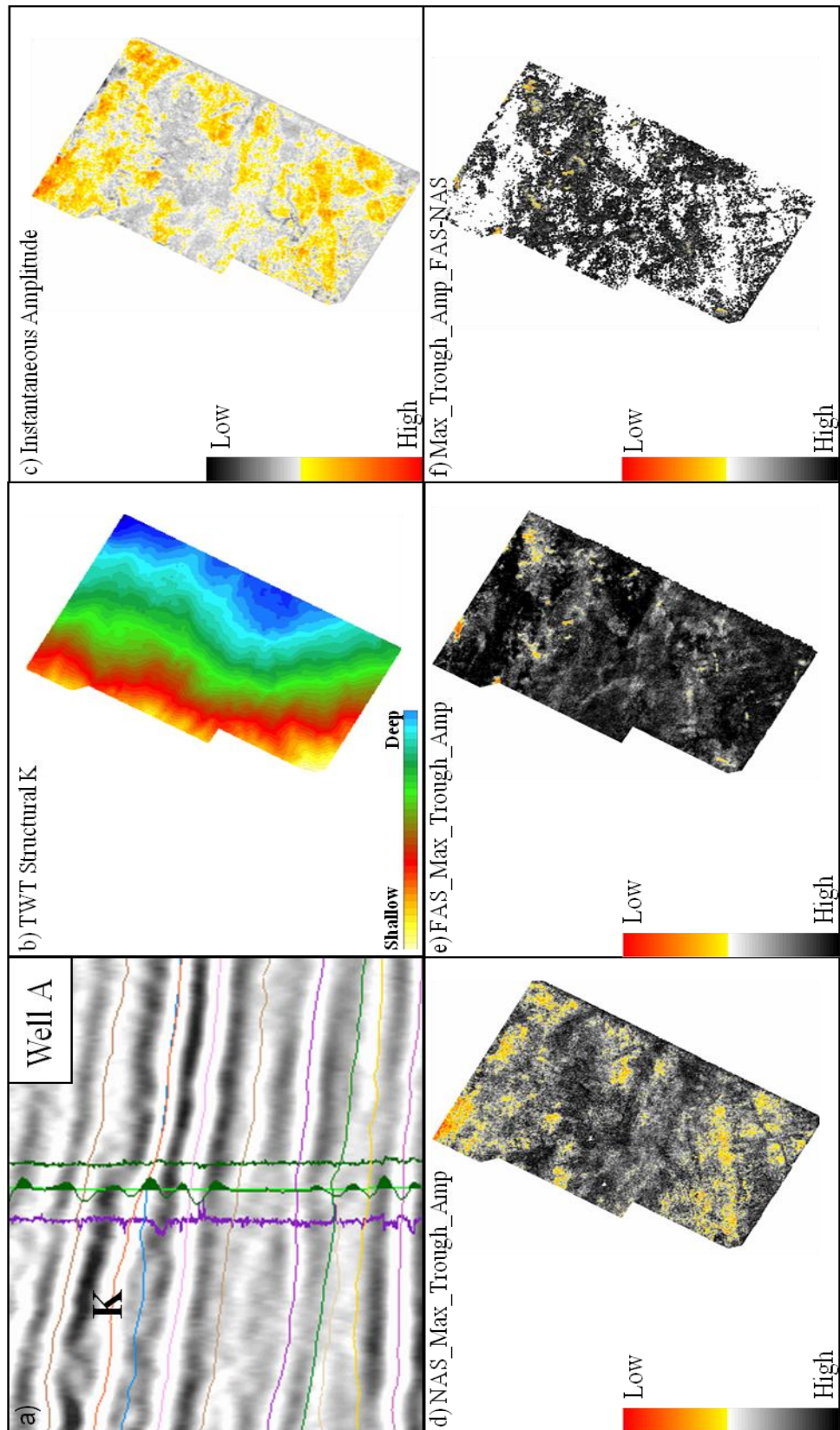


Figure F1. Composite image of marker K. a) west-to-east seismic section showing the seismic character of marker K, b) TWT structural map, c) instantaneous amplitude map, d) maximum trough amplitude calculated from the near angle stack, e) maximum trough amplitude calculated from the far angle stack, and f) difference between far and near maximum trough amplitude.

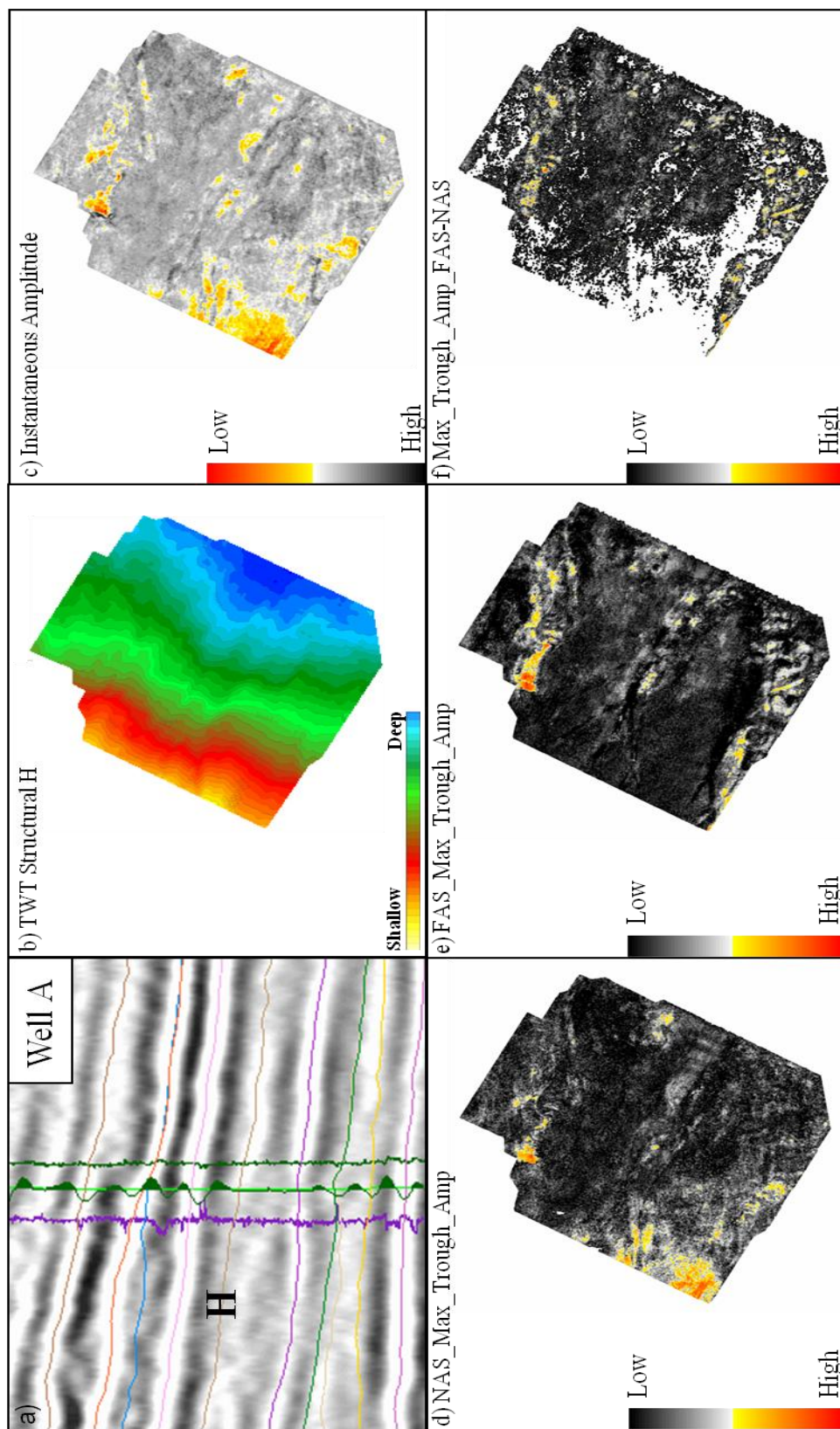


Figure F1. Composite image of marker H. a) west-to-east seismic section showing the seismic character of marker H, b) TWT structural map, c) instantaneous amplitude map, d) maximum trough amplitude calculated from the near angle stack, e) maximum trough amplitude calculated from the far angle stack, and f) difference between far and near maximum trough amplitude.

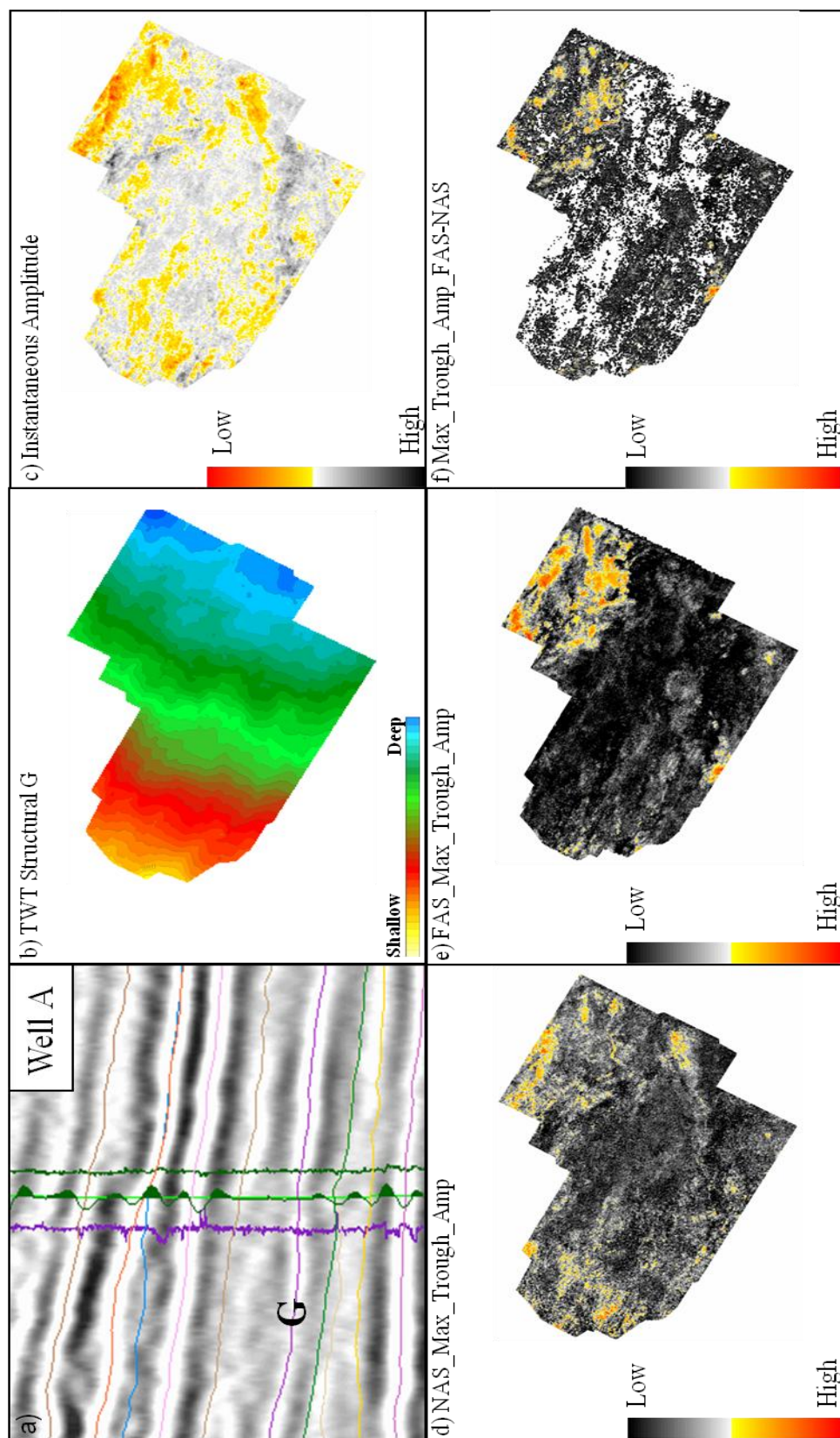


Figure F1. Composite image of marker G. a) west-to-east seismic section showing the seismic character of marker G, b) TWT structural map, c) instantaneous amplitude map, d) maximum trough amplitude calculated from the near angle stack, e) maximum trough amplitude calculated from the far angle stack, and f) difference between far and near maximum trough amplitude.

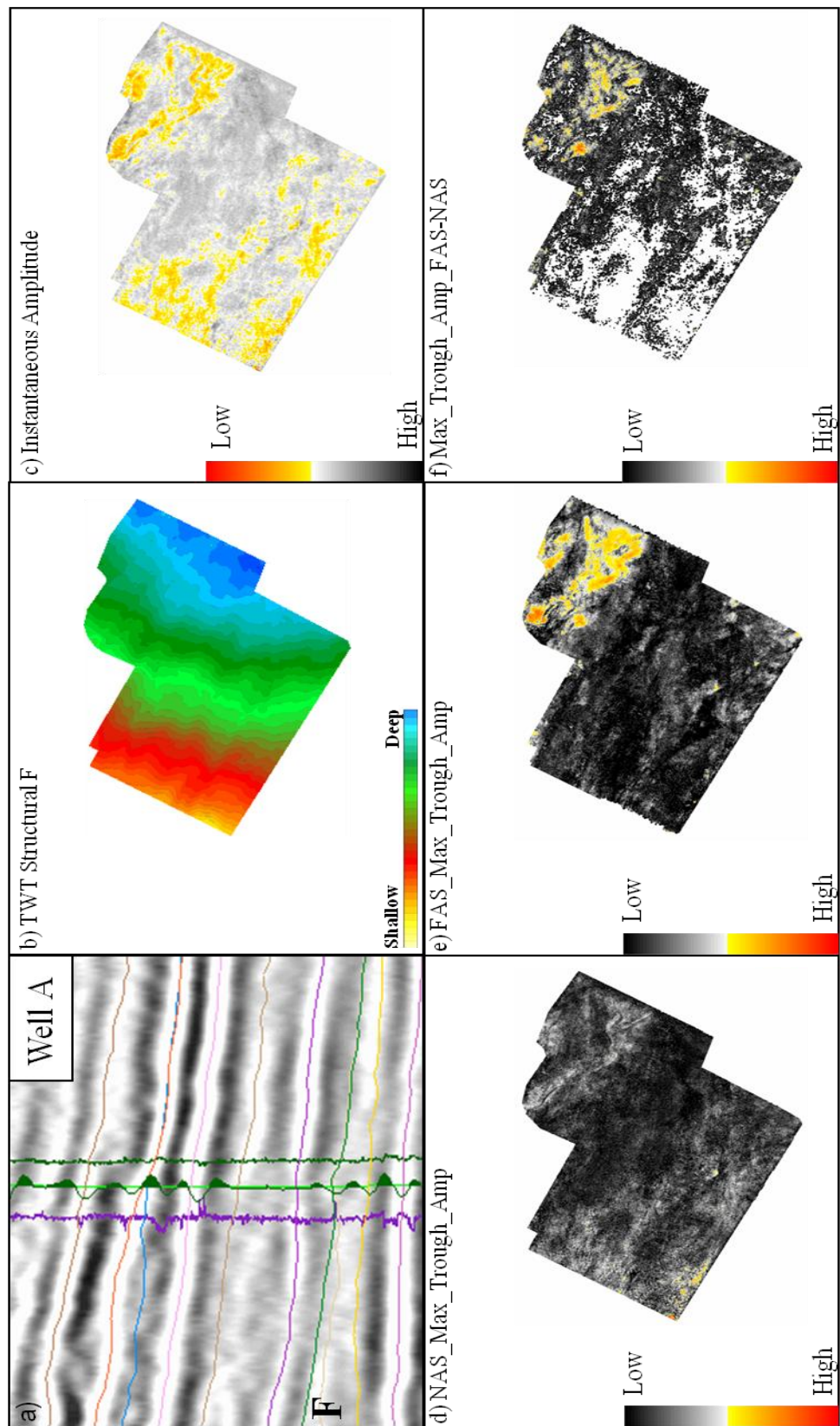


Figure F1. Composite image of marker F. a) west-to-east seismic section showing the seismic character of marker F, b) TWT structural map, c) instantaneous amplitude map, d) maximum trough amplitude calculated from the near angle stack, e) maximum trough amplitude calculated from the far angle stack, and f) difference between far and near maximum trough amplitude.

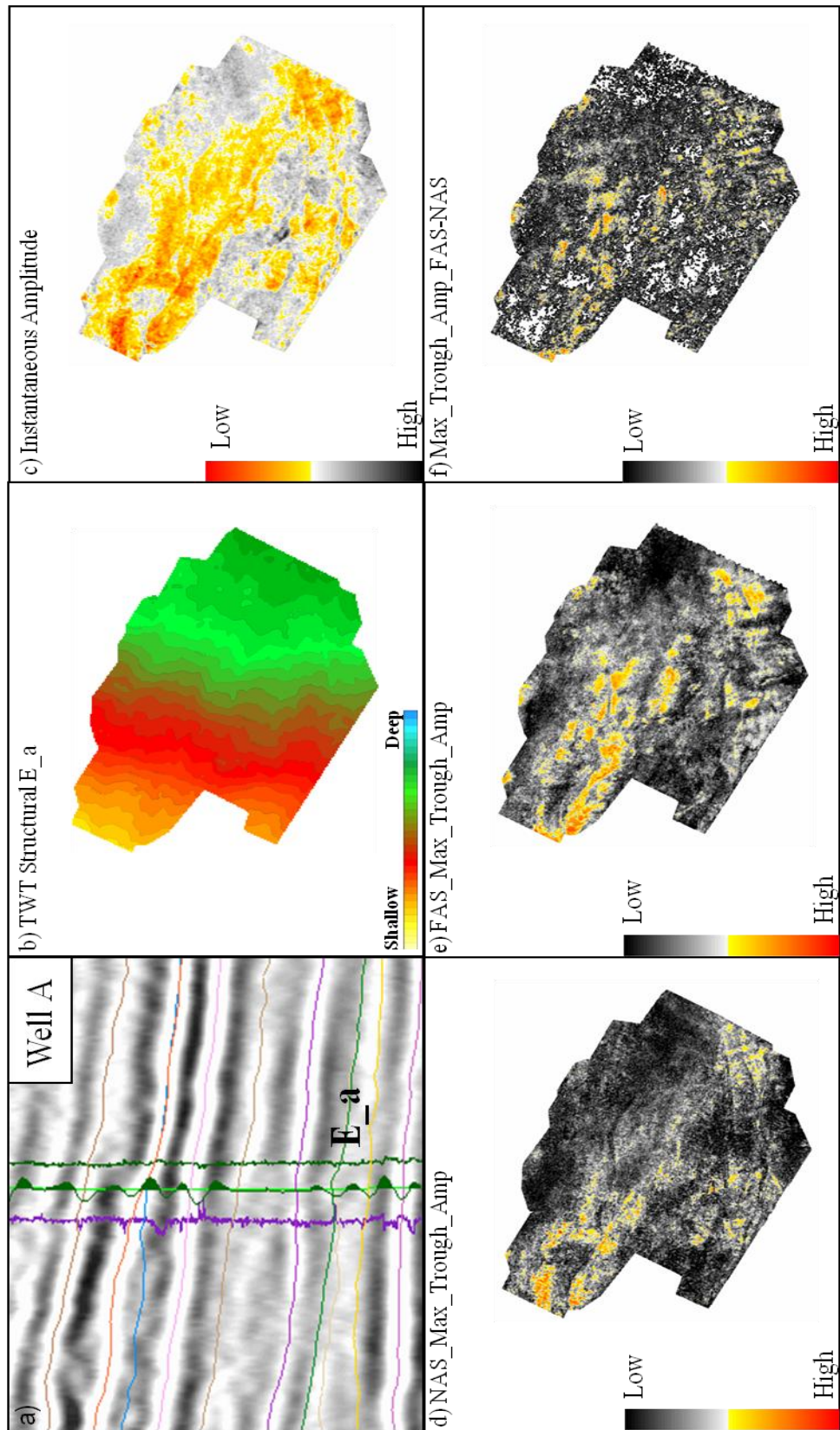


Figure F1. Composite image of marker E_a. a) west-to-east seismic section showing the seismic character of marker E_a b) TWT structural map, c) instantaneous amplitude map, d) maximum trough amplitude calculated from the near angle stack, e) maximum trough amplitude calculated from the far angle stack, and f) difference between far and near maximum trough amplitude.

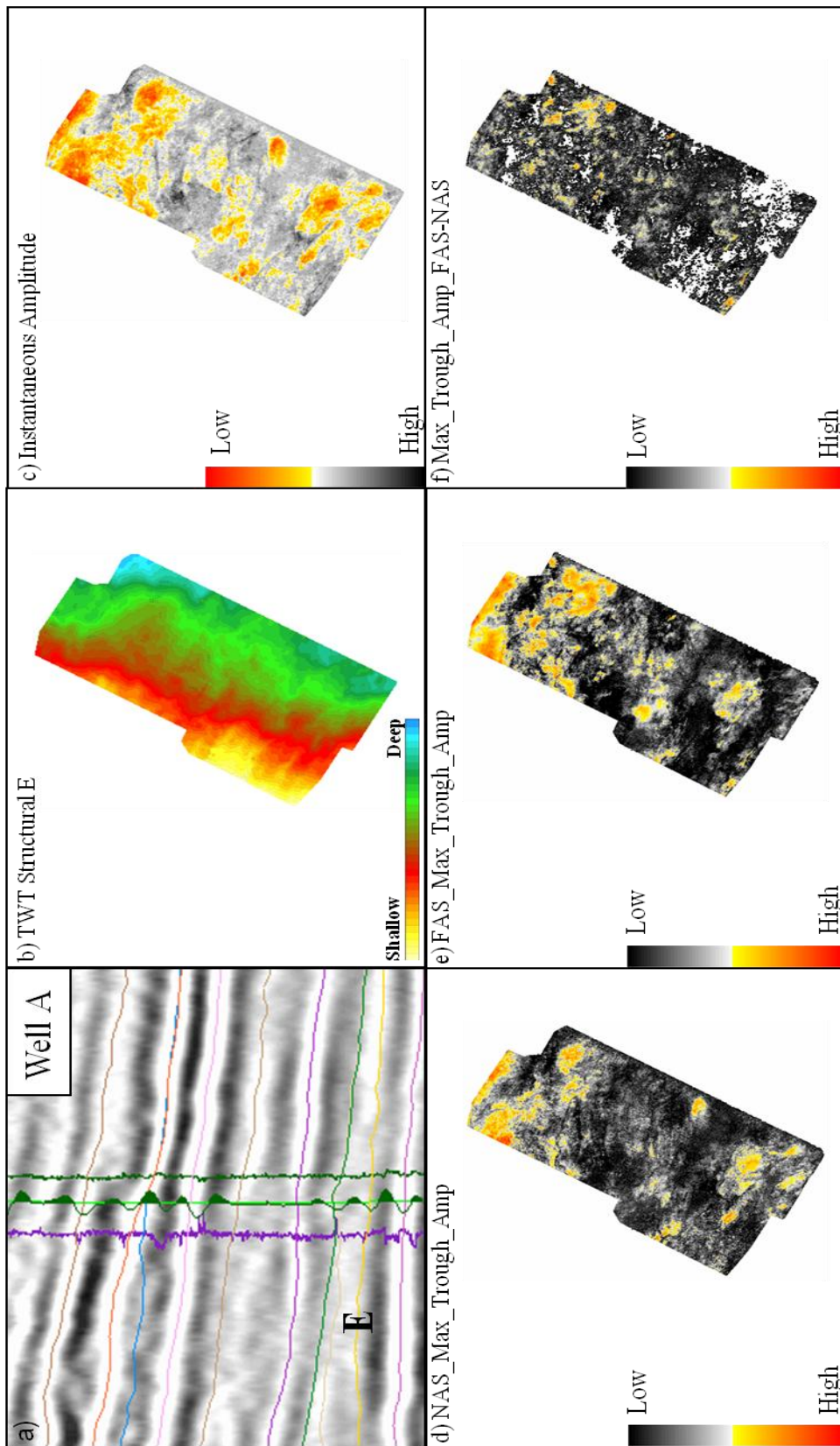


Figure F1. Composite image of marker E. a) west-to-east seismic section showing the seismic character of marker E, b) TWT structural map, c) instantaneous amplitude map, d) maximum trough amplitude calculated from the near angle stack, e) maximum trough amplitude calculated from the far angle stack, and f) difference between far and near maximum trough amplitude.

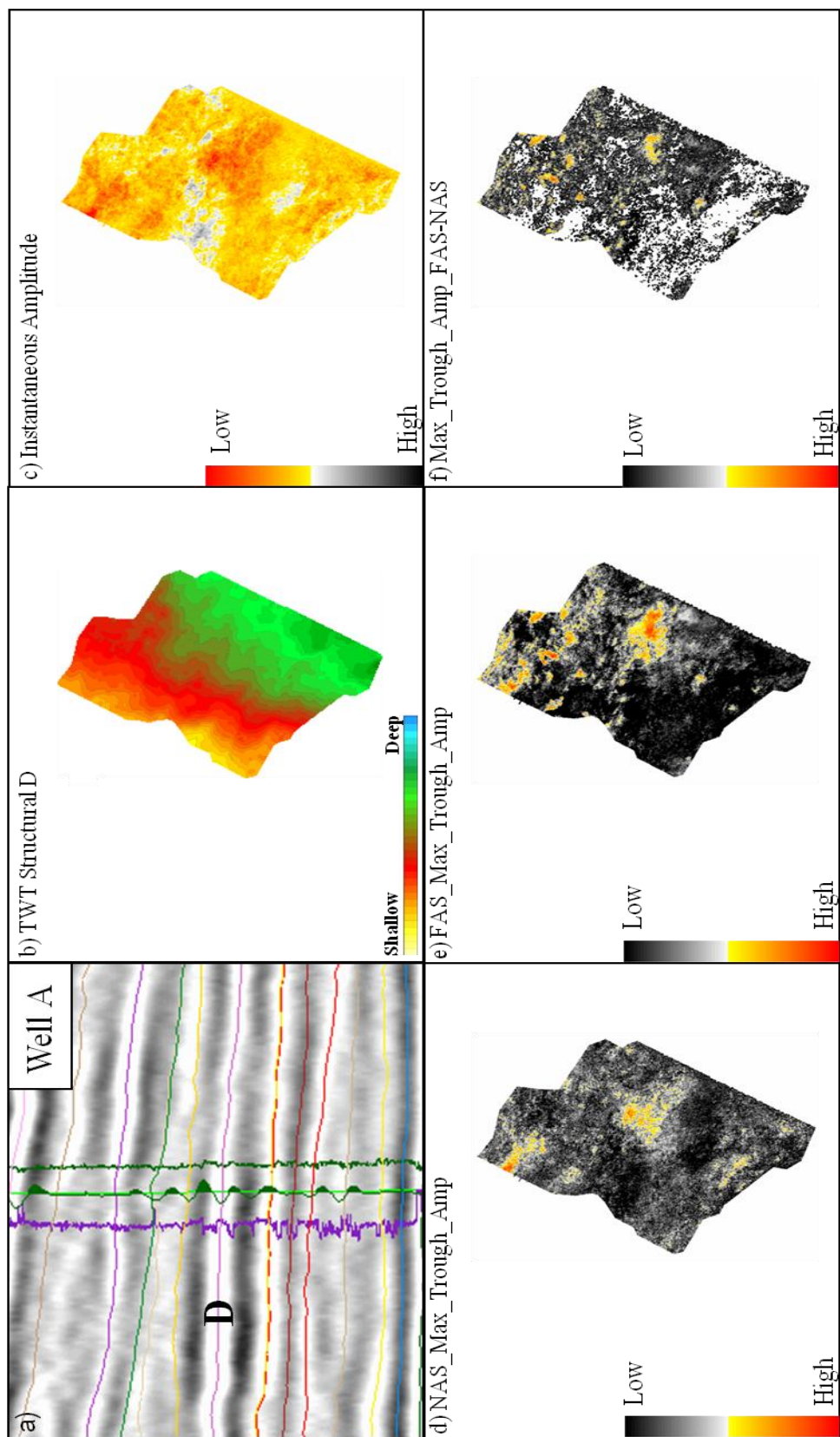


Figure F1. Composite image of marker D. a) west-to-east seismic section showing the seismic character of marker D, b) TWT structural map, c) instantaneous amplitude map, d) maximum trough amplitude calculated from the near angle stack, e) maximum trough amplitude calculated from the far angle stack, and f) difference between far and near maximum trough amplitude.

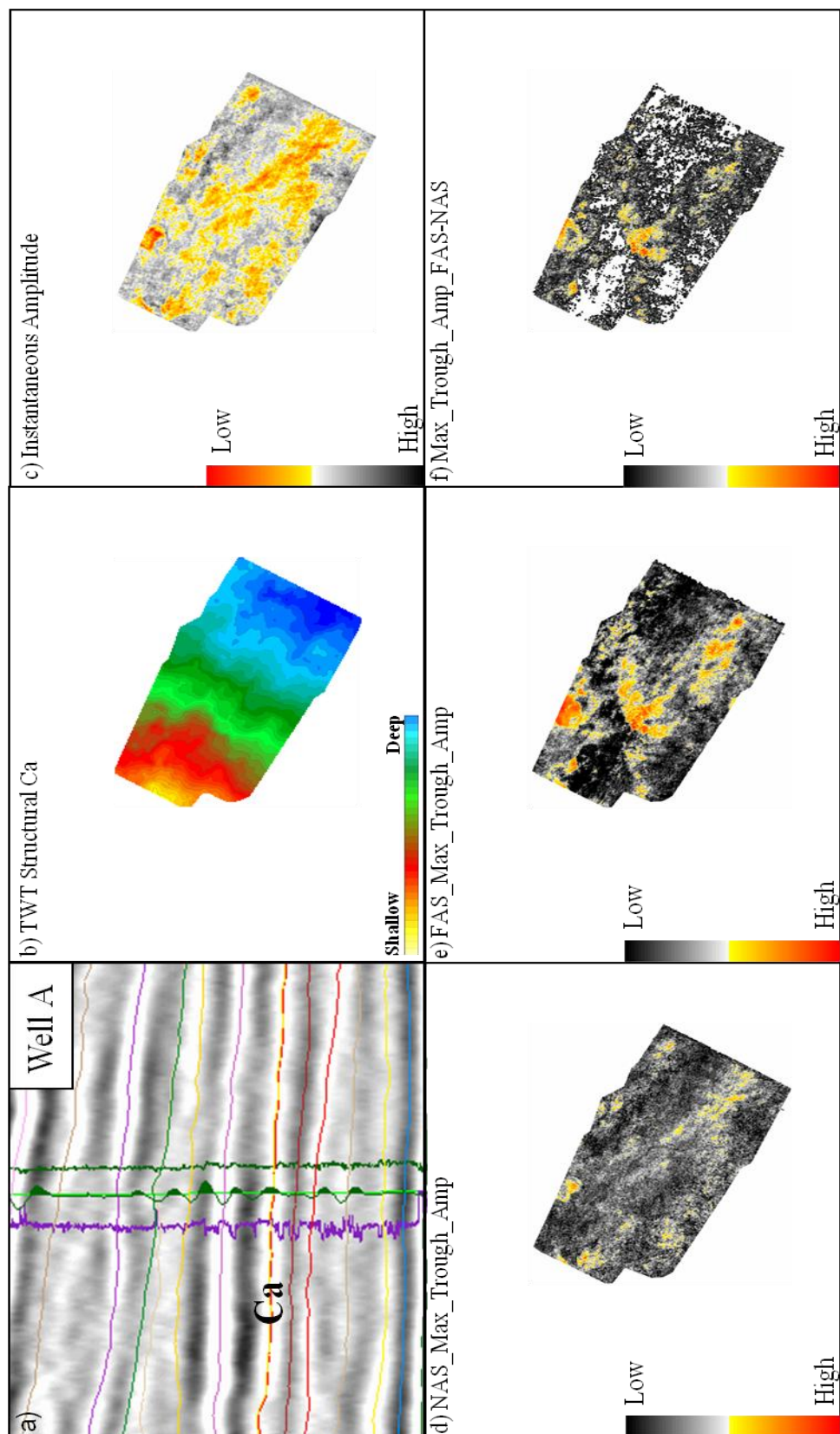


Figure F1. Composite image of marker Ca. a) west-to-east seismic section showing the seismic character of marker Ca, b) TWT structural map, c) instantaneous amplitude map, d) maximum trough amplitude calculated from the near angle stack, e) maximum trough amplitude calculated from the far angle stack, and f) difference between far and near maximum trough amplitude.

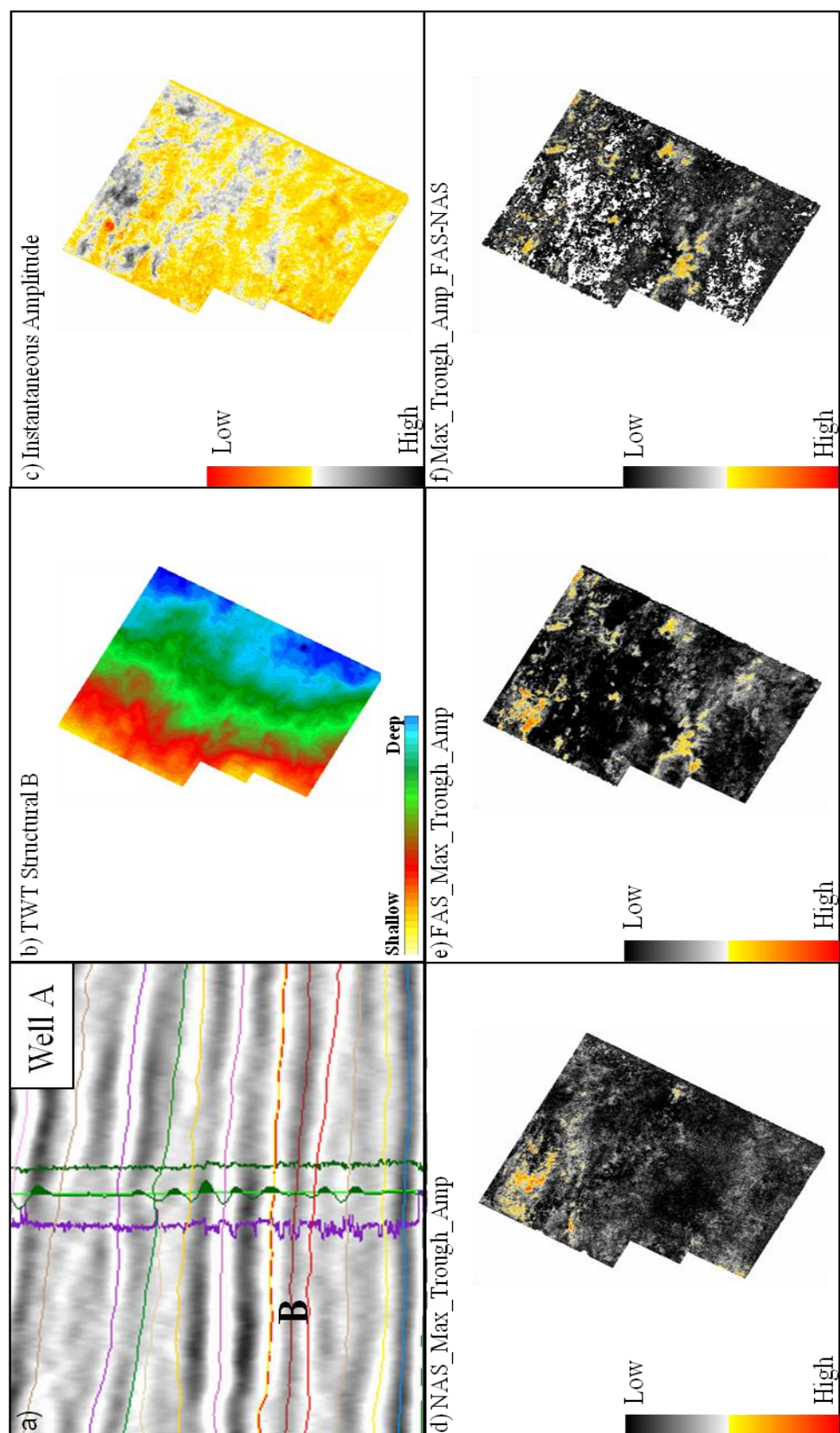


Figure F1. Composite image of marker B. a) west-to-east seismic section showing the seismic character of marker B, b) TWT structural map, c) instantaneous amplitude map, d) maximum trough amplitude calculated from the near angle stack, e) maximum trough amplitude calculated from the far angle stack, and f) difference between far and near maximum trough amplitude.

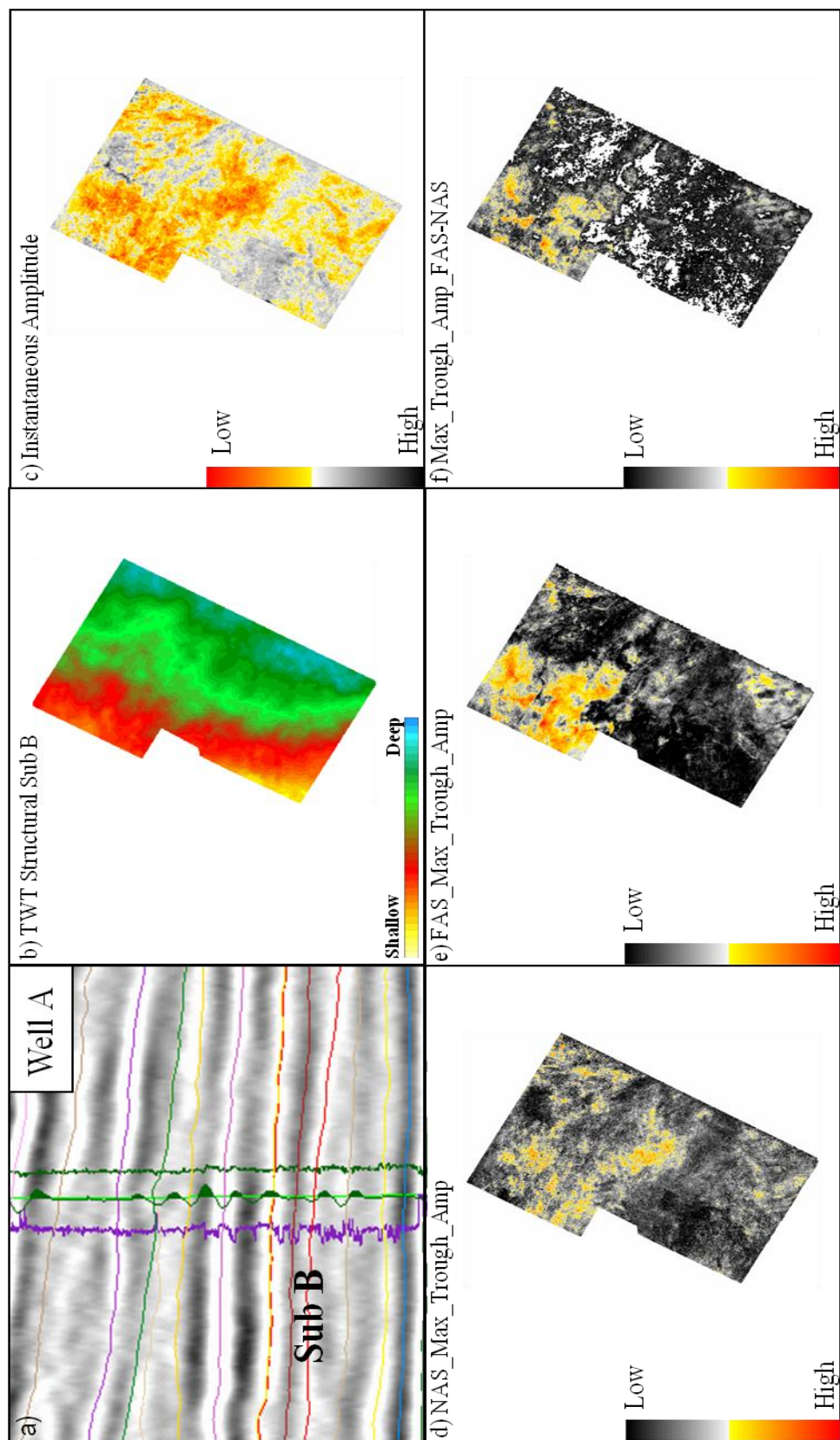


Figure F1. Composite image of marker Sub B. a) west-to-east seismic section showing the seismic character of marker Sub B, b) TWT structural map, c) instantaneous amplitude map, d) maximum trough amplitude calculated from the near angle stack, e) maximum trough amplitude calculated from the far angle stack, and f) difference between far and near maximum trough amplitude.

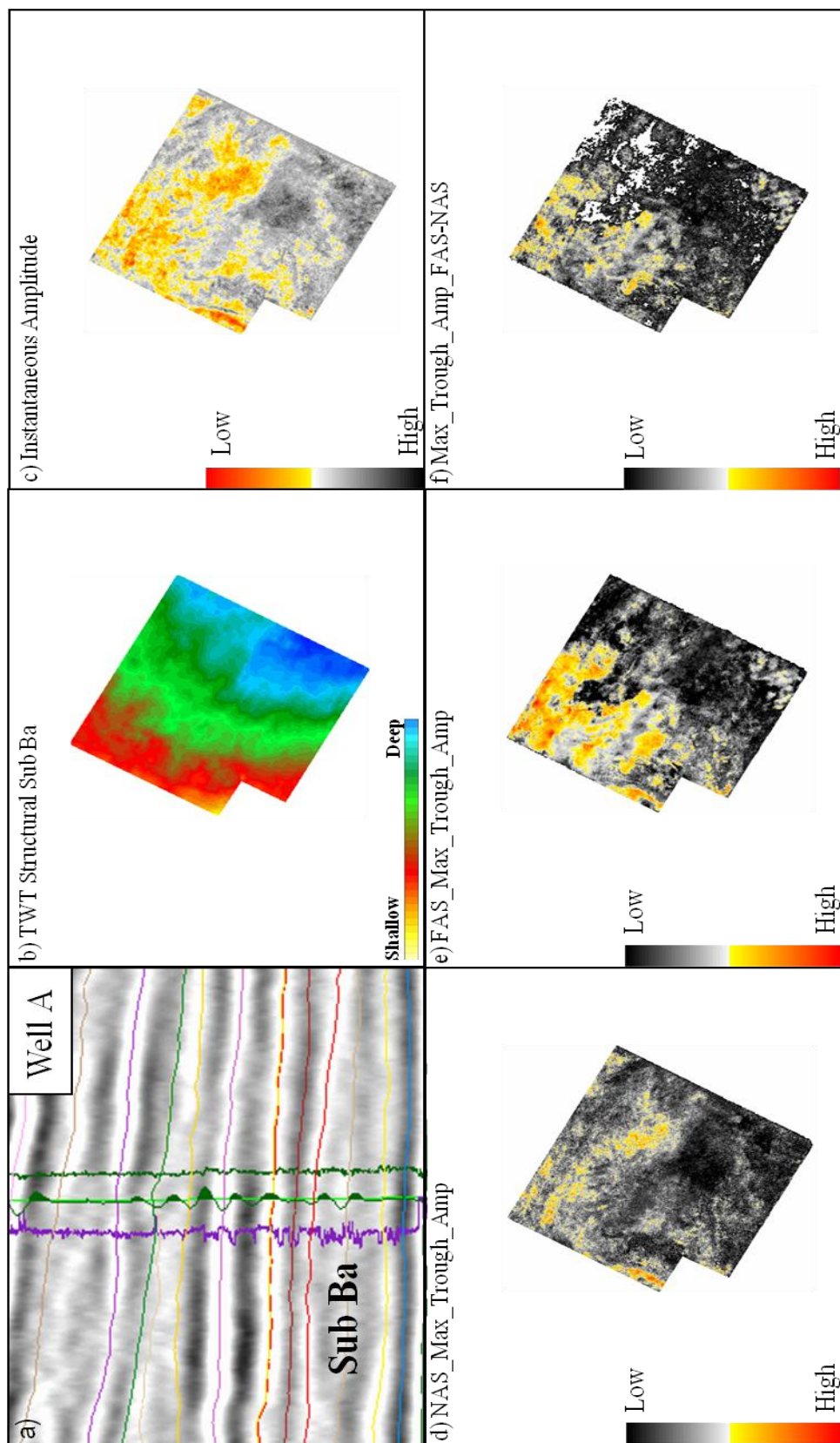


Figure F1. Composite image of marker Sub Ba. a) west-to-east seismic section showing the seismic character of marker Sub Ba, b) TWT structural map, c) instantaneous amplitude map, d) maximum trough amplitude calculated from the near angle stack, e) maximum trough amplitude calculated from the far angle stack, and f) difference between far and near maximum trough amplitude.

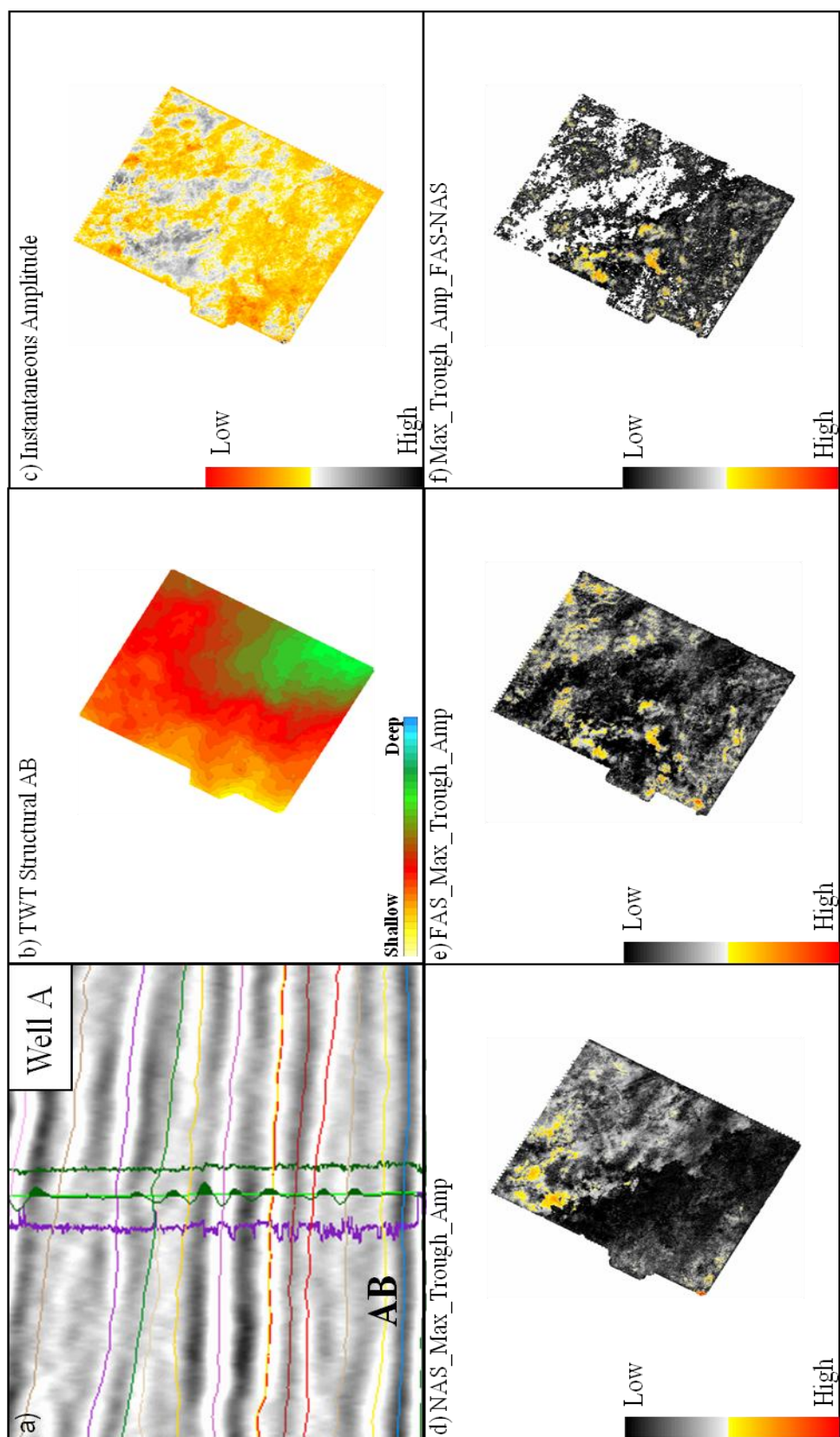


Figure F1. Composite image of marker AB. a) west-to-east seismic section showing the seismic character of marker AB, b) TWT structural map, c) instantaneous amplitude map, d) maximum trough amplitude calculated from the near angle stack, e) maximum trough amplitude calculated from the far angle stack, and f) difference between far and near maximum trough amplitude.

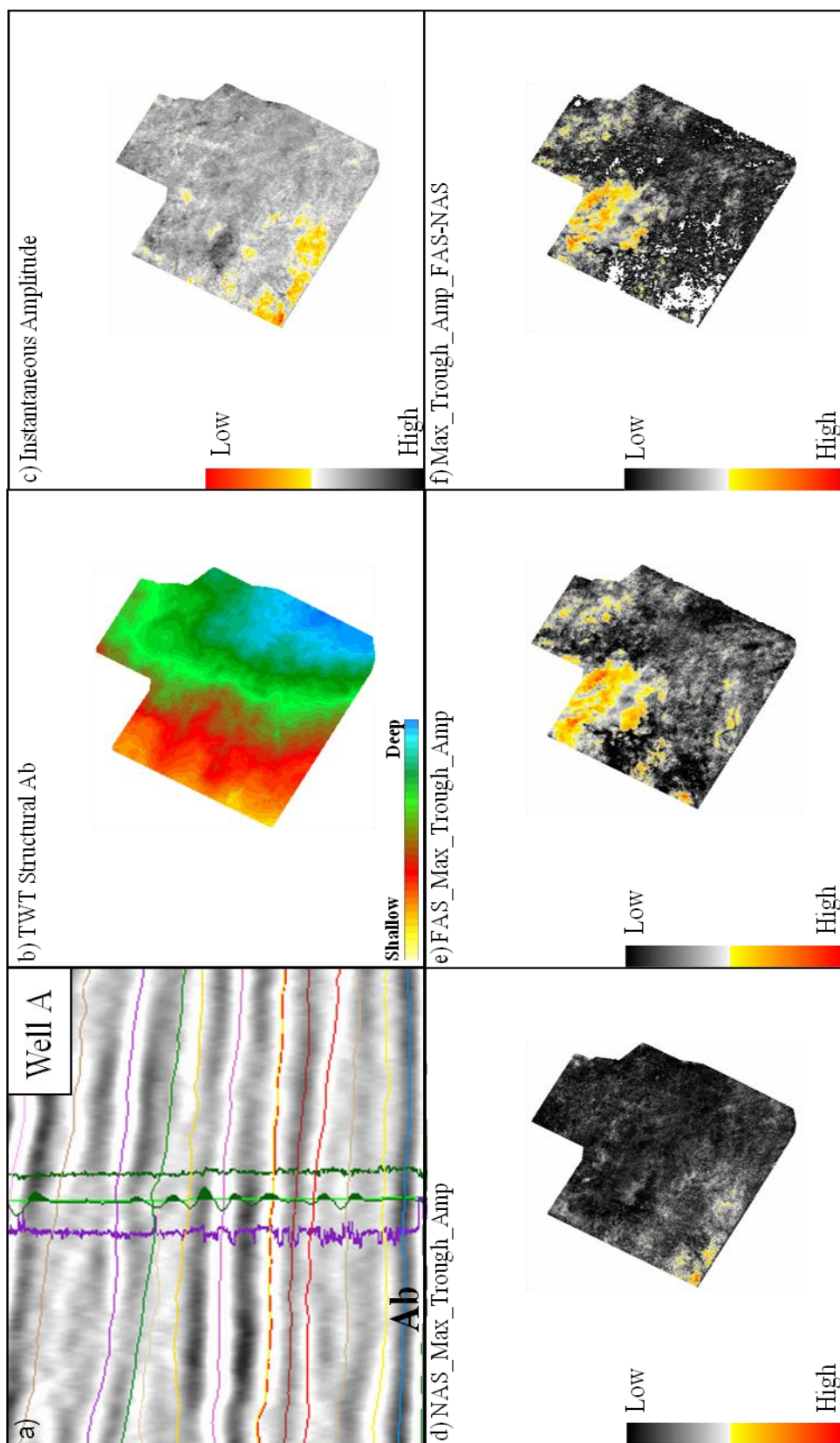


Figure F1. Composite image of marker Ab. a) west-to-east seismic section showing the seismic character of marker Ab, b) TWT structural map, c) instantaneous amplitude map, d) maximum trough amplitude calculated from the near angle stack, e) maximum trough amplitude calculated from the far angle stack, and f) difference between far and near maximum trough amplitude.